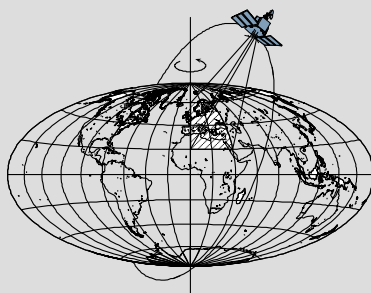# Coseismic Deformation Detection and Quantification for Great Earthquakes Using Spaceborne Gravimetry

by

Lei Wang

Report No. 498

Geodetic Science

The Ohio State University
Columbus, Ohio 43210

March 2012

Preface

This Ohio State University Geodetic Science Report was prepared for, in part, and submitted to the Graduate School of the Ohio State University as a Dissertation in partial fulfillment of the requirements of the Doctor of Philosophy (PhD) degree.

Abstract

Because of Earth's elasticity and its viscoelasticity, earthquakes induce mass redistributions in the crust and upper mantle, and consequently change Earth's external gravitational field. Data from Gravity Recovery And Climate Experiment (GRACE) spaceborne gravimetry mission is able to detect the permanent gravitational and its gradient changes caused by great earthquakes, and provides an independent and thus valuable data type for earthquake studies. This study uses a spatiospectral localization analysis employing the Slepian basis functions and shows that the method is novel and efficient to represent and analyze regional signals, and particularly suitable for extracting coseismic deformation signals from GRACE. For the first time, this study uses the Monte Carlo optimization method (Simulated Annealing) for geophysical inversion to quantify earthquake faulting parameters using GRACE detected gravitational changes. GRACE monthly gravity field solutions have been analyzed for recent great earthquakes. For the 2004 Mw 9.2 Sumatra-Andaman and 2005 Nias earthquakes (Mw 8.6), it is shown for the first time that refined deformation signals are detectable by processing the GRACE data in terms of the full gravitational gradient tensor. The GRACE-inferred gravitational gradients agree well with coseismic model predictions. Due to the characteristics of gradient measurements, which have enhanced high-frequency contents, the GRACE observations provide a more clear delineation of the fault lines, locate significant slips, and better define the extent of the coseismic deformation; For the 2010 Mw 8.8 Maule (Chile) earthquake and the 2011 Mw 9.0 Tohoku-Oki earthquake, by inverting the GRACE detected gravity change signals, it is demonstrated that, complimentary to classic teleseismic records and geodetic measurements, the coseismic gravitational change observed by spaceborne gravimetry can be used to quantify large scale deformations induced by great earthquakes.

Table of Contents

Chapter 1:   Introduction

1.1   Recent Great Earthquakes

Earthquake is one of the most devastating natural hazards facing mankind. The most recent catastrophic events include the 11 March 2011 Mw 9.0 Tohoku-Oki earthquake in Japan, the 27 February 2010 Mw 8.8 Maule earthquake in Chile, the 12 January 2010 Mw 7.0 Léogâne earthquake in Haiti, the 12 May 2008 Mw 8.0 Wenchun earthquake in China, and the 26 December 2004 Mw 9.2 Sumatra-Andaman megathrust earthquake which generated the giant Indian Ocean killer tsunami. The Haitian and the Wenchun earthquakes alone killed 224,000 and 68,000 people, respectively, while the Sumatra-Andaman earthquake and the resulting Indian Ocean tsunami incurred 230,000 casualties in fourteen countries. The most recent Tohoku-Oki earthquake claimed lives of 15,845 people and the tsunami caused a series of nuclear accidents which affected hundreds of thousands of nearby residents. Improved quantification of these earthquake events, including the exact sizes, geometries and orientations of the faults and the associated coseismic deformation is critical towards achieving our ultimate goal to understand the mechanisms of earthquake and volcano activities and potentially lead to an improvement in the prediction of such events.

Parameters quantifying earthquake faulting characteristics, such as the earthquake location, rupture size (length and width), rupture orientation, average displacement etc., have played major roles in the evolution of the theory of plate tectonics and revealing the lithospheric properties, which are meaningful scientific topics dedicated to the understanding of the processes and properties in Earth's crust and upper mantle. For example, the exact knowledge of the spatial distribution of earthquakes can be used to determine the location of plate boundaries, focal mechanisms can be used to infer the directions of relative motion between plates, and the rates and cumulative displacements of earthquake occurrences can be used to infer the relative velocities between plates.

Traditionally, *seismological methods* are used to determine the physical and geometric parameters quantifying the earthquake faulting characteristics. However, some of these parameters cannot be well resolved due to the intrinsic limits in the seismic wave analysis. For instance, although the pattern of seismic wave motions is able to constrain the overall geometry of fault and the sense of slip, the resolution generally is poor for the determination of slip distribution on the fault plane. The body wave data are relatively sensitive to depth of the earthquake focus, but there are trade-offs with many other parameters in the faulting quantification (Lay and Wallace, 1995). The absolute location of the epicenter cannot be well constrained purely by seismic waves, and its estimation highly relies on topographic features and the locations of aftershocks.

1.2 Geodetic Techniques for Earthquake Deformation Study

Alternative to seismic wave records, *geodetic measurements* including GNSS (Global Navigation Satellite System)- derived horizontal and vertical displacements, and InSAR (Interferometric Synthetic Aperture Radar)-derived vertical crustal deformations over land are commonly used to study earthquake mechanisms. Geodetic observations play even more important roles in describing earthquakes which donot rupture the ground surface, or when the teleseismic records cannot definitively determine the rupture geometry.

1.2.1 GPS

The Global Positioning System (GPS), developed by the US Department of Defense for military and civilian navigation and positioning, has revolutionized studies for a wide range of scientific topics, such as plate motions, the deformation around active faults and volcanoes, the glacial isostatic adjustment, global sea level change estimation (when GPS measurement is combined with tide gauge records) and GPS meteorology. GPS is now more generally called GNSS, since other nations are also developing operational navigation satellite systems. Here in this study, we use the term GPS and GNSS interchangeably. GPS provides three-dimensional relative positions with precision of a few millimeters to approximately one centimeter, for baselines of length from hundreds of meters to thousands of kilometers (Segall and Davis, 1997), and therefore is widely used to measure the three-dimensional co- and post-seismic displacements. Both of the horizontal and vertical coseismic displacements on the land are induced by slips on one or several planes of displacement discontinuity (i.e. fault planes) buried in the earth. Thus, the GPS-measured surface coseismic displacements can be inverted for faulting parameters, such as rupture geometry and slip distribution.

Continuous and campaign-type GPS measurements have been used to detect co-seismic displacements and determine finite faulting models for recent great earthquakes such as the 2004 Mw 9.1-9.3 Sumatra-Andaman earthquake (Banerjee *et al.*, 2005; Jade *et al.*, 2005; Vigny *et al.*, 2005; Gahalaut *et al.*, 2006; Subarya *et al.*, 2006), the 2010 Mw 8.8 Maule, Chile earthquake (Delouis *et al.*, 2010; Moreno *et al.,* 2010; Pollitz *et al.,* 2011; Vigny *et al.,* 2011) and the 2011 Mw 9.0 Tohoku-Oki earthquake (Iinuma *et al.,* 2011; Ozawa *et al.,* 2011; Pollitz *et al.,* 2011; Simons *et al.,* 2011). Specifically, for instance, Vigny *et al.* (2006) analyzed GPS data from ~60 stations distributed in a range of 400km~4000km away from the seismic epicenter of the 2004 Sumatra-Andaman earthquake, and detected significant coseismic jumps between 5mm ~ 27cm at all stations for this event. By using GPS detected coseismic displacements, they also showed that the fault plane for this earthquake must be at least 1000km long with non-homogeneous slip distributions on it. Using GPS measured interseismic deformation during the past ten years before the 2010 Maule event, Moreno *et al.* (2010) derived the interseismic locking pattern along a segment of the Andean subduction zone, and found that the patchwork of interseismic locking distribution is spatially correlated with the slip distribution for the 2010 Maule earthquake. For the recent 2011 Tohoku-Oki great earthquake, Ozawa *et al.* (2011) found the maximum horizontal coseismic displacement of 5.3m eastwards, and

maximum subsidence of 1.2m along the coastal line of the Tohoku region, by analyzing data from GPS Earth Observation Network (GEONET) operated by the Geospatial Information Authority of Japan. The inverted slips from these GPS observations indicate the rupture area during the 2011 Tohoku-Oki event extends approximately 400km along the Japan trench, where large strain accumulation rate was observed before the earthquake.

1.2.2 InSAR

InSAR (Interferometric Synthetic Aperture Radar) is a geodetic tool which combines conventional SAR techniques and interferometry techniques. Starting from early 1990s, it became popular to utilize radar interferometry to measure changes on Earth's surface. Two images can be acquired by spaceborne or airborne synthetic aperture radar at two distinct epochs. The change in distance between the ground surface and the on-board radar instrument can be estimated from the interference pattern due to the difference in phase between these two images. The InSAR generated interferogram can have the spatial and temporal resolution of ~100 pixels km^{-2} and 1 pass $month^{-1}$, respectively, and the observation accuracy of about 1 cm (Massonnet and Feigl, 1998).

In order to capture the signature (surface displacement) of an earthquake, two images must be obtained by the satellite or aircraft over the seismic region, one of them before the earthquake and the other one after the earthquake. The coseismic displacements by the earthquake can be estimated from changes in line-of-sight (LOS) range (range between ground point and radar antenna), which is derived by "unwrapping" the interferogram resulting from the two images. InSAR systems have been used extensively in the past two decades for coseismic displacement detections and slip modelings. For the 2010 Mw 8.8 Maule (Chile) earthquake, for example, Delouis *et al.* (2010) jointly inverted for the spatial and temporal distributions of slip during this event by combining the ALOS/PALSAR ScanSAR raw data with GPS and teleseismic broadband data. Tong *et al.* (2010) analyzed ascending and descending ALOS interferograms and found the maximum slip associated with the Maule earthquake was about 17m at a depth of 18km, and the rupture stopped at a depth of 43 ~ 48km. Lorito *et al.* (2010) jointly inverted tsunami and the ALSO observations for both coseismic slip distribution and stress changes resulting from Maule earthquake. Subsequently, they claimed that a zone of high preseismic locking remained unbroken.

Unfortunately, for great undersea earthquakes, GPS and InSAR measurements typically have poor sensitivity to the occurrence of slip far offshore, since they only measure far-field displacement on land, and cannot provide enough constraints for the significant coseismic seafloor deformations near the epicenter. In addition, limited by relatively high expense and logistics, it is not realistic to build up a large number of GPS stations densely covering the whole deformation area to provide strong observation constraints.

1.2.3 Spaceborne Gravimetry

Spaceborne gravimetry geodesy is the science of measuring the Earth's gravity field using space techniques, allows both the static and temporal variable constituents of the Earth's gravity field to be mapped with unprecedented accuracy and spatial resolution, and contributes to a better understanding of Earth system. The Gravity Recovery And Climate Experiment (GRACE) (Tapley *et al.*, 2004), which is a satellite mission jointly launched in 2002 by the National Aeronautics and Space Administration (NASA) and the Deutsche Forschungsanstalt für Luft und Raumfahrt (DLR), is making detailed measurements of Earth's gravity field, as well as its temporally variable component, with spatial resolution of several hundreds kilometers and temporal sampling of about 30 days. The GRACE-estimated Earth gravity fields revolutionized our understandings about the mass redistribution within the Earth system, e.g., terrestrial hydrologic water balance, ocean mass variations, sea-level rise, and ice-sheet and glacier ablations. The Gravity field and steady-state Ocean Circulation Explorer (GOCE), another satellite gravimetry mission launched in March 2009 by the European Space Agency (ESA), is dedicated to measure Earth's static gravity field with unprecedented accuracy and spatial resolution, i.e. with accuracy of 1*mGal* for gravity and 1~2cm for the geoid at a resolution of 100km, corresponding to spherical harmonic degree of 200. The accurate static gravity field model from GOCE is expected to benefit many scientific areas. In geodesy, it helps to build a unified height system. In oceanography, it helps to understand better the dynamic ocean topography, and absolute ocean circulation. In geophysics, since the gravity field reveals density variations in the Earth's interior, it will provide new insights into processes occurring in the lithosphere and upper mantle – down to a depth of about 200km (Drinkwater *et al.,* 2008).

Earthquakes cause mass redistribution in the Earth's crust and upper mantle, and permanently disturb Earth's gravity field in free space, which would be detected by current spaceborne gravimetry missions. GRACE provides uniform coverage over both ocean and land, although its application to earthquake studies is limited by its current relatively coarse spatial resolution. It has been proven by a series of studies that the co/post-seismic gravity signatures can be detected by GRACE for the 2004 Mw Sumatra earthquake (Han *et al,* 2006; Chen *et al.,* 2007; Panet *et al.,* 2007; Han and Simons*,* 2008; de Linage *et al.,* 2009; Simons *et al.,* 2009; Broerse *et al.,* 2011; Wang et al., 2012c), the 2010 Mw 8.8 Maule earthquake (Han *et al.,* 2010; Heki and Matsuo*,* 2010; Wang *et al.,* 2012a); as well as the recent 2011 Mw 9.0 Tohoku-Oki great earthquake (Matsuo and Heki*,* 2011; Wang *et al.,* 2012b). This study not only explores efficient data processing schemes to extract coseismic gravity signals from spaceborne gravimetry observation, but also discusses the feasibility of faulting parameter inversions using the detected signals.

1.3   Research Methodology and Outline

The scientific objective of this study are to explore effective data processing schemes to extract Earth's deformation signals due to large undersea earthquakes from the spaceborne gravimetry data provided by GRACE, and to provide a new type of

observation, i.e., gravity and gravitational gradients, to complimentarily constrain earthquake faulting modeling towards improved understanding of their mechanisms. An innovative spatiospectral localization analysis is applied to GRACE monthly gravitational solutions in order to extract co/post-seismic gravity changes due to great earthquakes. Subsequently, a Monte-Carlo inversion technique based on the simulated annealing algorithm is developed to allow the spaceborne gravity measurements to constrain earthquake faulting parameters. In addition, the calculations of coseismic gravitational changes due to shear and tensile faults in a half-space, both numerically and analytically, have been developed in this study.

The detailed mapping of coseismic gravity changes and estimations of faulting parameters from spaceborne gravimetry are expected to shed new light on the processes exciting earthquake (and volcano) activities, and potentially lead to improvement in the prediction of such events. This study opens up a new field of earthquake studies, namely those purely conducted from space gravity observation, not just seismological or of other geodetic means.

Chapter 2 gives the detailed derivations and numerical examples of coseismic gravitational and gradient changes due to finite fault model in a homogeneous half-space. Chapter 3 introduces the spatiospectral localization analysis for bandlimited signals based on the Slepian basis functions, and its advantages in the coseismic deformation studies. Subsequently, the simulated annealing (SA) algorithm, which is a popular non-linear inversion technique, is developed in Chapter 4 for inverting subsurface anomalies. The theories and methods developed in this study are applied to three recent earthquakes: the 2004 Mw 9.2 Sumatra event, the 2010 Mw 8.8 Maule event, and the 2011 Mw 9.0 Tohoku-Oki event, and the detailed analyses as well as subsequent results are presented in Chapter 5. Chapter 6 concludes the work in this dissertation.

Chapter 2: Gravitation and Gravitational Gradients Changes due to Shear and Tensile Faults in a Half Space

Earthquakes disturb Earth's gravitational potential, and consequently change gravitation and gravitational gradient observables on and above the surface of the Earth. Before discussing the coseismic gravitational changes due to earthquakes, the meanings of two terms, 'displacement' and 'dislocation', should be explicitly explained. 'Displacement' refers to the vector distance of a particle in half-space at time t from its initial position at time t_0, and 'dislocation' is regarded as the discontinuity in displacement or strain across a rupturing fault surface (Aki and Richards, 2002). To describe deformations and associated gravitation changes due to earthquakes, it is a simplified but effective way to model earthquakes as dislocations on a rectangular plane in a homogeneous elastic half-space (Okada, 1985; Okubo, 1991,1992). Dislocation theory adequately explains the coseimic displacement field (Press, 1965; Okada, 1985) and has been widely applied to coseismic deformation analyses.

The gravitational potential changes due to earthquakes are attributable to three factors (Okubo, 1991, 1992):

(1) The density perturbation $-\rho \nabla \cdot \bar{u}$ of the half-space material, where ρ is the original density of the unperturbed half-space, and $\bar{u}$ is the displacement field in the half-space.

(2) The surface mass density change $\rho \Delta h$ owing to the uplift/subsidence Δh of the originally flat half-space surface.

(3) Attraction of mass with density ρ' filling into the cavity created by tensile fracturing. For example, the upwelling magma rises up to fill the gap formed as the tectonic plates gradually moving apart at mid-ocean ridges.

This chapter presents two methods, i.e. an analytical method and a numerical method (Fourier method), to calculate the coseismic gravitation and gravitational gradient changes due to dislocation on a rectangular fault plane with the assumption of a homogeneous elastic half-space.

2.1 Analytical Method

The gravitational potential change caused by a point dislocation source is first discussed. By integrating the Green's function describing the point source effect over the whole rectangular fault plane, the expression of potential change caused by dislocation on a rectangular fault can be derived. Subsequently, the analytical expressions of the gravitation and gravitational gradient changes due to dislocation on a fault can be obtained by taking the first and second derivatives of the potential change.

2.1.1 Displacement Caused by Point Dislocation

Let's first discuss the displacement field $\vec{u}$ caused by a point dislocation buried in a homogeneous, isotropic and perfectly elastic half-space of density ρ. In Figure 2.1, a left-hand Cartesian frame is defined in the way that the x_1ox_2 plane spans the surface of the half-space with x_3-axis pointing perpendicularly downwards. A point dislocation source is buried at $(0,0,\xi_3)$ in the half-space.
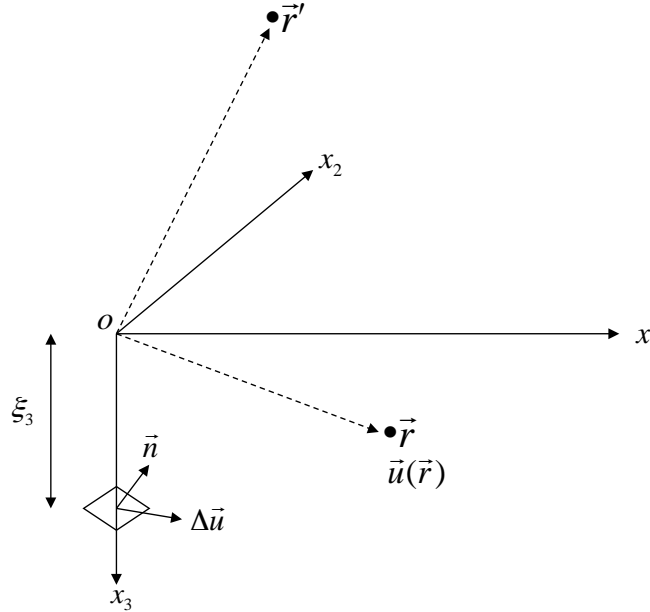
Figure 2.1: Point dislocation source buried in a half-space.

The point source can be considered as an infinitesimal fault of area $d\Sigma$ having the normal direction $\vec{n} = (n_1, n_2, n_3)$. The dislocation on this infinitesimal fault plane is represented by a vector $\Delta\vec{u} = (u_1, u_2, u_3)$. Steketee (1958) shows that the displacement vector at an arbitrary point $\vec{r} = (x_1, x_2, x_3)$ in the half-space can be computed as:

$$\vec{u}(\vec{r}; \xi_3) = \int_{d\Sigma} \frac{1}{8\pi\mu} \vec{\omega}^{(ij)}(\vec{r}; \xi_3) u_i n_j ds = \frac{1}{8\pi\mu} \vec{\omega}^{(ij)}(\vec{r}; \xi_3) u_i n_j d\Sigma \qquad (2.1)$$

where the Einstein's summation convention is applied and μ is the rigidity of the half-space medium. The kernel vector $\vec{\omega}^{(ij)}$ is proportional to the displacement at $\vec{r}$ caused by a dislocation in direction of x_i on the infinitesimal fault plane perpendicular to x_j axis. Based on the work of Mindlin & Cheng (1950) who derived explicit expressions of the displacement and stress fields for half-space nuclei of strain, Press (1965) showed that $\vec{\omega}^{(ij)}$ has the form of:

$$\bar{\omega}_{ij}(\vec{r},\xi_3) = \left\{ \frac{\lambda+\mu}{\lambda+2\mu} \left[\lambda\delta^{ij} \frac{\partial}{\partial\xi_k} + \mu\left(\delta^{ij} \frac{\partial}{\partial\xi_j} + \delta^{jk} \frac{\partial}{\partial\xi_i} \right) \right] \bar{v}^{(k)}(\vec{r},\vec{\xi}) \right\}\Bigg|_{\xi_1=\xi_2=0} \tag{2.2}$$

where λ and μ denote the Lamé constants, and δ^{ij} is Kronecker's delta function. The vector $\bar{v}^{(k)}(\vec{r},\vec{\xi})$ in (2.2) is the displacement at $\vec{r}$ due to a single force at $\vec{\xi}$ in x_k-

direction with magnitude of $\dfrac{8\pi\mu(\lambda+2\mu)A_0}{(\lambda+\mu)}$, and A_0 stands for the unit area (Okubo,

1991). Mindlin & Cheng (1950) gave the form of $\bar{v}^{(k)}(\vec{r},\vec{\xi})$ as:

$$\bar{v}^{(k)}(\vec{r},\vec{\xi}) = 2(1-v)\left[\nabla\left(\nabla\cdot\vec{\Gamma}^{(k)} \right) - \nabla\times\nabla\times\vec{\Gamma}^{(k)} \right] - \nabla\left(\nabla\cdot\vec{\Gamma}^{(k)} \right)$$
$$= 2(1-v)\nabla^2\vec{\Gamma}^{(k)} - \nabla\left(\nabla\cdot\vec{\Gamma}^{(k)} \right) \tag{2.3}$$

where v is Possion's ratio and $\vec{\Gamma}^{(k)}$ denote the Galerkin vector, whose explicit expression is given in Appendix A.

2.1.2 Gravitational Potential Changes Caused by Point Dislocation

Earthquakes induce mass redistribution both in the interior and on the surface of the earth, and thereby perturb Earth's gravitational field. After obtaining the displacement field, which quantitively describes the earthquake-induced mass movement, one can model the associated gravitational potential changes. Okubo (1991) divided the potential change caused by a subsurface point dislocation into two parts:

(1) The gravitational potential change ψ due to internal density disturbance $-\rho\nabla\cdot\vec{u}$ (divergence of the displacement field multiplied by density) to the original homogeneous density ρ;

(2) The gravitational potential change φ due to vertical deformation Δh of the originally flat half-space surface. The surface density change at the surface can be computed as $\rho\Delta h$.

2.1.2.1 Gravitational Potential Change Due to Density Changes

At an observation point $\vec{r}' = (x_1', x_2', x_3')$ outside of the half-space (see Figure 2.1), the gravitational potential change associated with the dilatation field, i.e. expansion/contraction of the half-space medium triggered by a point source buried at $(0,0,\xi_3)$, can be evaluated as:

$$\psi(\vec{r}',\xi_3) = G\rho \int_V \frac{\nabla\cdot\vec{u}}{|\vec{r}-\vec{r}'|} dV(\vec{r})$$

$$= \frac{G\rho}{8\pi\mu} \int_V \left(\frac{\nabla\cdot\bar{\omega}^{(ij)}(\vec{r},\xi_3)}{|\vec{r}-\vec{r}'|} u_i n_j d\Sigma \right) dV(\vec{r})$$

$$= \frac{G\rho}{8\pi\mu}\left(\int_V \frac{\nabla\cdot\vec{\omega}^{(ij)}(\vec{r},\xi_3)}{|\vec{r}-\vec{r}'|}dV(\vec{r})\right)u_i n_j d\Sigma$$

$$= \psi^{(ij)}u_i n_j d\Sigma \tag{2.4}$$

where

$$\psi^{(ij)}\left(\vec{r}',\xi_3\right) \equiv \frac{G\rho}{8\pi\mu}\int_V \frac{\nabla\cdot\vec{\omega}^{(ij)}(\vec{r},\xi_3)}{|\vec{r}-\vec{r}'|}dV(\vec{r}) \quad . \tag{2.5}$$

From equation (2.4), it can be seen that the expression $\psi^{(ij)}\left(\vec{r}',\xi_3\right)$ in equation (2.5) represents the gravitational potential change at $\vec{r}'$ caused by a unit dislocation in direction of x_i on an infinitesimal fault plane located at $\left(0,0,\xi_3\right)$, whose normal direction is parallel to x_j axis. The expression of displacement vector $u(\vec{r})$ in (2.4) is give by equation (2.1).

By using equation (2.2) and (2.3), the term of $\nabla\cdot\vec{\omega}^{(ij)}(\vec{r},\xi_3)$ in the integrand of equation (2.5) can be evaluated as:

$$\nabla\cdot\vec{\omega}^{(ij)}(\vec{r},\xi_3) = \nabla\cdot\left\{\frac{\lambda+\mu}{\lambda+2\mu}\left[\lambda\delta^{ij}\frac{\partial}{\partial\xi_k}+\mu\left(\delta^{ij}\frac{\partial}{\partial\xi_j}+\delta^{jk}\frac{\partial}{\partial\xi_i}\right)\right]\vec{v}^{(k)}\left(\vec{r},\vec{\xi}\right)\right\}\Bigg|_{\xi_1=\xi_2=0}$$

$$= \left\{\frac{\lambda+\mu}{\lambda+2\mu}\left[\lambda\delta^{ij}\frac{\partial}{\partial\xi_k}+\mu\left(\delta^{ij}\frac{\partial}{\partial\xi_j}+\delta^{jk}\frac{\partial}{\partial\xi_i}\right)\right]\nabla\cdot\vec{v}^{(k)}\left(\vec{r},\vec{\xi}\right)\right\}\Bigg|_{\xi_1=\xi_2=0}$$

$$= \left\{\frac{\lambda+\mu}{\lambda+2\mu}\left[\lambda\delta^{ij}\frac{\partial}{\partial\xi_k}+\mu\left(\delta^{ij}\frac{\partial}{\partial\xi_j}+\delta^{jk}\frac{\partial}{\partial\xi_i}\right)\right]\nabla\cdot\left(2(1-v)\nabla^2\vec{\Gamma}^{(k)}-\nabla\left(\nabla\cdot\vec{\Gamma}^{(k)}\right)\right)\right\}\Bigg|_{\xi_1=\xi_2=0}$$

$$= \left\{\left[\lambda\delta^{ij}\frac{\partial}{\partial\xi_k}+\mu\left(\delta^{ij}\frac{\partial}{\partial\xi_j}+\delta^{jk}\frac{\partial}{\partial\xi_i}\right)\right]\left[\nabla\cdot\left(\nabla^2\vec{\Gamma}^{(k)}\right)-\frac{\lambda+\mu}{\lambda+2\mu}\nabla^2\left(\nabla\cdot\vec{\Gamma}^{(k)}\right)\right]\right\}\Bigg|_{\xi_1=\xi_2=0}$$

$$= \left\{\left[\lambda\delta^{ij}\frac{\partial}{\partial\xi_k}+\mu\left(\delta^{ij}\frac{\partial}{\partial\xi_j}+\delta^{jk}\frac{\partial}{\partial\xi_i}\right)\right]\left[\frac{\mu}{\lambda+2\mu}\nabla^2\left(\nabla\cdot\vec{\Gamma}^{(k)}\right)\right]\right\}\Bigg|_{\xi_1=\xi_2=0}$$

$$= \frac{\mu}{\lambda+2\mu}\nabla^2 P^{(ij)}\left(\vec{r},\xi_3\right) \tag{2.6}$$

where

$$P^{(ij)}\left(\vec{r},\xi_3\right) \equiv \left\{\left[\lambda\delta^{ij}\frac{\partial}{\partial\xi_k}+\mu\left(\delta^{ij}\frac{\partial}{\partial\xi_j}+\delta^{jk}\frac{\partial}{\partial\xi_i}\right)\right]\left(\nabla\cdot\vec{\Gamma}^{(k)}\left(\vec{r},\vec{\xi}\right)\right)\right\}\Bigg|_{\xi_1=\xi_2=0} \tag{2.7}$$

Using the new notation $P^{(ij)}(\vec{r}, \xi_3)$ defined in equation (2.7), equation (2.5) can be rewritten as:

$$\psi^{(ij)}(\vec{r}', \xi_3) = \frac{G\rho}{8\pi(\lambda + 2\mu)} \int_V \frac{\nabla^2 P^{(ij)}(\vec{r}, \xi_3)}{|\vec{r} - \vec{r}'|} dV(\vec{r}) \qquad (2.8)$$

As pointed out by Okubo (1991), singularities at the dislocation source exist if the potential change of $\psi^{(ij)}(\vec{r}', \xi_3)$ is evaluated using equation (2.8) directly, since the factor $\frac{1}{|\vec{r} - \vec{\xi}|}$ shows up in the term of $\nabla^2 P^{(ij)}(\vec{r}, \xi_3)$ after substituting the expressions of Galerkin vector given by equation A.1~A.3 into equation (2.7). To avoid the singularity, equation (2.8) can be rewritten using Green's theorem as:

$$\psi^{(ij)}(\vec{r}', \xi_3) = \frac{G\rho}{8\pi(\lambda + 2\mu)} \left\{ \int_{S_0} \left[-P^{(ij)}(\vec{r}', \xi_3) \nabla \left(\frac{1}{|\vec{r} - \vec{r}'|} \right) + \frac{\nabla P^{(ij)}(\vec{r}, \xi_3)}{|\vec{r} - \vec{r}'|} \right] (-\vec{e}_3) ds \right.$$

$$\left. + \int_V P^{(ij)}(\vec{r}, \xi_3) \nabla^2 \left(\frac{1}{|\vec{r} - \vec{r}'|} \right) dV(\vec{r}) \right\}$$

$$= \frac{G\rho}{8\pi(\lambda + 2\mu)} \left\{ \int_{S_0} \left[P^{(ij)}(\vec{r}', \xi_3) \frac{\partial}{\partial x_3} \left(\frac{1}{|\vec{r} - \vec{r}'|} \right) - \frac{\partial P^{(ij)}(\vec{r}, \xi_3)}{\partial x_3} \frac{1}{|\vec{r} - \vec{r}'|} \right] ds \right.$$

$$\left. + \int_V P^{(ij)}(\vec{r}, \xi_3) \nabla^2 \left(\frac{1}{|\vec{r} - \vec{r}'|} \right) dV(\vec{r}) \right\} \qquad (2.9)$$

where S_0 denotes surface of the half-space at $x_3 = 0$, and $\vec{e}_3$ the unit vector of x_3 direction. By evaluating the surface and volume integral in equation (2.9) respectively, the explicit expressions of $\psi^{(ij)}(\vec{r}', \xi_3)$ are given in Appendix B (*Okubo*, 1991). Unlike above derivations where the notation of $\vec{r}$ was used for the integral variable in half-space, equations (B.1)~(B.4) use $\vec{r}$ to denote the location of the observation outside the half-space $(x_3 < 0)$.

2.1.2.2 Potential Change Due to Surface Vertical Deformation

Based on equation (2.1), the uplift/subsidence of the surface of half-space is obtained as:

$$\Delta h(x_1, x_2; \xi_3) = -\frac{1}{8\pi\mu} \omega_3^{(ij)}(\vec{r}; \xi_3) \Big|_{x_3=0} u_i n_j d\Sigma = \Delta h^{(ij)}(x_1, x_2; \xi_3) u_i n_j d\Sigma \qquad (2.10)$$

where

$$\Delta h^{(ij)}(x_1, x_2; \xi_3) \equiv -\frac{1}{8\pi\mu} \omega_3^{(ij)}(\vec{r}; \xi_3) \Big|_{x_3=0} \qquad (2.11)$$

10

The gravitational potential change due to surface elevation change is approximated by using a thin layer with surface density of $\rho\Delta h$, and can be written as:

$$\phi(\vec{r},\xi_3) = -\int_{-\infty}^{\infty}\int_{-\infty}^{\infty} \frac{G\rho\Delta h(x_1',x_2';\xi_3)}{\sqrt{(x_1-x_1')^2+(x_2-x_2')+x_3^2}}dx_1'dx_2'$$

$$= -\int_{-\infty}^{\infty}\int_{-\infty}^{\infty} G\rho \frac{\Delta h^{(ij)}(x_1',x_2';\xi_3)u_in_jd\Sigma}{\sqrt{(x_1-x_1')^2+(x_2-x_2')+x_3^2}}dx_1'dx_2'$$

$$= \left(-\int_{-\infty}^{\infty}\int_{-\infty}^{\infty} G\rho \frac{\Delta h^{(ij)}(x_1',x_2';\xi_3)}{\sqrt{(x_1-x_1')^2+(x_2-x_2')+x_3^2}}dx_1'dx_2'\right)u_in_jd\Sigma$$

$$= \phi^{(ij)}(\vec{r};\xi_3)u_in_jd\Sigma \tag{2.12}$$

where

$$\phi^{(ij)}(\vec{r};\xi_3) = -\int_{-\infty}^{\infty}\int_{-\infty}^{\infty} G\rho \frac{\Delta h^{(ij)}(x_1',x_2';\xi_3)}{\sqrt{(x_1-x_1')^2+(x_2-x_2')+x_3^2}}dx_1'dx_2' \tag{2.13}$$

Using the expressions for $\Delta h^{(ij)}$ given by Press (1965) and Okada (1985), $\phi^{(ij)}(\vec{r};\xi_3)$ in equation (2.13) can be evaluated using Fourier transforms, since it has the form of convolution integral. Equations (B.5~B.8) list the final evaluations given by Okubo (1991).

2.1.2.3 Total Potential Change

By simply summing together the potential change due to expansion/contraction $\psi^{(ij)}(\vec{r},\xi_3)$ in (2.9) and potential change due to surface uplift/subsidence $\phi^{(ij)}(\vec{r},\xi_3)$ in (2.13), the total gravitational potential change at a point $\vec{r}$ outside the half-space due to a point dislocation buried at $(0,0,\xi_3)$ is obtained as:

$$\Psi^{(ij)}(\vec{r},\xi_3) = \psi^{(ij)}(\vec{r},\xi_3) + \varphi^{(ij)}(\vec{r},\xi_3) \tag{2.14}$$

If some materials of density ρ_0 fill into the cavity generated by tensile opening, a factor

of $-\dfrac{G\rho_0}{R}$ should be added to the diagonal components of $\Psi^{(ij)}(\vec{r};\xi_3)$.

2.1.3   Potential Change Caused by Fault in Half-space

Usually, it is not enough to just use an infinitesimal point dislocation to approximate the effect by a fault plane of finite size. How well the gravitation change due to a finite fault can be approximated by using a point dislocation depends on the distance between observation point and the dislocation source, as well as the size of the actual fault. Thus, it is necessary to consider the gravitational potential change due to uniform dislocation on a rectangular fault, which is a more realistic although simplified geometric

model for earthquakes. Figure 2.2 shows a finite rectangular fault plane with its length, width, depth and dip angle of L, W, d and δ, respectively. As indicated by the red arrows in Figure 2.2, the dislocation on this fault plane has the along-strike, down-dip and tensile components of U_1, U_2 and U_3, respectively. Under the Cartesian frame $ox_1x_2x_3$, the dislocation can be represented by a vector $\vec{U}$:

$$\vec{U} = \begin{pmatrix} U_1 \\ U_2\cos\delta - U_3\sin\delta \\ -U_2\sin\delta - U_3\cos\delta \end{pmatrix} \tag{2.15}$$

and the normal vector of the fault plane is:

$$\vec{n} = \begin{pmatrix} 0 \\ -\sin\delta \\ -\cos\delta \end{pmatrix} \tag{2.16}$$
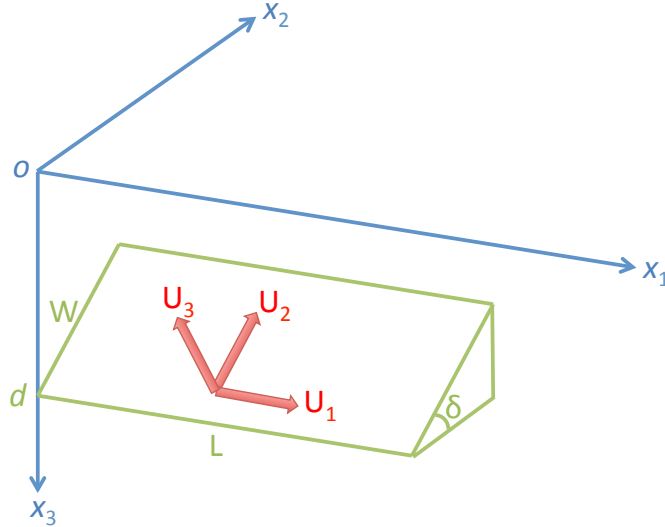
Figure 2.2: Geometry of a fault model. Positive U_1, U_2 and U_3 with $0 < \delta < 90^o$ mean left-lateral strike slip, thrusting slip and tensile opening, respectively.

In order to derive the gravitational potential changes caused by the faulting model in Figure 2.2, the Green's functions $\Psi^{(ij)}$ in (2.14), which describe potential changes excited by point dislocation, are integrated over the rectangular fault plane. To be specific, the total potential change $\Delta\Psi$ at a location $\vec{r} = (x_1, x_2, x_3)$ outside the half-space can be modeled by:

$$\Delta\Psi(x_1, x_2, x_3) = \int_0^L d\xi' \int_0^W d\eta' \Psi^{(ij)}(x_1 - \xi', x_2 - \eta'\cos\delta, x_3; d - \eta'\sin\delta)u_i n_j. \tag{2.17}$$

By applying the variable substitutions of $\xi = x_1 - \xi'$ and $\eta = p - \eta'$, where $p \equiv x_2 \cos\delta + (d - x_3)\sin\delta$, the integral in equation (2.17) turns out to be:

$$\Delta\Psi(x_1, x_2 x_3) = \int_{x_1}^{x_1 - L} d\xi \int_p^{p-W} d\eta \Psi^{(ij)}(\xi, \eta\cos\delta + q\sin\delta, x_3; \eta\sin\delta + d - p\sin\delta) u_i n_j \quad (2.18)$$

Similarly, the gravitational potential change cause by density change is:

$$\Delta\psi(x_1, x_2 x_3) = \int_{x_1}^{x_1 - L} d\xi \int_p^{p-W} d\eta \psi^{(ij)}(\xi, \eta\cos\delta + q\sin\delta, x_3; \eta\sin\delta + d - p\sin\delta) u_i n_j \quad (2.19)$$

In following text, the double-verticals notation is used to represent the form of:

$$f(\xi, \eta)\| \equiv f(x_1, p) - f(x_1, p - W) - f(x_1 - L, p) + f(x_1 - L, p - W) \quad (2.20)$$

Appendix C provides the explicit forms of potential changes after integration (*Okubo*, 1992).

2.1.4   Gravitation Changes Caused by Faults in Half-space

Gravitation is the first derivative of gravitational potential. Therefore, the gravitation change due to faulting in half-space can be derived by taking the derivative of potential change $\Delta\Psi$ in equation (2.17) with respect to x_3. For an observation point attached to the free surface of the half-space, the expression for gravitation change can be written as following form:

$$\Delta g(x_1, x_2, 0) = \left\{ G\rho \left[U_1 S_g(\xi, \eta) + U_2 D_g(\xi, \eta) + U_3 T_g(\xi, \eta) \right] + G\Delta\rho U_3 C_g(\xi, \eta) \right\} \Big\| - \beta\Delta h(x_1, x_2)$$

$$(2.21)$$

where $\beta = 0.3086 \times 10^{-5} / s^2$ takes into account the free-air effect due to the surface vertical motion of Δh. To assume a density of $2.67 kg/m^3$ and vertical uplift of 1 m of the half-space surface, the gravitation change due to the direct attraction of deformed surface is approximately 0.1119 *mGal*, while the free-air effect is 0.3086 *mGal*. Thus, the free-air effect is non-negligible when the observation point is on the free surface of the half-space. S_g, D_g, T_g and C_g are the derivatives of *S, D, T,* and *C* with respect to x_3, respectively, i.e.,

$$(S_g, D_g, T_g, C_g) = \Gamma(S, D, T, C) \quad (2.22)$$

where Γ is an operator defined as:

$$\Gamma \equiv \left(-\frac{\partial}{\partial x_3} - \frac{\partial q}{\partial x_3}\frac{\partial}{\partial q} - \frac{\partial p}{\partial x_3}\frac{\partial}{\partial \eta} \right)\Bigg|_{x_3=0} \quad (2.23)$$

S, D and *T* are terms related to the potential changes caused by U_1, U_2 and U_3 dislocation components respectively, and *C* takes into account the attraction of the mass intruding into the cavity formed by tensile opening. Their explicit expressions are given by (C.3)~(C.6) or (C.14)~(C.16).

Similarly, by taking the derivative of $\Delta\psi$ in equation (2.19) with respect to x_3, gravity change free from the effect of uplift/subsidence of the half-space surface is calculated by:

$$\Delta g^*\left(x_1, x_2, 0\right) = \left\{G\rho\left[U_1 S_g^*\left(\xi, \eta\right) + U_2 D_g^*\left(\xi, \eta\right) + U_3 T_g^*\left(\xi, \eta\right)\right] + G\Delta\rho U_3 C_g^*\left(\xi, \eta\right)\right\}\Big\| \qquad (2.24)$$

Furthermore, the surface vertical deformation Δh caused by dislocation on fault can be obtained by the same integration procedure as in equation (2.17), but using the Green's function of $\Delta h^{(ij)}$ given in equation (2.11), which describes surface vertical deformation caused by point dislocation source. After evaluation of the integral, the surface deformation due to a rectangular fault has the form of (*Okada* 1985, *Okubo* 1992):

$$\Delta h\left(x_1, x_2, 0\right) = \frac{1}{2\pi}\left[U_1 S_h\left(\xi, \eta\right) + U_2 D_h\left(\xi, \eta\right) + U_3 T_h\left(\xi, \eta\right)\right]\Big\|_{.} \qquad (2.25)$$

See Appendix D for explicit forms for (2.21), (2.24) and (2.25).

2.1.5 Gravitational Gradients Changes Caused by Faults in Half-space

The gravitational gradients are the 2nd derivatives of the gravitational potential. Thus, gravitational gradient changes at a fixed point outside the half-space ($x \leq 0$) can be calculated by applying various second order differential operators to the gravitational potential change given by equation (2.18) or (C.1), i.e.,

$$\Delta T_{ij}\left(x_1, x_2, 0\right) = -\frac{\partial^2}{\partial x_i \partial x_j}\Delta\Psi\left(x_1, x_2, 0\right)$$

$$= -\left\{G\rho\left[U_1 S_{ij}\left(\xi, \eta\right) + U_2 D_{ij}\left(\xi, \eta\right) + U_3 T_{ij}\left(\xi, \eta\right)\right] + G\Delta\rho U_3 C_{ij}\left(\xi, \eta\right)\right\}$$

$$\left(i, j = 1, 2, 3\right) \qquad (2.26)$$

where

$$\left(S_{ij}, D_{ij}, T_{ij}, C_{ij}\right) = \frac{\partial^2}{\partial x_i \partial x_j}\left(S, D, T, C\right) \qquad (2.27)$$

Here, the expressions of S, D, T and C are given by equations (C.3)~(C.6) for $\cos\delta \neq 0$ and equations (C.14)~(C.16) for $\cos\delta = 0$. Based on aforementioned results mostly by Okubo (1991,1992), this study for the first time derived the analytical expressions of gradient changes for all five independent tensor components, both total changes and partial changes purely due to internal density perturbation. These analytical expressions are listed in Appendix E.

2.2 Numerical Methods

After dividing the half-space into finite regular grids, the dislocation-induced displacement and dilatation are computed at the center of each small cube. Then, the gravitational potential change, as well as its derivatives, can be numerically evaluated via Fourier transformations of the calculated displacements and dilatations on the regular grids.

2.2.1 Potential/Gravitation/Gravitational Gradients of Infinitesimally thin Mass Sheet

Here, a right-hand Cartesian frame is defined for the homogeneous elastic half-space. The plane spanned by x_1 and x_2 axes is parallel to the surface of half-space, x_1 and x_2 axes point to the east and north, respectively, and x_3 axis points upwards. Let us first consider the gravitational potential generated by an infinitesimally thin mass sheet with surface density of $\sigma(x_1, x_2)$ at depth of $x_3^{(0)}$ (see Figure 2.3).
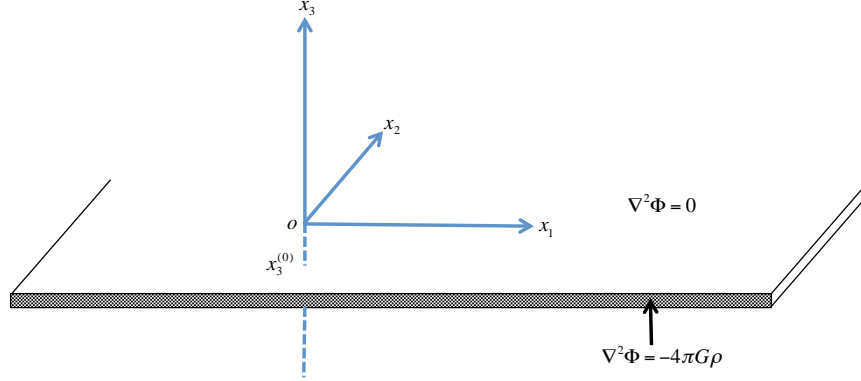
Figure 2.3: An infinitesimally thin mass sheet. Φ is the gravitational potential generated by this thin layer, G is the gravitational constant and ρ is the mass density.

The gravitational potential Φ generated by the mass sheet satisfies Poisson's equation:

$$\frac{\partial^2 \Phi}{\partial x_1^2} + \frac{\partial^2 \Phi}{\partial x_2^2} + \frac{\partial^2 \Phi}{\partial x_3^2} = -4\pi G \sigma(x_1, x_2) \delta(x_3 - x_3^{(0)}) \tag{2.28}$$

with the boundary conditions of:

$$\lim_{|x_1| \to \infty} \Phi = 0 \tag{2.29}$$

$$\lim_{|x_2| \to \infty} \Phi = 0 \tag{2.30}$$

$$\lim_{x_3 \to \infty} \Phi = 0 \tag{2.31}$$

Here, G and ρ are the gravitational constant and mass density, respectively.

The differential equation (2.28) can be solved using 2D Fourier transforms, whose forward and inverse transforms are defined as:

$$F(k_1, k_2) = \int_{-\infty}^{\infty} \int_{-\infty}^{\infty} f(x_1, x_2) e^{-i2\pi(k_1 x_1 + k_2 x_2)} \, dx_1 \, dx_2 \tag{2.32}$$

$$f(x_1, x_2) = \int_{-\infty}^{\infty} \int_{-\infty}^{\infty} F(k_1, k_2) e^{i2\pi(k_1 x_1 + k_2 x_2)} \, dk_1 \, dk_2 \tag{2.33}$$

Applying the forward 2D Fourier transform to variables x_1 and x_2 in equation (2.28) leads to:

$$-4\pi^2\left(k_1^2+k_2^2\right)\Phi\left(k_1,k_2,x_3\right)+\frac{\partial^2\Phi}{\partial x_3^2}=-4\pi G\sigma\left(k_1,k_2\right)\delta\left(x_3-x_3^{(0)}\right) \tag{2.34}$$

Then, forward 1D Fourier transform is applied for variable x_3 in (2.34). Given the fact that:

$$\int_{-\infty}^{\infty}\delta\left(x_3-x_3^{(0)}\right)e^{-i2\pi kx_3}\,dz=e^{-i2\pi kx_3^{(0)}}, \tag{2.35}$$

it gives:

$$\pi\left(k_1^2+k_2^2+k_3^2\right)\Phi\left(k_1,k_2,k_3\right)=G\sigma\left(k_1,k_2,k_3\right)e^{-i2\pi k_3 x_3^{(0)}} \tag{2.36}$$

Therefore, the 2D spectrum of potential at height level of x_3 is solved as:

$$\Phi\left(k_1,k_2,x_3\right)=\frac{G\sigma\left(k_1,k_2\right)}{\pi}\int_{-\infty}^{\infty}\frac{e^{i2\pi k_3\left(x_3-x_3^{(0)}\right)}}{k_3^2+\left(k_1^2+k_2^2\right)}dk_3$$

$$=G\sigma\left(k_1,k_2\right)\frac{e^{-2\pi|\mathbf{k}|\left(x_3-x_3^{(0)}\right)}}{|\mathbf{k}|} \tag{2.37}$$

where $|\mathbf{k}|=\sqrt{k_1^2+k_2^2}$. The expression of potential in space domain can be obtained by applying the inverse 2D Fourier transform to equation (2.37) for variables k_1 and k_2:

$$\Phi\left(x_1,x_2,x_3\right)=G\int_{-\infty}^{\infty}\int_{-\infty}^{\infty}\sigma\left(k_1,k_2\right)\frac{e^{-2\pi|\mathbf{k}|\left(x_3-x_3^{(0)}\right)}}{|\mathbf{k}|}e^{i2\pi\left(k_1x_1+k_2x_2\right)}\,dk_1\,dk_2. \tag{2.38}$$

Equation (2.38) is the expression of the gravitational potential generated by an infinitesimally thin mass sheet with surface density $\sigma\left(x_1,x_2\right)$. By introducing two abstract operators $\Im$ and $\Im^{-1}$ to denote forward and inverse 2D Fourier transforms respectively, equation (2.38) can be concisely rewritten as:

$$\Phi\left(x_1,x_2,x_3;x_3^{(0)}\right)=G\Im^{-1}\left\{\Im\left\{\sigma\left(x_1,x_2\right)\right\}\frac{e^{-2\pi|\mathbf{k}|\left(x_3-x_3^{(0)}\right)}}{|\mathbf{k}|}\right\} \tag{2.39}$$

The gravitation generated by the mass sheet can subsequently be computed by taking the derivative of $\Phi\left(x_1,x_2,x_3\right)$ with respect to x_3:

$$g=-\frac{\partial\Phi}{\partial x_3}=2\pi G\Im^{-1}\left\{\Im\left\{\sigma\left(x_1,x_2\right)\right\}e^{-2\pi|\mathbf{k}|\left(x_3-x_3^{(0)}\right)}\right\} \tag{2.40}$$

Similarly, the gravitational gradient components can be obtained by taking the 2nd derivatives:

$$T_{11} = \frac{\partial^2 \Phi}{\partial x_1^2} = -4\pi^2 G \Im^{-1} \left\{ \Im\{\sigma(x_1, x_2)\} k_1^2 \frac{e^{-2\pi|\mathbf{k}|\left(x_3 - x_3^{(0)}\right)}}{|\mathbf{k}|} \right\} \tag{2.41}$$

$$T_{12} = \frac{\partial^2 \Phi}{\partial x_1 \partial x_2} = -4\pi^2 G \Im^{-1} \left\{ \Im\{\sigma(x_1, x_2)\} k_1 k_2 \frac{e^{-2\pi|\mathbf{k}|\left(x_3 - x_3^{(0)}\right)}}{|\mathbf{k}|} \right\} \tag{2.42}$$

$$T_{13} = -\frac{\partial^2 \Phi}{\partial x_1 \partial x_3} = 4\pi^2 G \Im^{-1} \left\{ \Im\{\sigma(x_1, x_2)\} i k_1 e^{-2\pi|\mathbf{k}|\left(x_3 - x_3^{(0)}\right)} \right\} \tag{2.43}$$

$$T_{22} = \frac{\partial^2 \Phi}{\partial x_2^2} = -4\pi^2 G \Im^{-1} \left\{ \Im\{\sigma(x_1, x_2)\} k_2^2 \frac{e^{-2\pi|\mathbf{k}|\left(x_3 - x_3^{(0)}\right)}}{|\mathbf{k}|} \right\} \tag{2.44}$$

$$T_{23} = -\frac{\partial^2 \Phi}{\partial x_2 \partial x_3} = 4\pi^2 G \Im^{-1} \left\{ \Im\{\sigma(x_1, x_2)\} i k_2 e^{-2\pi|\mathbf{k}|\left(x_3 - x_3^{(0)}\right)} \right\} \tag{2.45}$$

$$T_{33} = \frac{\partial^2 \Phi}{\partial x_3^2} = 4\pi^2 G \Im^{-1} \left\{ \Im\{\sigma(x_1, x_2)\} |\mathbf{k}| e^{-2\pi|\mathbf{k}|\left(x_3 - x_3^{(0)}\right)} \right\} \tag{2.46}$$

2.2.2   Potential/Gravitation/Gravitational Gradient Changes Due to Internal Density Changes

If the dilatation field $\nabla \cdot \vec{u}$ can be calculated, the internal density changes can thereby be evaluated everywhere in the half-space as:

$$\Delta\rho = -\rho \nabla \cdot \vec{u} \tag{2.47}$$

As shown in Figure 2.4, the half-space can be equally divided into a stack of thin layers with constant thickness of Δx_3. When the thickness Δx_3 of each layer is small enough, the dislocation induced volumetric density change within each layer can be approximated by surface density change:

$$\Delta\sigma = \Delta\rho \cdot \Delta x_3 \tag{2.48}$$

17
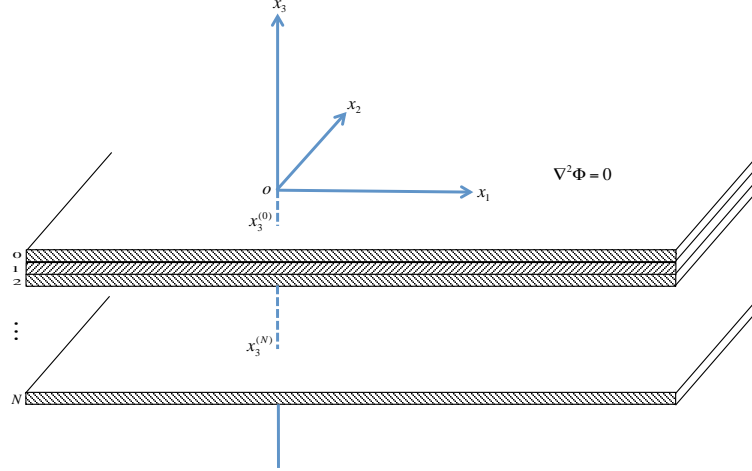
Figure 2.4: Stacking of $N+1$ infinitesimally thin mass layers.

In this way, the potential changes due to the expansion/contraction in each layer can be computed using equation (2.39). The potential change due to density changes in the whole half-space can then be numerically estimated by summing the contributions of all layers:

$$\Phi\left(x_1, x_2, x_3\right) = \int_{-\infty}^{0} \Phi\left(x_1, x_2, x_3; x_3'\right) dx_3'$$

$$\approx \sum_{i=N}^{0} \Phi(x_1, x_2, x_3; x_3^{(i)}) \Delta x_3$$

(2.49)

where $x_3^{(i)}$ denotes the depth of ith layer, and Δx_3 is the thickness of the layers. Similarly, gravitation and gravitational gradients changes can be computed by summing each layer's effects given by equations (2.40)~(2.46).

2.2.3 Potential/Gravitation/Gravitational Gradient Changes Due to Surface Vertical Deformation

Same as the analytical method, gravitation change owing to vertical deformation of the half-space surface is approximated by using a thin layer with surface density $\sigma\left(x_1, x_2\right)$, which is equal to the volumetric density ρ multiplied by the amount of vertical deformation $\Delta h\left(x_1, x_2\right)$:

$$\sigma\left(x_1, x_2\right) = \rho \Delta h\left(x_1, x_2\right).$$

(2.50)

By introducing this thin layer, the potential, gravitation and gravitational gradient changes due to surface vertical deformation are ready to be evaluated using the same approaches discussed in section 2.2.1.

2.3   Numerical Results

In this section, the gravitation and gravitational gradient changes due to different faulting scenarios are modeled using both analytical and numerical methods, and the computation results from these two approaches are compared with each other. This is a way to validate the Fourier approach since the evaluations using analytical formulas can be considered as truths.

A rectangular fault plane with length L=10 km and width W=10 km is used in all numerical examples. The top edge of the fault plane is fixed at depth of 1 km. Poisson's ratio is assumed to be 0.25, and density of the medium is assumed to be $2.67\text{x}10^3$ kg/m^3, consistent with the average density of Earth's crust.

For the first case, dip angle of the fault plane is set to be 30°. The gravitation and gravitational gradient changes triggered by a strike-slip faulting ($U_1 = 5m; U_2 = U_3 = 0$) (see Figure 2.2) on this fault plane are computed over a 50 km×50 km domain on the surface of the half-space, with spatial samplings of 100 m. It can be seen from Figure 2.5 that the gravity changes computed using analytical formula (Figure 2.5a) and using Fourier approach (Figure 2.5b) are very similar. They both reveal characteristic patterns similar to those of elevation changes. The differences between these two results (Figure 2.5c) are about several μGal. Figure 2.6 shows the computed gravitational gradient changes for the same strike-slip faulting. The numerically computed gradient changes approximate the results from analytical formula fairly well for all tensor components. Large differences only show up along edges of the fault plane, particularly at upper corners of the rectangular fault.

Figure 2.5: Gravitation changes in unit of μGal caused by left-lateral faulting: fault length, width and dip are 10km, 10km, and 30°, respectively. Depth to the top edge of the fault is 1km. White rectangular shows the edges of the fault plane. Dislocation $U_1 = 5m$. (a) Gravitation changes calculated using analytical formula; (b) Gravitation changes calculated using Fourier approach; (c) The differences between (a) and (b) shown in a different color scale.

Figure 2.6: Gravitational gradient changes in unit of *mE* caused by left-lateral faulting: fault length, width and dip are 10km, 10km, and 30°, respectively. Depth to the top edge of the fault is 1km. White rectangular shows the edges of the fault plane. Dislocation U_1 = *5m*. (a)~(f) Gravitational gradient changes calculated using analytical formula; (g)~(l) Gravitational gradient changes calculated using Fourier approach; (m)~(r) The differences between the results using two methods shown in a different color scale.

In the 2nd case, the gravitation and gravitational gradient changes are calculated for thrust faulting ($U_2 = 5m; U_1 = U_3 = 0$) (see Figure 2.2) on the same fault plane as the one used in the previous case. The computed gravitation change (Figure 2.7) has larger amplitude than in the strike-slip case (Figure 2.5) although the dislocation magnitudes keep the same. Compared with the gravity change in Figure 2.7, the T_{22}, T_{33} and T_{23} components of the gravitational gradient changes (Figure 2.8), computed both analytically and numerically, more clearly delineate the edge of the fault.

20

Figure 2.7: Gravitation changes in unit of *μGal* caused by thrust faulting: fault length, width and dip are 10km, 10km, and 30°, respectively. Depth to the top edge of the fault is 1km. White rectangular shows the edges of the fault plane. Dislocation $U_2 = 5m$. (a) Gravitation changes calculated using analytical formula; (b) Gravitation changes calculated using Fourier approach; (c) The differences between (a) and (b) shown in a different color scale.

Figure 2.8: Gravitational gradient changes in unit of *mE* caused by thrust faulting: fault length, width and dip are 10km, 10km, and 30°, respectively. Depth to the top edge of the fault is 1km. White rectangular shows the edges of the fault plane. Dislocation $U_2 = 5m$. (a)~(f) Gravitational gradient changes calculated using analytical formula; (g)~(l) Gravitational gradient changes calculated using Fourier approach; (m)~(r) The differences between the results using two methods shown in a different color scale.

In case III, dip angle of the fault plane is increased to 60°, different from the value of 30° used in previous two examples. The computed gravitation and gravitational gradient changes due to left-lateral faulting ($U_1 = 5m; U_2 = U_3 = 0$) are shown in Figure 2.9 and Figure 2.10, respectively. When compared with case I which has the same strike-slip vector but shallower dip angle, it is found that the amplitudes of the gravitation and gravitational gradient changes get smaller as the dip angle increases from 30° in case I to 60° in this case. Good consistencies still exist between the results calculated from analytical formula and from numerical method.
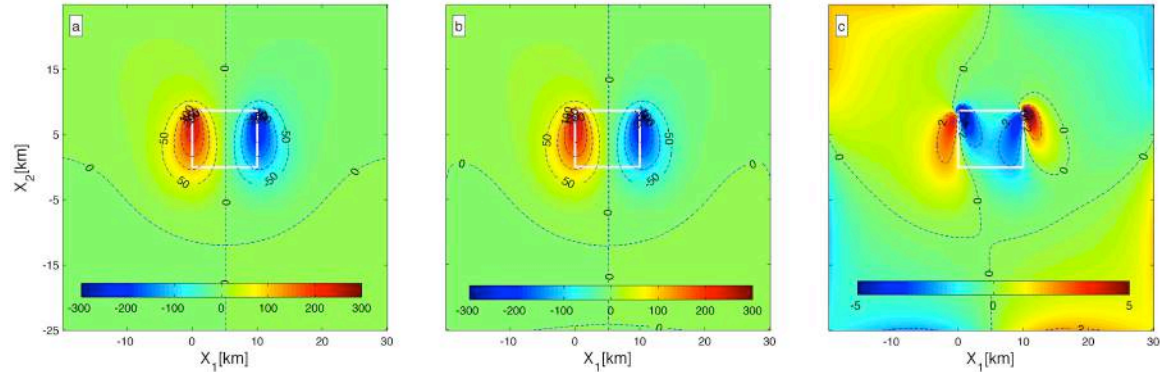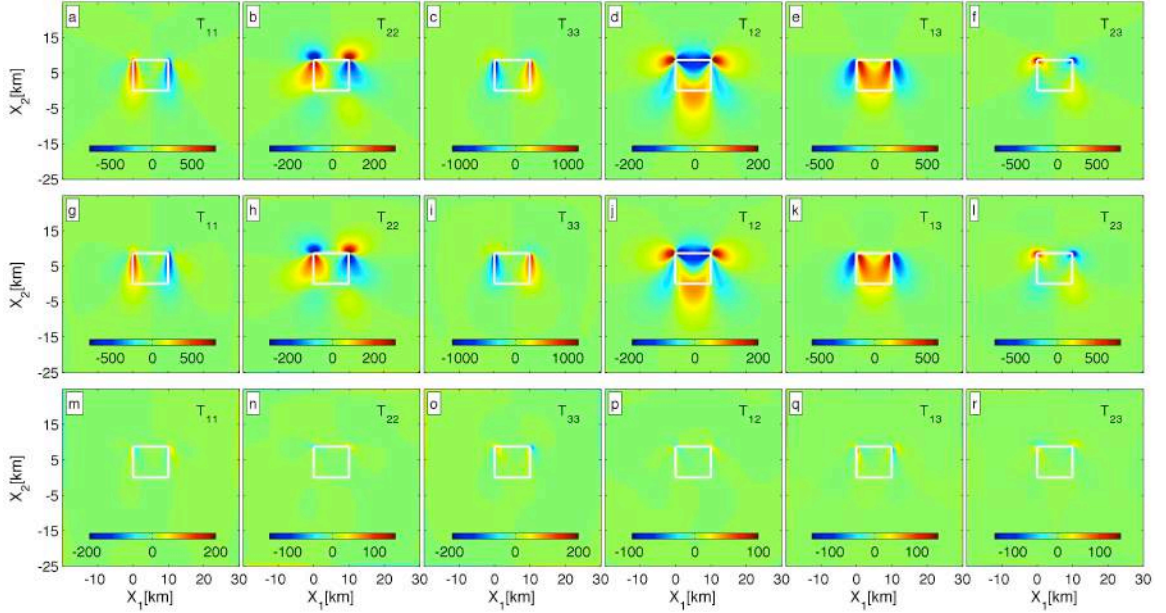
Figure 2.9: Gravitation changes in unit of *μGal* caused by left-lateral faulting: fault length, width and dip are 10km, 10km, and 60°, respectively. Depth to the top edge of the fault is 1km. White rectangular shows the edges of the fault plane. Dislocation $U_1 = 5m$. (a) Gravitation changes calculated using analytical formula; (b) Gravitation changes calculated using Fourier approach; (c) The differences between (a) and (b) shown in a different color scale.

Figure 2.10: Gravitational gradient changes in unit of *mE* caused by left-lateral faulting: fault length, width and dip are 10km, 10km, and 60°, respectively. Depth to the top edge of the fault is 1km. White rectangular shows the edges of the fault plane. Dislocation U_1 = 5m. (a)~(f) Gravitational gradient changes calculated using analytical formula; (g)~(l) Gravitational gradient changes calculated using Fourier approach; (m)~(r) The differences between the results using two methods.

In case IV, The geometry of the fault remains the same as the one in case III, but a thrust faulting is considered ($U_2 = 5m; U_1 = U_3 = 0$). Figure 2.11 and Figure 2.12 show the predicted gravitation and gravitational gradient changes, respectively. When compared with case II in which the dislocation vector is the same yet the dip angle is shallower, more positive signals are found in the calculated gravitation changes (Figure 2.11) since larger dip angle leads to more significant elevation changes on the surface. Again, the T_{22}, T_{33} and T_{23} components of the gravitational gradient changes (Figure 2.12) clearly delineate the edge of the fault.
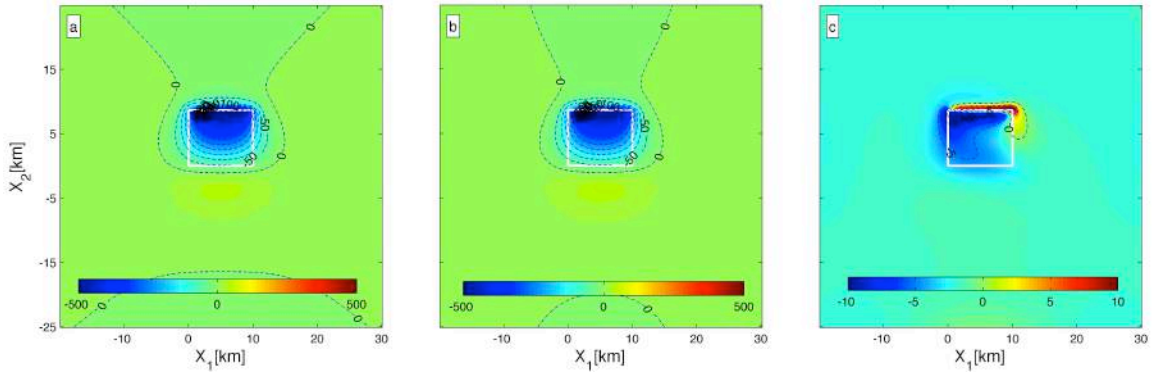

Figure 2.11: Gravitation changes in unit of μGal caused by thrust faulting: fault length, width and dip are 10km, 10km, and 60°, respectively. Depth to the top edge of the fault is 1km. White rectangular shows the edges of the fault plane. Dislocation $U_2 = 5m$. (a) Gravitation changes calculated using analytical formula; (b) Gravitation changes calculated using Fourier approach; (c) The differences between (a) and (b) shown in a different color scale.
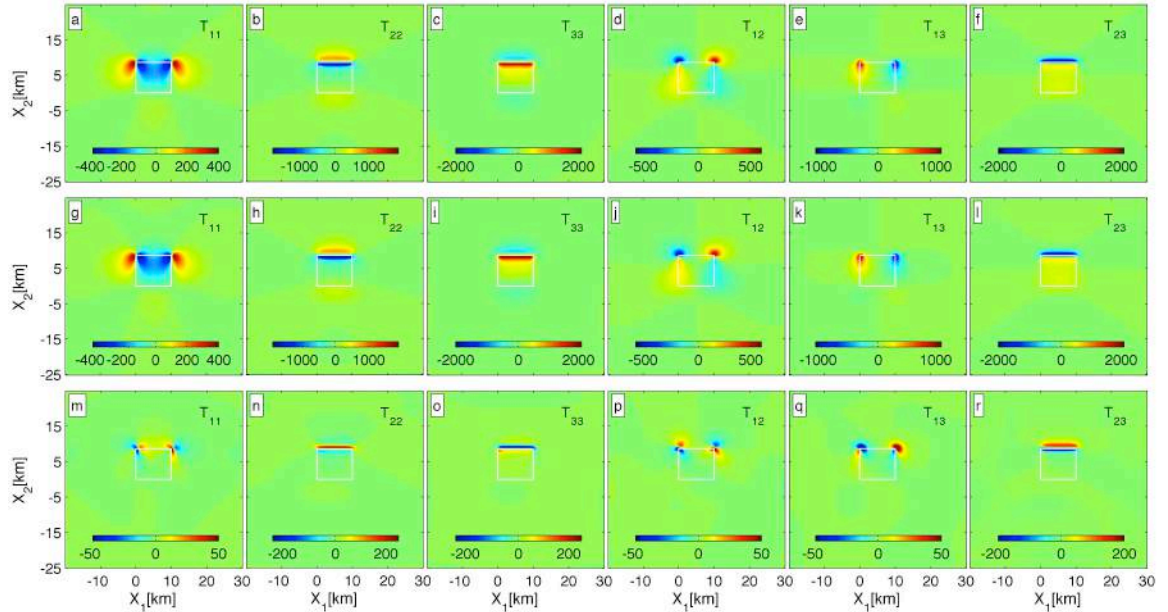
Figure 2.12: Gravitational gradient changes in unit of *mE* caused by thrust faulting: fault length, width and dip are 10km, 10km, and 60°, respectively. Depth to the top edge of the fault is 1km. White rectangular shows the edges of the fault plane. Dislocation $U_2 = 5m$. (a)~(f) Gravitational gradient changes calculated using analytical formula; (g)~(l) Gravitational gradient changes calculated using Fourier approach; (m)~(r) The differences between the results using two methods.

In case V, let's consider the gravitation and gravitational gradient changes due to strike-slip ($U_1 = 5m; U_2 = U_3 = 0$) faulting on a vertical fault plane whose size keeps the same as in previous examples. The gravitation and gravitational gradient changes show totally symmetric spatial pattern, and the positive and negative changes have equal amplitudes.
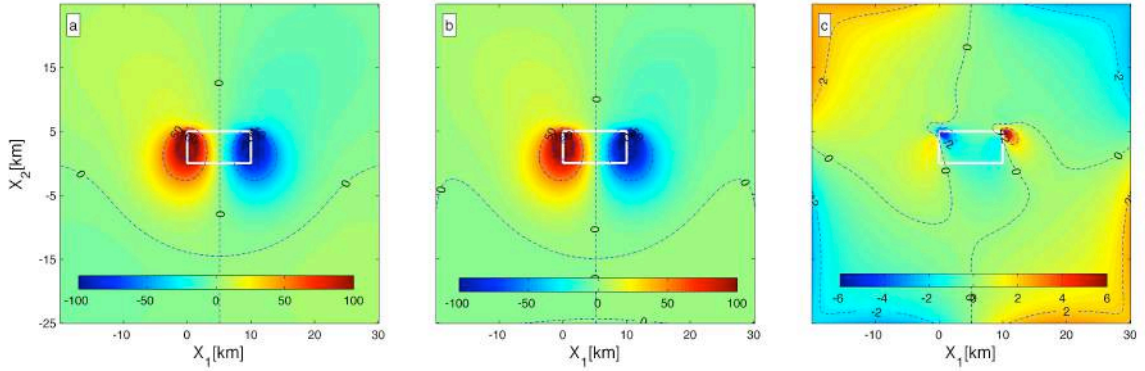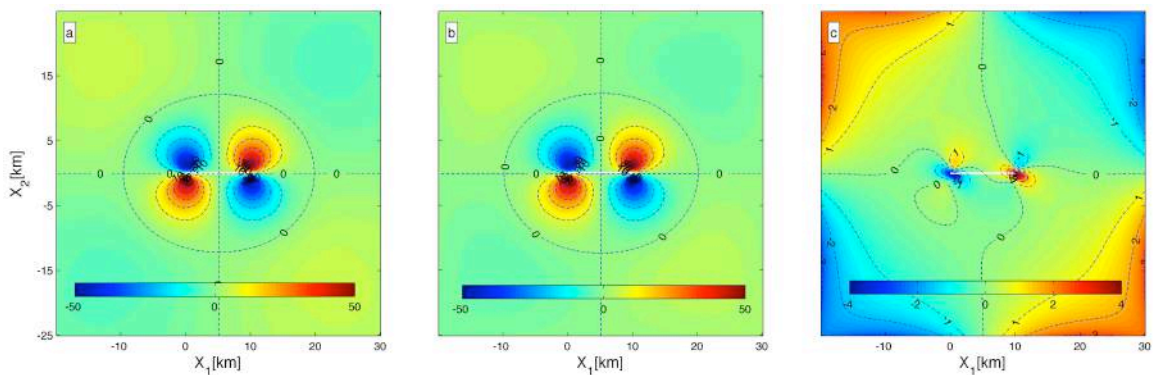

Figure 2.13: Gravitation changes in unit of μGal caused by left-lateral faulting: fault length, width and dip are 10km, 10km, and 90°, respectively. Depth to the top edge of the

fault is 1km. White rectangular shows the edges of the fault plane. Dislocation $U_1 = 5m$. (a) Gravitation changes calculated using analytical formula; (b) Gravitation changes calculated using Fourier approach; (c) The differences between (a) and (b) shown in a different color scale.
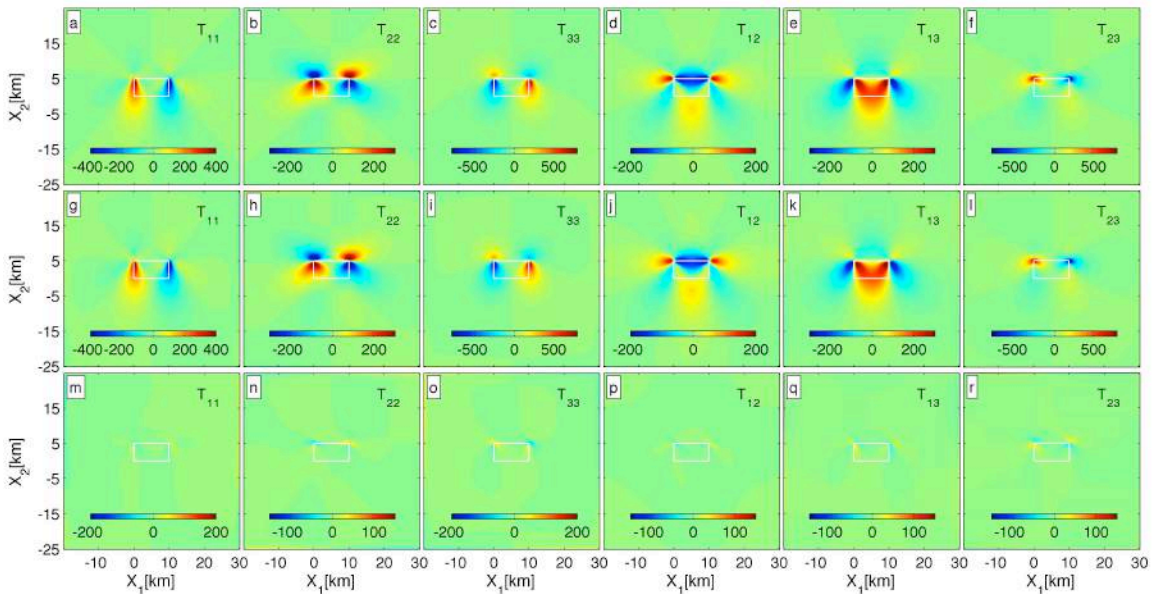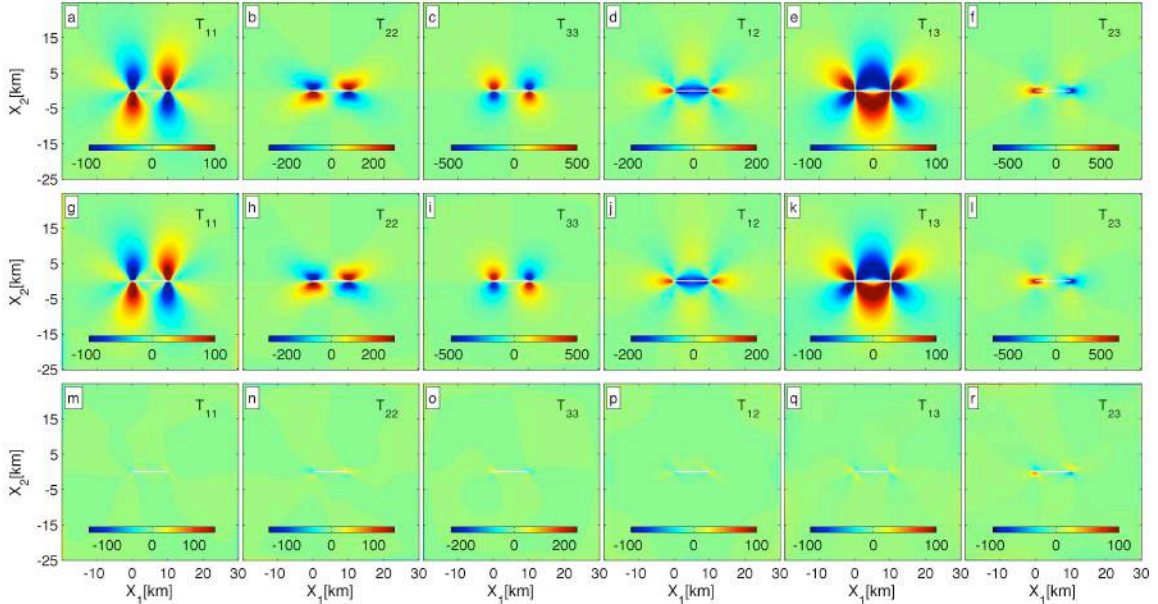

Figure 2.14: Gravitational gradient changes in unit of mE caused by left-lateral faulting: fault length, width and dip are 10km, 10km, and $90°$, respectively. Depth to the top edge of the fault is 1km. White rectangular shows the edges of the fault plane. Dislocation $U_1 = 5m$. (a)~(f) Gravitational gradient changes calculated using analytical formula; (g)~(l) Gravitational gradient changes calculated using Fourier approach; (m)~(r) The differences between the results using two methods.

In last case, the gravitation (Figure 2.15) and gravitational gradient (Figure 2.16) changes due to a thrust ($U_2 = 5m; U_1 = U_3 = 0$) faulting on the same vertical fault plane as the one used in case V are presented.
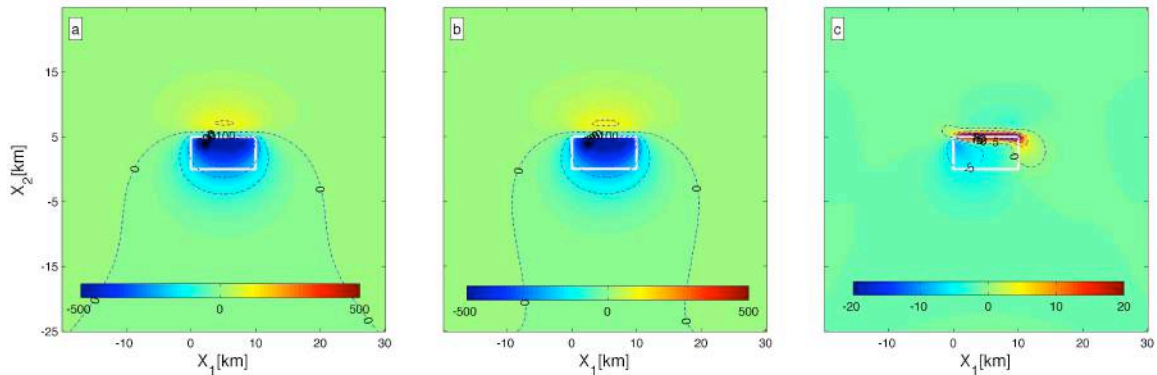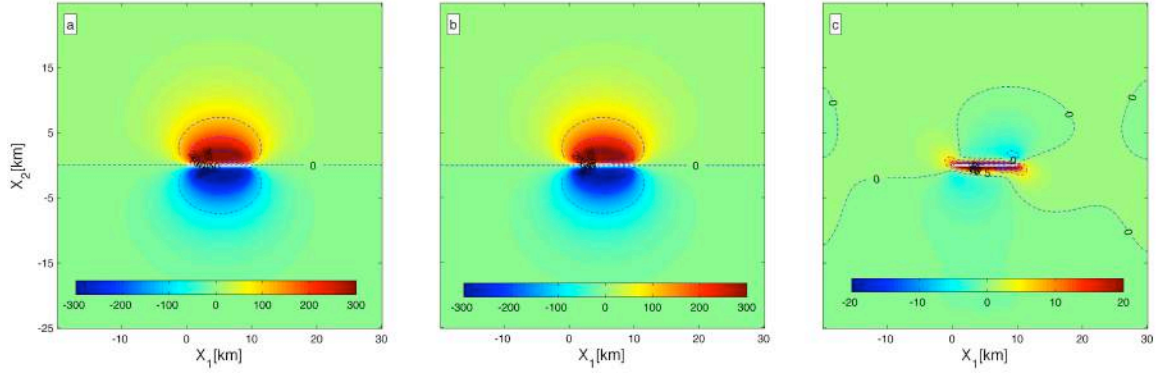
Figure 2.15: Gravitation changes in unit of *μGal* caused by thrust faulting: fault length, width and dip are 10km, 10km, and 90°, respectively. Depth to the top edge of the fault is 1km. White rectangular shows the edges of the fault plane. Dislocation $U_2 = 5m$. (a) Gravitation changes calculated using analytical formula; (b) Gravitation changes calculated using Fourier approach; (c) The differences between (a) and (b) shown in a different color scale.
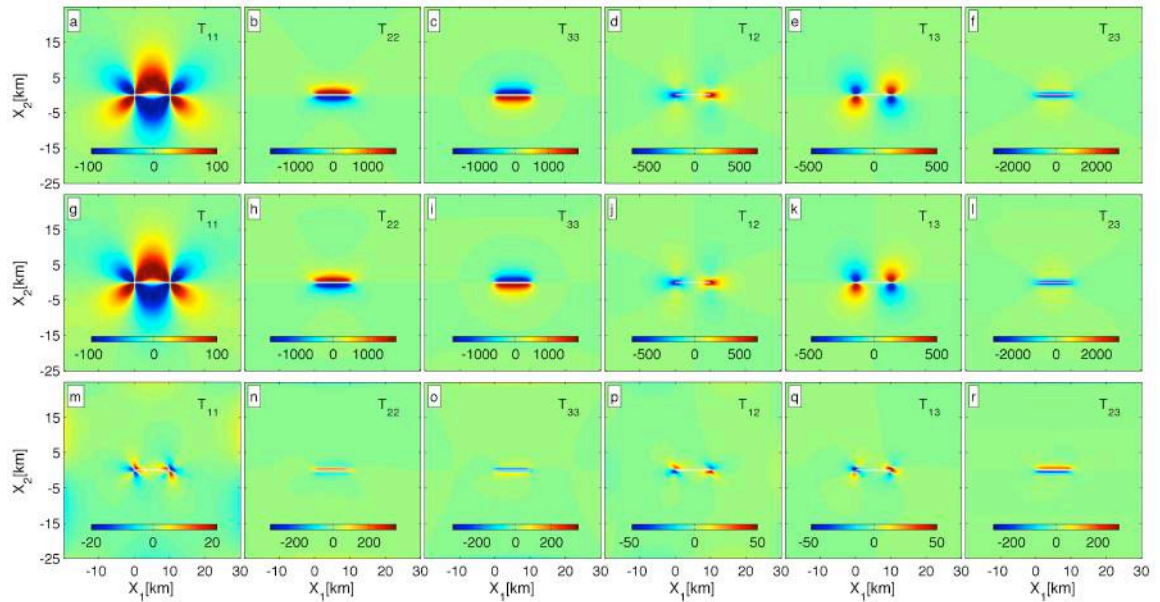
Figure 2.16: Gravitational gradient changes in unit of *mE* caused by thrust faulting: fault length, width and dip are 10km, 10km, and 90°, respectively. Depth to the top edge of the fault is 1km. White rectangular shows the edges of the fault plane. Dislocation $U_2 = 5m$. (a)~(f) Gravitational gradient changes calculated using analytical formula; (g)~(l) Gravitational gradient changes calculated using Fourier approach; (m)~(r) The differences between the results using two methods.

If the gravitation and gravitational gradient changes calculated by the analytical formulas are considered as truths, the errors induced by the numerical method can be

26

evaluated based on the differences between the results of these two methods. Table 2.1 lists the standard deviations (std) of relative errors of the estimated gravitation and gravitational gradient changes using Fourier approach.

std / fault		g $[\mu Gal]$	T_{33} $[mE]$	T_{13} $[mE]$	T_{23} $[mE]$	T_{22} $[mE]$	T_{12} $[mE]$	T_{11} $[mE]$
Dip=30°	U1=5m	0.94	11.53	8.65	8.91	8.06	1.62	8.02
	U2=5m	1.12	13.81	3.46	13.38	13.15	2.58	2.40
Dip=60°	U1=5m	1.10	10.66	8.51	7.99	7.09	1.69	7.73
	U2=5m	1.57	14.83	2.69	14.71	14.47	2.27	1.79
Dip=90°	U1=5m	1.19	8.09	6.23	6.60	5.76	1.76	5.37
	U2=5m	1.68	18.37	2.45	18.69	18.24	2.34	1.67

Table 2.1: Standard deviations of relative errors in estimated gravitation and gravitational gradient changes using Fourier approach for various faulting scenarios. The gravitation and gravitational gradient changes given by the analytical formulas are considered as 'truths'.

Table 2.1 reveals that, for both strike-slip faulting and thrust faulting, the errors in the calculated gravitation changes by Fourier approach get larger with the increasing of dip angle. The errors are larger for thrust faulting than strike-slip faulting at the same dip angle. For the gravitational gradient components of T_{33}, T_{23} and T_{22}, if the faulting is in the strike-slip sense, the errors induced by the numerical method become smaller as the dip angle increases; While for thrust faulting, the errors are larger for larger dip angles. At the same dip angle, the numerical approach induces larger errors for thrust faulting. For the components of T_{13} and T_{11}, the errors induced by the numerical methods get smaller as the dip angle increases for both strike-slip and thrust faultings. At fixed dip angle, the numerical approach induces larger errors for strike-slip faulting.

In all cases, when the numerical method is used, the standard deviations of errors in the calculated gravitation changes are less than $2\mu Gal$. The standard deviations of errors in estimated gravitational gradient changes are $< 20mE$ for T_{33}, T_{23}, T_{22}, while $< 10mE$ for T_{13}, T_{12}, T_{11} components.

Analytical formula can be used to compute the coseismic gravitation and gravitational gradient changes very fast. The Fourier approach can also be used to effectively estimate the faulting-induced gravitation and gravitational gradient changes. In order to implement the numerical method, the half-space has to be divided into grid of rectangular cells whose size must be small enough to avoid losses of high-frequency contents. For complicated slip models, which typically consist of several large fault planes, and slips keep varying from patch to patch, utilization of the Fourier approach

demands huge memory storage and computation time. However, the advantage of the numerical method is that it can take into account the effect of layered density structure of the half-space. The only elastic property controlling the displacement field and thus the dilatation filed in the half-space is the Poisson ratio, which is less variable (Okada, 1985; Lay *et al*., 2011) in crust and upper mantle of the Earth. Therefore, multiplying the dilatation (sum of normal strains) by specific densities at different depths, e.g. sediment, soft crust, hard curst, and upper mantle, we can obtain the volumetric density changes at arbitrary levels even if the half-space has layered density structure.

Chapter 3:   Spatiospectral Localization Analysis for Regional Signals

While many geophysical phenomena, such as ice-sheet melting over Greenland and Antarctica, glacial isostatic adjustment over Hudson Bay, magnetic anomaly due to bodies buried in Earth's crust and deformation caused by great earthquakes, are spatially localized, the signals associated with these geological and geophysical processes are usually extracted and analyzed from data products represented by certain basis functions having global support. The so-called spatiospectral concentration problem is to determine an orthogonal family of strictly bandlimited functions that are optimally concentrated within a closed region of the sphere or, alternatively, to determine an orthogonal family of strictly spacelimited functions that are optimally concentrated in the spherical harmonic domain (Simons *et al.,* 2006). The resulted Slepian basis function can be efficiently applied to represent and analyze regional signals, in particular the coseismic gravity changes by great earthquakes.

3.1   Slepian's Concentration Problem on Sphere

Figure 3.1 shows a unit sphere Ω. $\bar{r}$ is the location of a point on the surface of the unit sphere with colatitude θ and longitude ϕ. An arbitrary real-valued, square-integrable function $f(\bar{r})$ on the unit sphere can be expressed by spherical harmonic expansion as:

$$f(\bar{r}) = \sum_{l=0}^{\infty} \sum_{m=-l}^{l} f_{lm} Y_{lm} \tag{3.1}$$

where f_{lm} is the spherical harmonic coefficient:

$$f_{lm} = \int_{\Omega} f Y_{lm} \, d\Omega . \tag{3.2}$$

Y_{lm} denotes the spherical harmonic of degree l and order m:

$$Y_{lm}(\theta,\phi) = \begin{cases} \sqrt{2} X_{lm}(\theta)\cos m\phi, & if \quad -l \le m < 0 \\ X_{l0}, & if \quad m = 0 \\ \sqrt{2} X_{lm}(\theta)\sin m\phi, & if \quad 0 < m \le l \end{cases} \tag{3.3}$$

$$X_{lm}(\theta) = (-1)^{m} \left(\frac{2l+1}{4\pi}\right)^{1/2} \left[\frac{(l-m)!}{(l+m)!}\right]^{1/2} P_{lm}(\cos\theta) \tag{3.4}$$

$$P_{lm}(t) = \frac{1}{2^{l} l!} \left(1-t^{2}\right)^{m/2} \left(\frac{d}{dt}\right)^{l+m} \left(t^{2}-1\right)^{l} \tag{3.5}$$

In the following discussions, we use $g(\bar{r})$ to denote strictly bandlimited square-integrable functions on the unit sphere Ω:

$$g(\bar{r}) = \sum_{l=0}^{L} \sum_{m=-l}^{l} g_{lm} Y_{lm} \tag{3.6}$$

and $h(\bar{r})$ to denote strictly spacelimited square-integrable functions on Ω:

$$h(\bar{r}) = \sum_{l=0}^{\infty} \sum_{m=-l}^{l} h_{lm} Y_{lm}, \quad h(\bar{r}) = 0 \text{ in } \Omega - R \tag{3.7}$$

where R is an arbitrary spatial region on Ω, as shown in Figure 3.1.
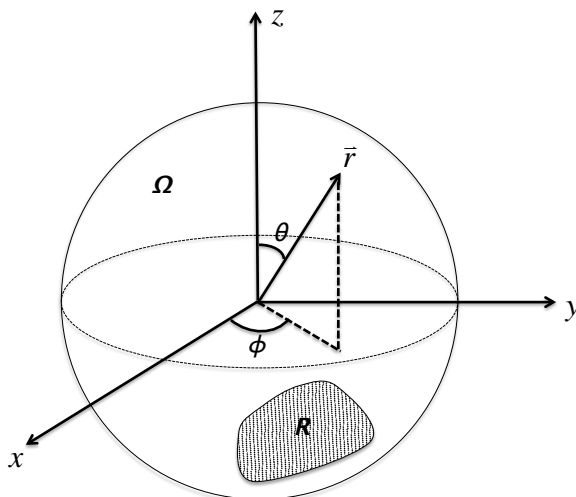
Figure 3.1: A unit sphere Ω. R is a close region of the surface.

No functions can be strictly spacelimited and at the same time strictly bandlimited. The objective of the spatiospectral concentration problem is to find bandlimited functions $g(\bar{r})$, which are optimally concentrated within a spatial region R, and to determine spacelimited functions $h(\bar{r})$ whose spectrum is optimally concentrated within an interval $0 \le l \le L$.

To maximize the spatial concentration of a bandlimited function $g(\bar{r})$ within a region R, the ratio of the norms should be maximized as:

$$\lambda = \frac{\|g\|_R^2}{\|g\|_\Omega^2} = \frac{\int_R g^2 \, d\Omega}{\int_\Omega g^2 \, d\Omega} = \text{maximum} \tag{3.8}$$

Here, the ratio $0 < \lambda < 1$ is a measure of the spatial concentration. Substituting equation (3.6) into equation (3.8), we have

$$\lambda = \frac{\displaystyle\sum_{l=0}^{L}\sum_{m=-l}^{l} g_{lm} \sum_{l'=0}^{L}\sum_{m'=-l'}^{l'} D_{lm,l'm'} g_{l'm'}}{\displaystyle\sum_{l=0}^{L}\sum_{m=-l}^{l} g_{lm}^2} \tag{3.9}$$

where

$$D_{lm,l'm'} = \int_R Y_{lm} Y_{l'm'} \, d\Omega . \tag{3.10}$$

By introducing a matrix **D** of dimension $(L+1)^2 \times (L+1)^2$:

$$\mathbf{D} = \begin{pmatrix}
D_{0,0;0,0} & \cdots & D_{0,0;L,0} & D_{0,0;1,-1} & \cdots & D_{0,0;L,-1} & D_{0,0;1,1} & \cdots & D_{0,0;L,1} & \cdots & D_{0,0;L,L} \\
\vdots & & & & & & & & & & \vdots \\
D_{L,0;0,0} & \cdots & D_{L,0;L,0} & D_{L,0;1,-1} & \cdots & D_{L,0;L,-1} & D_{L,0;1,1} & \cdots & D_{L,0;L,1} & \cdots & D_{L,0;L,L} \\
D_{1,-1;0,0} & \cdots & D_{1,-1;L,0} & D_{1,-1;1,-1} & \cdots & D_{1,-1;L,-1} & D_{1,-1;1,1} & \cdots & D_{1,-1;L,1} & \cdots & D_{1,-1;L,L} \\
\vdots & & & & & & & & & & \vdots \\
D_{L,-1;0,0} & \cdots & D_{L,-1;L,0} & D_{L,-1;1,-1} & \cdots & D_{L,-1;L,-1} & D_{L,-1;1,1} & \cdots & D_{L,-1;L,1} & \cdots & D_{L,-1;L,L} \\
D_{1,1;0,0} & \cdots & D_{1,1;L,0} & D_{1,1;1,-1} & \cdots & D_{1,1;L,-1} & D_{1,1;1,1} & \cdots & D_{1,1;L,1} & \cdots & D_{1,1;L,L} \\
\vdots & & & & & & & & & & \vdots \\
D_{L,1;0,0} & \cdots & D_{L,1;L,0} & D_{L,1;1,-1} & \cdots & D_{L,1;L,-1} & D_{L,1;1,1} & \cdots & D_{L,1;L,1} & \cdots & D_{L,1;L,L} \\
\vdots & & & & & & & & & & \vdots \\
D_{L,L;0,0} & \cdots & D_{L,L;L,0} & D_{L,L;1,-1} & \cdots & D_{L,L;L,-1} & D_{L,L;1,1} & \cdots & D_{L,L;L,1} & \cdots & D_{L,L;L,L}
\end{pmatrix} \tag{3.11}$$

with elements $D_{l,m;l',m'}$, $0 \le l(l') \le L$ and $-l \le m(m') \le l$, as well as a $(L+1)^2 \times 1$ vector of spherical harmonic coefficients g:

$$\mathbf{g} = \begin{pmatrix} g_{0,0} & \cdots & g_{L,0} & g_{1,-1} & \cdots & g_{L,-1} & g_{1,1} & \cdots & g_{L,1} & \cdots & g_{L,L} \end{pmatrix}^T, \tag{3.12}$$

which is associated with function $g(\vec{r})$, we can rewrite equation (3.9) in matrix form as:

$$\lambda = \frac{\mathbf{g}^T \mathbf{D} \mathbf{g}}{\mathbf{g}^T \mathbf{g}} = \text{maximum} \tag{3.13}$$

The concentration problem now turns out to be a classical matrix variational problem. By solving the $(L+1)^2 \times (L+1)^2$ algebraic eigenvalue problem:

$$\mathbf{D}\mathbf{g} = \lambda \mathbf{g}, \tag{3.14}$$

$(L+1)^2$ eigenvalues λ and associated eigenvectors $\mathbf{g}_1, \mathbf{g}_2, \cdots, \mathbf{g}_{(L+1)^2}$ can be determined. The eigenvalues $\lambda_1, \lambda_2, \cdots, \lambda_{(L+1)^2}$ can be sorted in descending order $(1 > \lambda_1 \ge \lambda_2 \ge \cdots \ge \lambda_{(L+1)^2})$ and correspondingly the associated spectral-domain eigenvectors $\mathbf{g}_1, \mathbf{g}_2, \cdots, \mathbf{g}_{(L+1)^2}$. Every spectral-domin eigenvector $\mathbf{g}_\alpha$ corresponds to an associated bandlimited spatial eigenfunction $g_\alpha(\vec{r})$ as defined by (3.6). The spatial

31

eigenfunction $g_1(\bar{r})$ corresponding to the largest eigenvalue of λ_1 is a bandlimited function on the unit sphere but optimally concentrated within region R, and the 2$^{\text{nd}}$ ranked eigenfunction $g_2(\bar{r})$ is the next best concentrated function, et cetera.

It can be proven that the spectrum domain eigenvectors $\mathbf{g}_1, \mathbf{g}_2, \cdots, \mathbf{g}_{(L+1)^2}$ are mutually orthogonal. They can also be chosen to be orthonormal so that:

$$\mathbf{g}_\alpha^T \mathbf{g}_\beta = \delta_{\alpha\beta}, \text{ and } \mathbf{g}_\alpha^T \mathbf{D} \mathbf{g}_\beta = \lambda_\alpha \delta_{\alpha\beta} \tag{3.15}$$

where

$$\delta_{\alpha\beta} = \begin{cases} 1, & \alpha = \beta \\ 0, & \alpha \neq \beta \end{cases} \tag{3.16}$$

is the Kronecker's delta function. In space domain, the associated spatial eigenfunctions $g_1(\bar{r}), g_2(\bar{r}), \cdots, g_{(L+1)^2}(\bar{r})$ form a set of bases spanning the space of bandlimited square-integrable functions on the unit sphere Ω. It is worth mentioning here that both Y_{lm}, $0 \le l \le L$, $-l \le m \le l$, and g_α, $\alpha = 1, 2, \cdots, (L+1)^2$, are $(L+1)^2$ - dimensinal orthogonal bases for the space of bandlimited square-integrable functions on Ω.

The sum of all the eigenvalues $\lambda_1, \lambda_2, \cdots, \lambda_{(L+1)^2}$ of the matrix $\mathbf{D}$ defined in (3.11) is:

$$N = \sum_{\alpha=1}^{(L+1)^2} \lambda_\alpha = tr(\mathbf{D}) = \sum_{l=0}^{L} \sum_{m=-l}^{l} D_{lm,lm} = (L+1)^2 \frac{A}{4\pi} \tag{3.17}$$

where A is the area of the concentration region R. The quantity N is defined as 'spherical Shannon number'. The eigenvalues λ_α are near unity for the eigenfunctions $g_\alpha(\bar{r})$ which are well concentrated within the region R, yet near zero for those poorly concentrated eigenfunctions. If the transition band from values near unity to values near zero in the eigenspectrum is narrow, the Shannon number well approximates the total number of the eigenvalues close to unity, i.e., the number of bandlimited spatial eigenfunctions having most of their energy concentrated within the region R. Thus, the first N orthogonal eigenfunctions g_α, $\alpha = 1, 2, \cdots, N$, with significant eigenvalues $\lambda_\alpha \approx 1$, provide uniform coverage of the objective region R. This is the essence of the spatiospectral concentration problem: the local signals can be essentially well approximated by using only N (spherical Shannon number) Slepian basis functions.

As an example, following text discusses the localization problem for a special but important case, i.e., concentration within a circularly symmetric polar cap of colatitudinal radius Θ, centered on the north pole (see Figure 3.2).
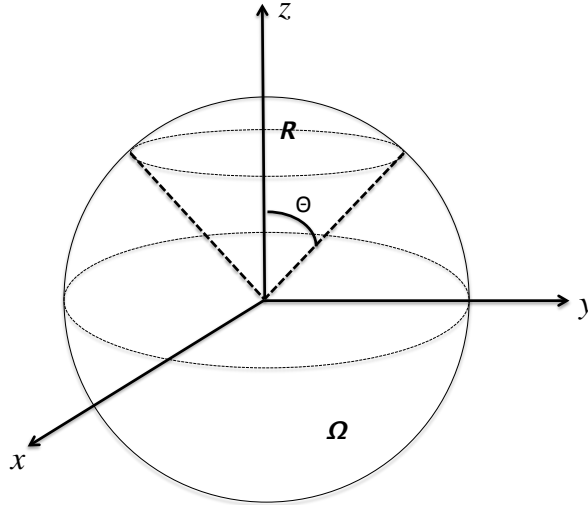
Figure 3.2: An axisymmetric polar cap of colatitudinal radius Θ, centered on the north pole.

In this circumstance, the matrix elements $D_{lm,l'm'}$ as given by equation (3.10) reduce to:

$$D_{lm,l'm'} = \int_R Y_{lm} Y_{l'm'} \, d\Omega$$
$$= 2\pi \delta_{mm'} \int_0^\Theta X_{lm} X_{l'm'} \sin\theta \, d\theta$$

(3.18)

The Kronecker's delta $\delta_{mm'}$ makes the $(L+1)^2 \times (L+1)^2$ matrix $\mathbf{D}$ of (3.11) block diagonal:

$$\mathbf{D} = \begin{pmatrix} \mathbf{D}_0 & & & & & \\ & \mathbf{D}_1 & & & & \\ & & \mathbf{D}_1 & & & \\ & & & \ddots & & \\ & & & & \mathbf{D}_L & \\ & & & & & \mathbf{D}_L \end{pmatrix}$$

$$
= \begin{pmatrix}
D_{0,0;0,0} & \cdots & D_{0,0;L,0} \\
\vdots & & \vdots \\
D_{L,0;0,0} & \cdots & D_{L,0;L,0} \\
& & & D_{1,-1;1,-1} & \cdots & D_{1,-1;L,-1} \\
& & & \vdots & & \vdots \\
& & & D_{L,-1;1,-1} & \cdots & D_{L,-1;L,-1} \\
& & & & & & D_{1,1;1,1} & \cdots & D_{1,1;L,1} \\
& & & & & & \vdots & & \vdots \\
& & & & & & D_{L,1;1,1} & \cdots & D_{L,1;L,1} \\
& & & & & & & & & \ddots \\
& & & & & & & & & & D_{L,L;L,L}
\end{pmatrix}
$$

$$(3.19)$$

Every submatrix $\mathbf{D}_m$ ($m \neq 0$) occurs twice because of the doublet degeneracy associated with $\pm m$. Thus, the eigenvalue problem in equation (3.14) can be decomposed into a series of $(L-m+1) \times (L-m+1)$ spectral-domain algebraic eigenvalue problems:

$$\mathbf{D_m g_m} = \lambda_m \mathbf{g_m}, \tag{3.20}$$

one for each non-negative order m. In the following text, the identifying subscript m is dropped, and each fixed-order eigenvalue problem is simply written as:

$$\mathbf{Dg} = \lambda \mathbf{g} \tag{3.21}$$

where

$$
\mathbf{D} = \begin{pmatrix}
D_{mm} & \cdots & D_{mL} \\
\vdots & & \vdots \\
D_{Lm} & \cdots & D_{LL}
\end{pmatrix}, \quad \text{and} \quad \mathbf{g} = \begin{pmatrix}
g_m \\
\vdots \\
g_L
\end{pmatrix}. \tag{3.22}
$$

For a particular order $0 \le m \le L$ and $m \le l \le L$,

$$D_{ll'} = D_{l,m;l',m} = 2\pi \int_0^\Theta X_{lm} X_{l'm} \sin\theta \, d\theta \tag{3.23}$$

Equation (3.23) can be evaluated as:

$$D_{ll'} = (-1)^m \frac{\sqrt{(2l+1)(2l'+1)}}{2} \sum_{n=|l-l'|}^{l+l'} \begin{pmatrix} l & n & l' \\ 0 & 0 & 0 \end{pmatrix} \begin{pmatrix} l & n & l' \\ m & 0 & -m \end{pmatrix} \left[P_{n-1}(\cos\Theta) - P_{n+1}(\cos\Theta) \right],$$

$$(3.24)$$

where the arrays of indices are Wigner 3-*j* symbols.

By solving each of the fixed-order eigenvalue problem (3.21), we obtain *L-m*+1 eigenvectors $\mathbf{g}_1, \mathbf{g}_2, \cdots, \mathbf{g}_{L-m+1}$ associated with the *L-m*+1 distinct eigenvalues

$1 > \lambda_1 > \lambda_2 > \cdots > \lambda_{L-m+1} > 0$. These eigenvectors can be orthonormalized as in (3.15) so that:

$$\mathbf{g}_\alpha^{\mathrm{T}}\mathbf{g}_\beta = \delta_{\alpha\beta}, \quad \text{and} \quad \mathbf{g}_\alpha^{\mathrm{T}}\mathbf{D}\mathbf{g}_\beta = \lambda_\alpha\delta_{\alpha\beta}. \tag{3.25}$$

Consequently, the associated bandlimited colatitudinal eigenfunctions $g_1(\theta), g_2(\theta), \cdots, g_{L-m+1}(\theta)$, which are defined by:

$$g(\theta) = \sum_{l=m}^{L} g_l X_{lm}(\theta), \tag{3.26}$$

satisfy the orthogonality relations:

$$2\pi\int_0^\pi g_\alpha g_\beta \sin\theta\, d\theta = \delta_{\alpha\beta}, \quad \text{and} \quad 2\pi\int_0^\Theta g_\alpha g_\beta \sin\theta\, d\theta = \lambda_\alpha\delta_{\alpha\beta}. \tag{3.27}$$

Finally, the optimally concentrated spatial eigenfunctions $g(\bar{r})$ for a given order $-L \le m \le L$ are expressed in terms of spherical harmonic expansion:

$$g(\theta,\phi) = \begin{cases} \sqrt{2}g(\theta)\cos m\phi & \text{if} \quad -L \le m < 0, \\ g(\theta) & \text{if} \quad m = 0, \\ \sqrt{2}g(\theta)\sin m\phi & \text{if} \quad 0 < m \le L. \end{cases} \tag{3.28}$$

After obtaining the $L+1$ sets of fixed-order eigenvalues, we can resort all the $(L+1)^2$ eigenvalues to exhibit an overall mixed-order ranking. As discussed before, there are roughly N (spherical Shannon number) eigenfunctions optimally concentrated within the polar cap.

Figure 3.3 shows the reordered, mixed-m eigenvalue spectra for four different polar caps, with colatitudinal radii $\Theta = 10°, 20°, 30°,$ and $40°$. The maximum spherical harmonic degree is $L=20$. The well concentrated eigenfunctions $(\lambda \ge 0.5)$ are separated from the more poorly concentrated ones $(\lambda < 0.5)$ roughly by the rounded Shannon numbers N, which are $N = 3, 13, 30$ and 52 in all four cases.
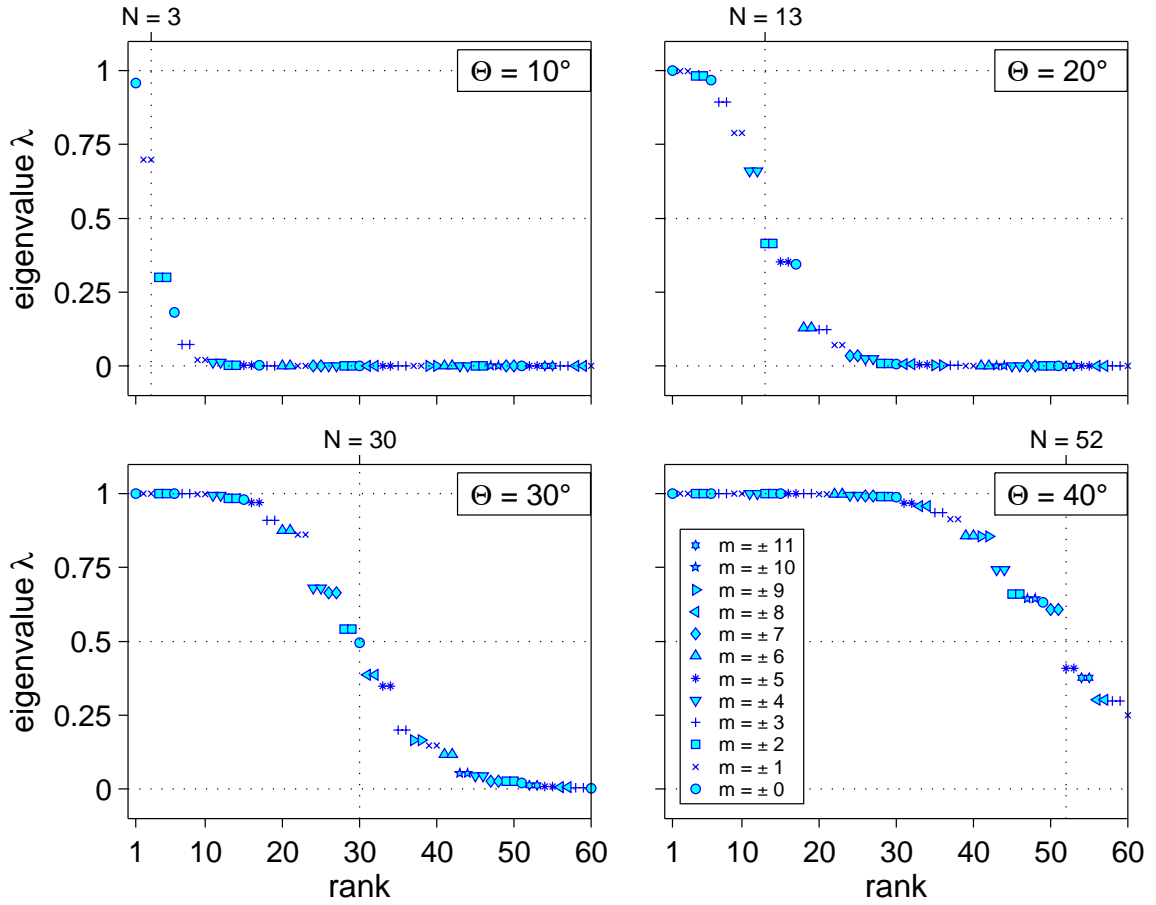
Figure 3.3: Sorted eigenvalues (λ_α versus rank α) for symmetric polar caps of colatitudinal radius $\Theta = 10°, 20°, 30°$ and $40°$, and the maximum spherical harmonic degree L=20. Only λ_1 through λ_{60} among the total $(L+1)^2 = 441$ eigenvalues are shown.

Figure 3.4 shows the first 32 eigenfunctions $g(\theta, \phi)$ concentrated with a polar cap of radius 40° as defined by equation (3.28). The maximum bandwidth is spherical harmonic degree of 20. The spherical Shannon number is N=52.

λ₁ = 1.000 ; m = 0   λ₁ = 1.000 ; m = −1   λ₁ = 1.000 ; m = 1   λ₁ = 1.000 ; m = −2

$\lambda_1 = 1.000$; $m = 0$ $\lambda_1 = 1.000$; $m = -1$ $\lambda_1 = 1.000$; $m = 1$ $\lambda_1 = 1.000$; $m = -2$

$\lambda_1 = 1.000$; $m = 2$ $\lambda_2 = 1.000$; $m = 0$ $\lambda_1 = 1.000$; $m = -3$ $\lambda_1 = 1.000$; $m = 3$

$\lambda_2 = 1.000$; $m = -1$ $\lambda_2 = 1.000$; $m = 1$ $\lambda_1 = 1.000$; $m = -4$ $\lambda_1 = 1.000$; $m = 4$

$\lambda_2 = 1.000$; $m = -2$ $\lambda_2 = 1.000$; $m = 2$ $\lambda_3 = 1.000$; $m = 0$ $\lambda_1 = 1.000$; $m = -5$

$\lambda_1 = 1.000$; $m = 5$ $\lambda_2 = 0.999$; $m = -3$ $\lambda_2 = 0.999$; $m = 3$ $\lambda_3 = 0.999$; $m = -1$

$\lambda_3 = 0.999$; $m = 1$ $\lambda_1 = 0.999$; $m = -6$ $\lambda_1 = 0.999$; $m = 6$ $\lambda_2 = 0.995$; $m = -4$

$\lambda_2 = 0.995$; $m = 4$ $\lambda_1 = 0.991$; $m = -7$ $\lambda_1 = 0.991$; $m = 7$ $\lambda_3 = 0.990$; $m = -2$

$\lambda_3 = 0.990$; $m = 2$ $\lambda_4 = 0.988$; $m = 0$ $\lambda_2 = 0.967$; $m = -5$ $\lambda_2 = 0.967$; $m = 5$
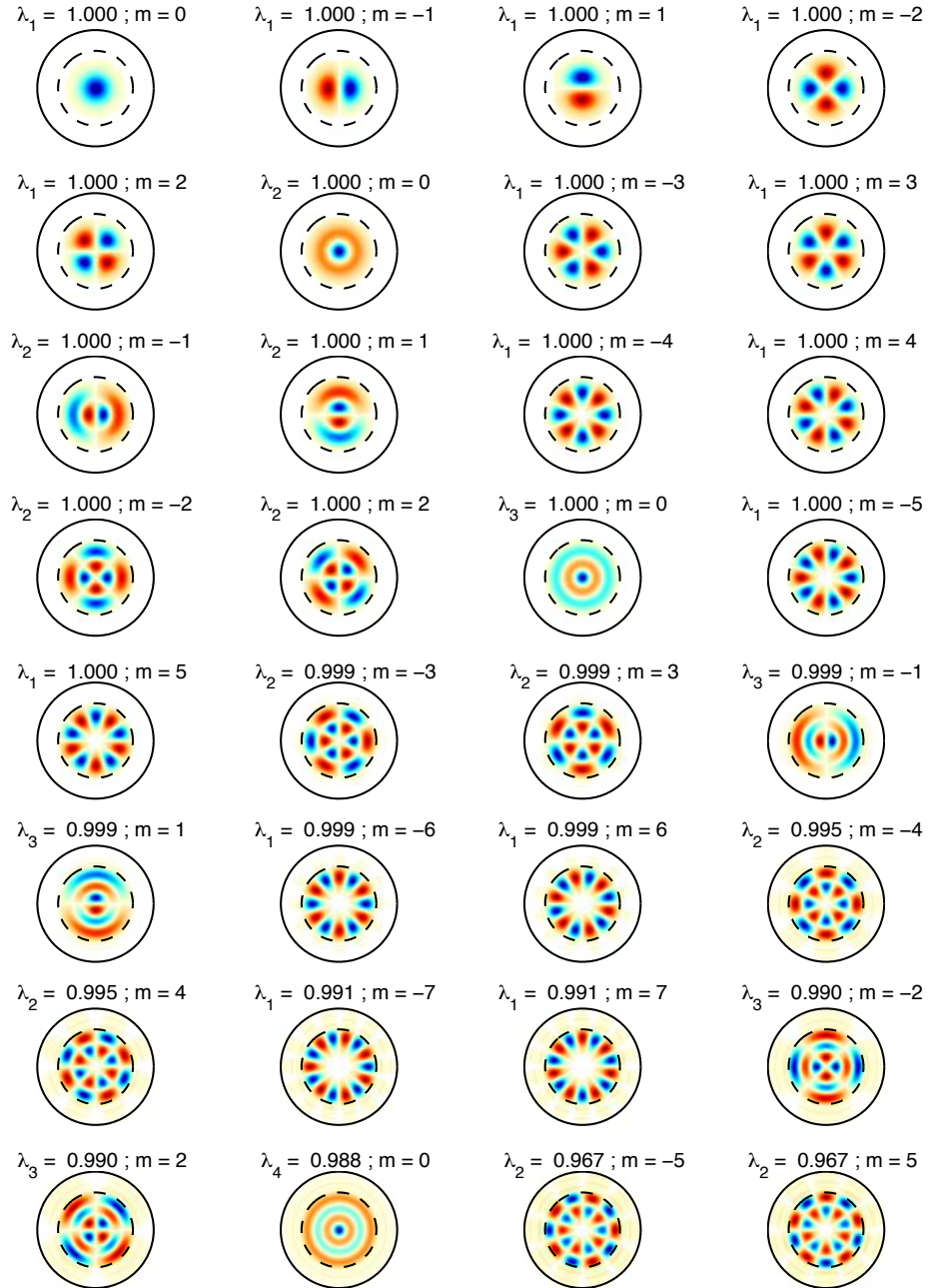
Figure 3.4: Bandlimited eigenfunctions $g(\theta, \phi)$ that are optimally concentrated within an axisymmetric polar cap of colatitudinal radius $\Theta = 40°$, whose boundary is denoted by dashed circles. The bandwidth is *L*=20, and the rounded Shannon number is *N*=52. Subscripts on the eigenvalues λ_α specify the rank for fixed-order *m*. The eigenvalues have been resorted into a mixed-order ranking, and the top 32 best concentrated eigenfunctions are plotted. Blue indicates positive values and red indicates negative

values; regions having the absolute value less than 1/100 of the maximum value on the sphere are left white.

3.2   Sparsity in Slepian Localization Analysis

3.2.1   Sparsity From Geometry

Geophysical signals that are regional in nature are sparse in the Slepian domain if the Slepian basis is designed to be concentrated within the same region as the signals reside in. The signal of interest can be expressed by spherical harmonic expansion as in equation (3.1). Although the bandwidth of signal in real world can be infinite, in practice it is often represented or estimated up to certain maximum spherical harmonic degree L, i.e.,

$$\hat{f}(\bar{r}) = \sum_{l=0}^{L} \sum_{m=-l}^{l} \hat{f}_{lm} Y_{lm}(\bar{r}).$$

(3.29)

Alternatively, it can be expanded using the Slepian basis designed for certain concentration region:

$$\hat{f}(\bar{r}) = \sum_{\alpha=1}^{(L+1)^2} \hat{f}_{\alpha} g_{\alpha}(\bar{r})$$

(3.30)

In equation (3.29) and (3.30), the spherical harmonics Y_{lm} and the corresponding expansion coefficients $\hat{f}_{lm}$ are indexed by the integer degree l and order m, and the Slepian basis functions g_{α} and expansion coefficients $\hat{f}_{\alpha}$ by the linear index α. The expression by spherical harmonic basis (3.29) and the one using the Slepian basis (3.30) are completely equivalent, since the Slepian basis for bandlimited functions everywhere on the sphere is complete, and the transformation from the spherical harmonic to the Slepian basis is unitary. When the signal of interest, $f(\bar{r})$, is spatially localized, and the Slepian basis is designed to be concentrated inside the same region, the signal can be very well approximated by a truncated Slepian expansion limited to the first N (spherical Shannon number) terms:

$$\hat{f}(\bar{r}) = \sum_{l=0}^{L} \sum_{m=-l}^{l} \hat{f}_{lm} Y_{lm}(\bar{r}) = \sum_{\alpha=1}^{(L+1)^2} \hat{f}_{\alpha} g_{\alpha}(\bar{r}) \approx \sum_{\alpha=1}^{N} \hat{f}_{\alpha} g_{\alpha}(\bar{r}),$$

(3.31)

since the first N Slepian basis functions have their energy optimally concentrated within the region, while the remaining $(L+1)^2 - N$ basis functions are mostly defined outside the concentration region. In other words, a local bandlimited signal (with maximum bandwidth of L) can be well approximated by using only N Slepian coefficients instead of $(L+1)^2$ spherical harmonic expansion coefficients. The efficiency gained by using Slepian representation depends on the area of the region of interest as shown in equation (3.17). Thus, we say this sparsity is mostly "geometric" (Simons *et al.,* 2009).

For illustration, the coseismic gravity changes from 2010 Mw 8.8 Maule earthquake is represent using both spherical harmonics and the Slepian functions. With the assumption of a homogeneous half-space, the coseismic gravity changes can be computed from a seismically derived faulting model (USGS, 2010) up to degree and order 100. Figure 3.5a shows the coseismic gravity changes represented using all 10,201 spherical harmonic coefficients. Figure 3.5d reveals that among those only 5,598 coefficients are significant contributors to the signal, in that they have absolute values that are larger than one hundredth of the maximum of the entire set. Figure 3.5b shows the approximation of the same coseismic gravity changes, but only using the first $N = 77$ best-localized Slepian functions in the expansion. Compared to Figure 3.5a, the coseismic gravity changes inside of the concentration region are extremely well captured by the partial sum of the first $N = 77$ terms in the Slepian expansion, since only 50, belonging to those with the highest concentration ratios, have significant values, as shown in Figure 3.5e. This example shows one of the advantages of making expansions in the Slepian basis: band-limited geophysical signals that are regional in nature are sparse in this sense. The root mean squared misfit of the expansions, which are shown in Figure 3.5c, is 0.05% of the signal when calculated over the entire sphere, and 0.14% of the signal when calculated over the circular concentration region.
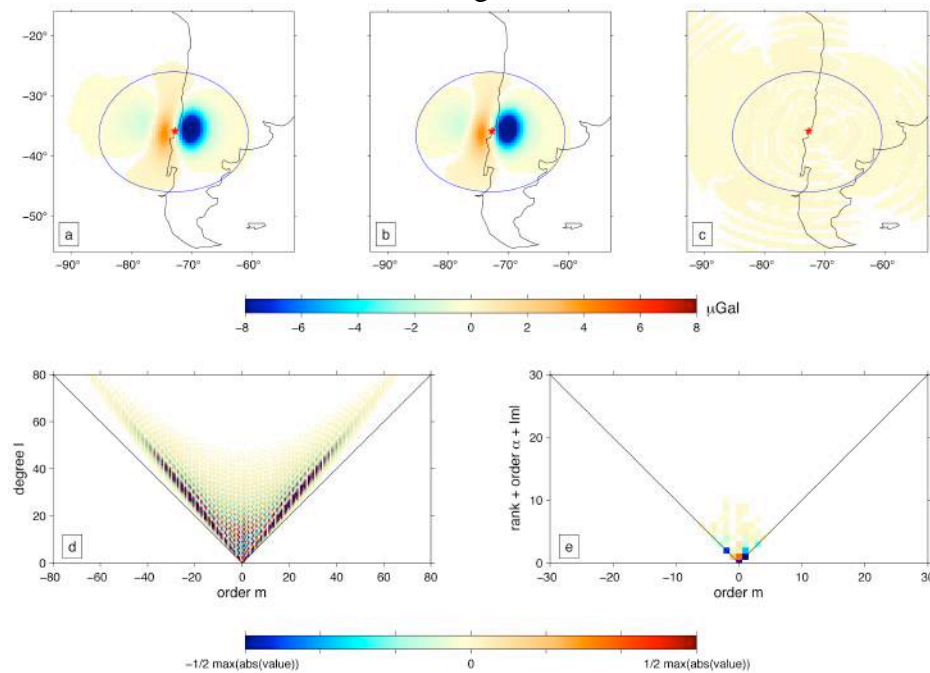
Figure 3.5: The useful sparsity that results from expanding localized geophysical signals in a Slepian basis. (a) Model-predicted coseismic gravity changes for 2010 Mw 8.8 Maule earthquake, bandlimited to spherical harmonic degree and order 100; (b) an approximation of the same coseismic gravity changes using the $N = 77$ best-localized of the 10201 Slepian functions concentrated to a circular region centered at the epicenter with radius of 10°; (c) the differences between the spherical-harmonic representation in

(a) and the Slepian-function representation in (b); (d) the corresponding 10201 spherical harmonic expansion coefficients; and (e) their Slepian expansion coefficients, using the same color scheme. Values whose absolute value is smaller than 1/100 of their maximum absolute value are rendered white. The ordinate is the sum of the rank α of the Slepian function within a sequence of single absolute order and this order of $|m|$. Only a small number of Slepian functions are needed for an adequate representation of the signal in the target region.

3.2.2 Sparsity From Geophysics

The top-ranked Slepian basis functions on circular concentration regions, fortuitously, match the patterns of the geopotential perturbation generated by coseismic deformation.

In a spherical coordinate system, the hypocenter of an earthquake is at $\vec{r}_s = (r_s, \theta_s, \phi_s)$. The equivalent body forces for seismic sources of different geometries at $\vec{r}_s$ are represented by the seismic moment tensor in spherical coordinate:

$$\mathbf{M} = \begin{pmatrix} M_{rr} & M_{r\theta} & M_{r\phi} \\ M_{\theta r} & M_{\theta\theta} & M_{\theta\phi} \\ M_{\phi r} & M_{\phi\theta} & M_{\phi\phi} \end{pmatrix} \tag{3.32}$$

For simplicity, the symmetric moment tensor in above equation can be vectorized as:

$$\mathbf{M} = \begin{bmatrix} M_{rr}, M_{\theta\theta}, M_{\phi\phi}, M_{r\theta}, M_{r\phi}, M_{\theta\phi} \end{bmatrix} \tag{3.33}$$

According to normal-mode theory, Simons *et al.* (2009) showed that the first-order Eulerian gravitational potential perturbations in a spherically-symmetric non-rotating Earth due to a variety of earthquake focal-mechanism end-members form patterns that are similar to the shape of some of the best-concentrated Slepian functions on symmetric spherical cap. To be specific, the gravitational potential perturbations induced by a variety of fictitious earthquake sources at Japan trench are shown in Figure 3.6. The symmetries of monopoles, dipoles and quadrupoles can be found in the patterns of gravitational perturbations by various seismic sources. Fortuitously, the shapes of top five Slepian functions, which are shown in Figure 3.4, match the patterns with which moment-tensor point source earthquakes perturb Earth's geopotential field as shown in Figure 3.6. This is an additional advantage by which the Slepian basis functions are particularly suitable to represent and analyze coseismic gravity changes.

40
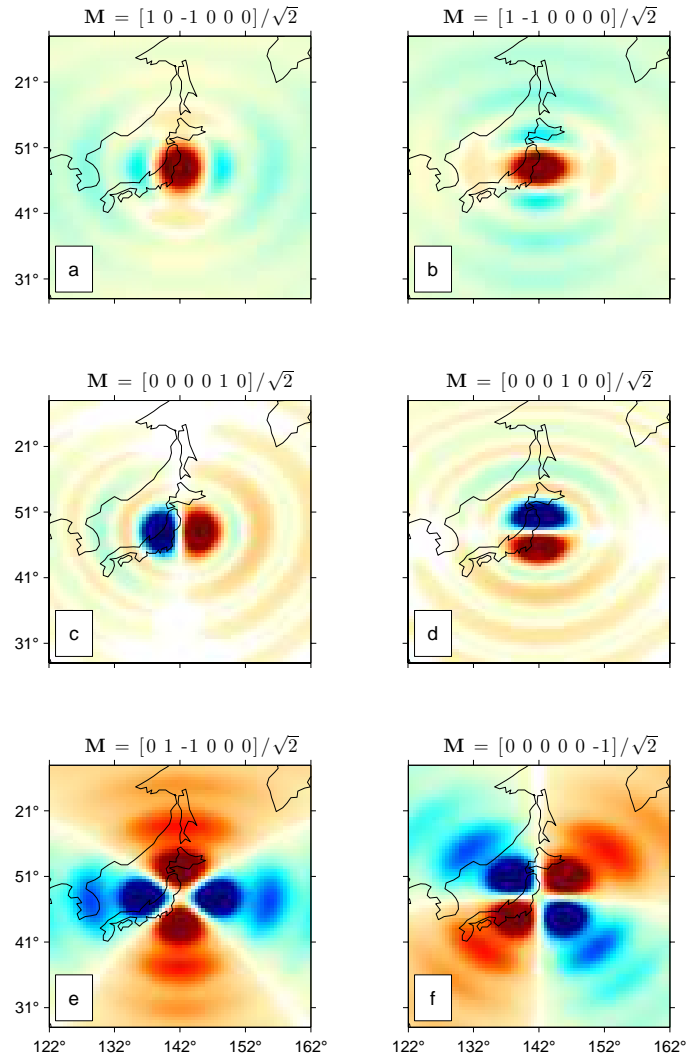
Figure 3.6: The spatial pattern of gravitational potential disturbance owing to fictitious double-coupled point-source earthquake occurring at depth of 30km along the Japan trench. The calculation is based on the normal-mode theory, and the Preliminary Reference Earth model (PREM) is assumed. The maximum spherical degree is L=60. Blue and red colors indicate positive and negative signals respectively, and the color axis is symmetric. (a)~(b) 45$^{\mathrm{o}}$ thrust faults. (c)~(d) Vertical dip-slip faults. (e)~(f) Vertical strike-slip faults.

41

Chapter 4:   Monte Carlo Inversion

During the earthquake, slips on the rupture interface induce mass movement in surrounding crust/upper mantle and consequently perturb the local gravity field. The earthquake induced mass redistribution, which can be detected by spaceborne gravimetry, is related to slips on the buried fault plane via Volterra's formula (Aki and Richards, 2002). Thus, it is possible to use the detected gravity change, as an independent thus valuable observation, to inversely constrain the slip and fault geometry of the earthquake. However, to invert for fault parameters from coseismic gravity changes is a strongly nonlinear problem as can be seen in Chapter 2. Furthermore, the gravity inverse problem is an ill-posed problem, and the solution faces the problem of non-uniqueness. Thus, the Monte Carlo method is applied for gravity inversion in the study.

Modern Monte Carlo methods, defined as "experiments making use of random numbers to solve problems that are either probabilistic or deterministic in nature" (Sambridge and Mosegaard, 2002), are first used in the work on the atomic bomb during World War II to simulate the neutron diffusion. Since then, the Monte Carlo methods have been applied to a vast range of problems in physics, mathematics, biology, chemistry and geophysics etc.

One important application of Monte Carlo methods is to realize the optimization in inverse problem. Inverse problems are typically ill-posed, linear inversion procedure based on matrix inversion suffers from numerical instabilities, such as inverting ill-conditioned matrices. Compared with linear or linearized inversion schemes, the Monte Carlo methods directly sample the parameter space, and thereby are inherently stable in the sense that no potentially numerical unstable processes are involved. Furthermore, although linear inversion technique could always give a unique solution for weakly nonlinear inverse problem via linearization and regularization, it cannot be applied if either the inverse problem is highly nonlinear or it is practically impossible for the problem to be linearized. The Monte Carlo method can still be utilized since it only requires the capability to implement forward modeling.

The core of all Monte Carlo methods is to randomly sample (or 'search') the parameter space by an efficient algorithm. For most problems, the searching range is preferred to be gradually confined in particular 'promising' regions in the parameter space (non-uniform sampling). Otherwise, huge computation time would be required in order to find the optimal solution. Among various sampling algorithms, Metropolis-Hastings algorithm (Metropolis *et al.,* 1953), which belongs to the class of Markov Chain Monte Carlo (MCMC) algorithms, is widely used to search the parameter space in a way that the states leading to smaller data-model misfits have larger chances to be sampled.

Based on Metropolis-Hastings algorithm, the Simulated Annealing (SA) method, first introduced by Kirkpatrick *et al.* (1983), searches for the global optimum via a procedure analogous to the process of chemical annealing.

In section 4.1, the Metropolis-Hastings sampling algorithm is first explained in details, as it is the basis of the SA method, which is introduced in section 4.2. Finally, two numerical applications are given in section 4.3.

4.1   Metropolis-Hastings Algorithm

Metropolis-Hastings algorithm is a kind of Markov Chain Monte Carlo (MCMC) algorithm designed to generate a sequence of random samples from a target probability distribution P over a high-dimensional space. When no explicit mathematical expressions exist for the probability distribution P, the samples generated by the Metropolis-Hastings algorithm can be used to effectively approximate or 'visualize' the distribution. Following the basic theories about Markov Chain model given in Appendix F, the Metropolis-Hastings algorithm is explained in detail below.

Assume at epoch $t = 0$ the system is at state l. Notation $P_l^{(t)}$ is used here to denote the probability of the state l at epoch t, i.e., $P(X(t) = l)$, where $X(t)$ is the state of the system at epoch t. The evolution of probability $P_l^{(t)}$ follows the "master equation":

$$P_l^{(t+1)} - P_l^{(t)} = \sum_{m \neq l} \left[P_m^{(t)} p_{ml} - P_l^{(t)} p_{lm} \right] \tag{4.1}$$

where p_{lm} is the 1-step transition probability from state m to state l. The first term on the right hand side is the probability of transitions from state m to state l, while the second term gives the probability for transitions out of state l. The objective is to design a transition probability p_{ij} so that the Markov chain converges to a target stationary distribution.

To assume a target stationary (equilibrium) distribution P^{eq} is reached, equation (4.1) turns out to be:

$$\sum_m \left(P_m^{eq} p_{ml} - P_l^{eq} p_{lm} \right) = 0. \tag{4.2}$$

Equation (4.2) means that $\dfrac{dP_l^{(t)}}{dt} = 0$, i.e. the system is at equilibrium.

Given the fact $\sum_m p_{lm} = 1$, it can be easily derived from (4.2) that:

$$P_l^{eq} = \sum_m P_m^{eq} p_{ml} \tag{4.3}$$

In practice, equilibrium in (4.2) is usually accomplished by making each term in the summation zero, i.e.

$$P_m^{eq} p_{ml} = P_l^{eq} p_{lm}. \tag{4.4}$$

Equation (4.4) is known as the "detailed balance condition" or "microscopic reversibility", which means that the probabilities of the transitions between two states (i.e. the transition from m to l and the transition from l to m) are the same at all time. If each pair of states in state space satisfies the detailed balance condition as given by (4.4), the overall equilibrium sampling is realized for the target distribution P^{eq}. Any designed transition probability p_{ij} satisfying the microscopic reversibility can be used to

continuously sample the target probability distribution (e.g. P^{eq}).

Equation (4.4) can be further written in the form of ratio:

$$\frac{p_{lm}}{p_{ml}} = \frac{P_m^{eq}}{P_l^{eq}} \tag{4.5}$$

There are infinitely many choices for transition probability that satisfy equation (4.4) or (4.5). The Metropolis-Hastings algorithm uses a simple transition probability p_{ij} given by:

$$p_{ij} = \frac{1}{N} \min\left(1, \frac{P_i^{eq}}{P_j^{eq}}\right). \tag{4.6}$$

In practice, this transition probability is realized in following way: first, to assume current state visited by the algorithm is i. Each point in the N neighbors of i has equal probability of

$$P_{proposal} = 1/N \tag{4.7}$$

to be proposed as the state for next epoch. When a new state, say j, is proposed, it is accepted only with probability:

$$P_{accept} = \min\left(1, \frac{P_i^{eq}}{P_j^{eq}}\right) \tag{4.8}$$

Therefore, the transition probability from state i to state j is:

$$p_{ij} = \frac{1}{N} \min\left(1, \frac{P_i^{eq}}{P_j^{eq}}\right) \tag{4.9}$$

Equation (4.9) indeed satisfies the microscopic reversibility in (4.5), since

$$\text{when} \quad \frac{P_i^{eq}}{P_j^{eq}} \le 1, \quad \frac{p_{ij}}{p_{ji}} = \frac{\min\left(1, \frac{P_i^{eq}}{P_j^{eq}}\right)}{\min\left(1, \frac{P_i^{eq}}{P_j^{eq}}\right)} = \frac{P_i^{eq}}{P_j^{eq}}, \tag{4.10}$$

$$\text{when } \frac{P_i^{eq}}{P_j^{eq}} > 1, \ \frac{p_{ij}}{p_{ji}} = \frac{\min\left(1, \dfrac{P_i^{eq}}{P_j^{eq}}\right)}{\min\left(1, \dfrac{P_j^{eq}}{P_i^{eq}}\right)} = \frac{1}{P_j^{eq}/P_i^{eq}} = \frac{P_i^{eq}}{P_j^{eq}}. \tag{4.11}$$

It can be seen from equation (4.9) that to decide whether or not to accept a new state j requires knowledge about the probabilities of current state P_i^{eq} and the proposed state P_j^{eq}, not the absolute probabilities, but just the ratio between them. In geophysical inversion, P^{eq} is usually a probability density derived from a certain data-model misfit function, e.g. the Gibbs-Boltzmann Distribution function given in next section.

To numerically illustrate the Metropolis-Hastings algorithm, a system is assumed to have a state space consisting of two variables, x and y. The target probability density function is assumed to be inversely proportional to the Rosenbrock function, which is defined on the 2D infinite domain ($-\infty < x < \infty$, $-\infty < y < \infty$) as:

$$f(x, y) = (1 - x)^2 + 100 \cdot (y - x^2)^2. \tag{4.12}$$

The Rosenbrock function has a global minimum of 0 at the point (1, 1) locating in a parabolic shaped valley as shown in Figure 4.1. A Markov chain with initial point at (0,2.5) is run on the Rosenbrock function using the Metropolis algorithm.
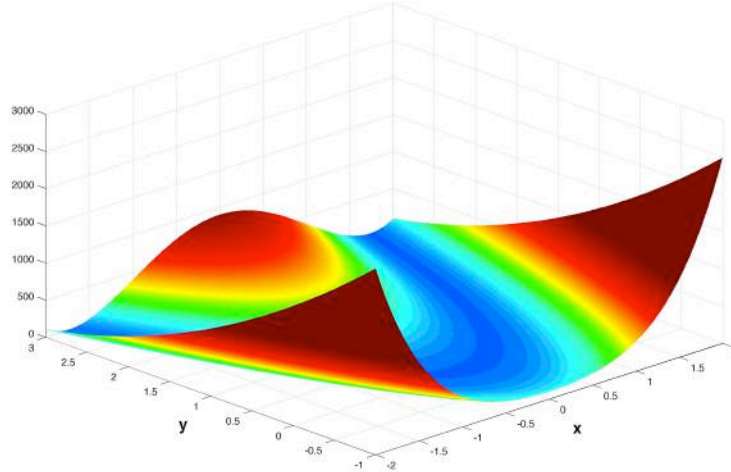
Figure 4.1：Rosenbrock function of two variables.

Figure 4.2 visualizes the Metropolis-Hastings algorithm running for Rosenbrock function. It can be seen that all the trials, which reduce the function values of the current state, are accepted. However, not all the trials that increase the function values are rejected.
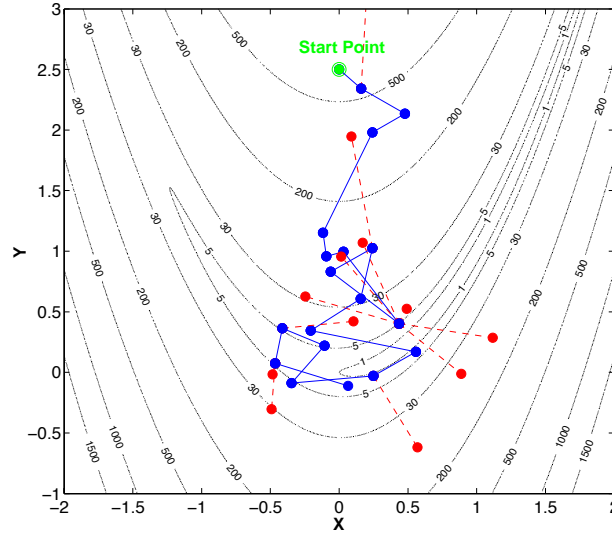
Figure 4.2: Evolution of the Markov chain running on the Rosenbrock function using Metropolis-Hastings algorithm. Total 30 iterations. The blue points connected by solid blue lines are the accepted samples, while the red points connected by dotted red lines are the rejected samples. The start point of the sampling, plotted as a solid green point, is at (0, 2.5). The contours of the Rosenbrock function are also plotted.

Figure 4.3 shows the generated samples after 60000 iterations. A large part of the samples is concentrated into the narrow valley, where the Rosenbrock function has relatively small values and thereby larger probability density values for the system. Even more dense samples locate around the point (1, 1), at which the Rosenbrock function has the global minimum.
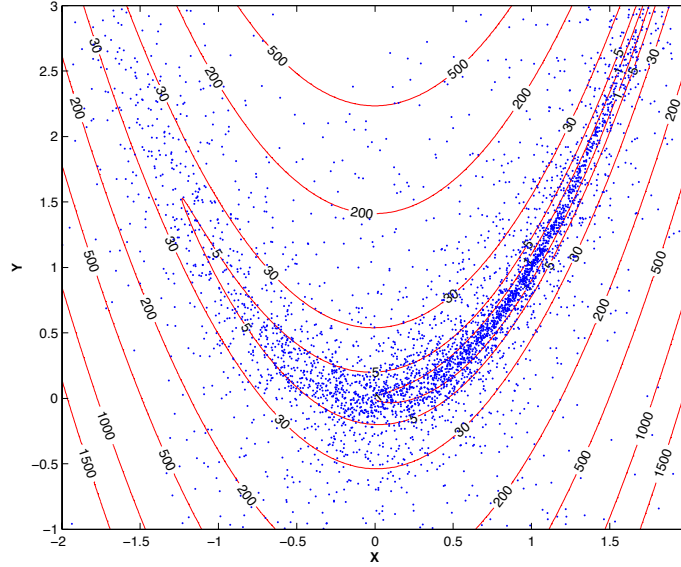
Figure 4.3: Random samples from Rosenbrock function using Metropolis-Hastings algorithm.

4.2 Simulated Annealing

Simulated Annealing (SA), which is the generalization of the Metropolis-Hastings algorithm, is used to find the global optimum of objective function which contains many local minima. In chemical industry, annealing is a process of slowly cooling a crystalline material from its melted status to form highly ordered, low-energy crystals. Kirkpatrick *et al.* (1983) first viewed the analogies between annealing process and optimization problem. In the numerical optimization problem, possible solutions of the numerical system are analogous to microcosmic configurations (or states) in the annealing process, and the cost function of the optimization problem is mapped to the internal energy E. The formation of flawless crystal is analogous to the attainment of global optimum, while the formation of metastable glass is the analogue of entrapment in local minima.

4.2.1 Gibbs-Boltzmann Distribution in Statistical Mechanics

The core of the SA method is to sample the Gibbs-Boltzmann distribution using the Metropolis-Hastings algorithm.

A fundamental result in statistical mechanics is that, for a system in thermal equilibrium at temperature T, the Gibbs-Boltzmann distribution:

$$P_B = \frac{\exp\left(-\dfrac{E(\omega)}{T}\right)}{Z(T)} \tag{4.13}$$

describes the expected fluctuations of the system's state. The 'state' of a system here means the configuration of its microscopic components. In above equation, ω denotes a

state of a statistical ensemble of a system, $E(\omega)$ is the energy of the configuration, and $Z(T)$ is called partition function:

$$Z(T) = \sum_{\omega} \exp\left(-\frac{E(\omega)}{T}\right) \qquad (4.14)$$

In the Boltzmann distribution in equation (4.13), the system assigns progressively larger probability to the low-energy states as T decrease. Finally the system will freeze to a configuration with global minimal energy. This global minimal energy state is called 'ground state'. When it is applied to an optimization problem, the energy can be identified with the misfit function in the inversion problem, and the ground state is the counterpart of the global optimal estimate.

Generally, it is impossible to get the explicit expression for the Gibbs-Boltzmann distribution in (4.13) due to the huge size of system's state space. Thereby, a sequence of samples generated by Metropolis-Hastings algorithm is used for approximation. This process is called 'importance sampling', which is the core of the SA technique.

4.2.2 Specific Procedure of Simulated Annealing

Model parameters in the optimization problem are mapped to the state space variables ω in the thermal equilibrium system, and a misfit function (typically the sum of squares of the differences between observation and model prediction) are mapped to the energy E in the system. Using the Metropolis-Hastings algorithm, the model parameters are randomly perturbed to generate a trial model in each step. The change in energy ΔE from the old state is computed. If $\Delta E \leq 0$, the trial is accepted and further used as the starting point for the next step; If $\Delta E > 0$, the trial model is only accepted with probability

$$P_{accept} = exp\left(-\frac{\Delta E}{T}\right). \qquad (4.15)$$

If it is not accepted, the old model parameters are used to start the next iteration. It is not hard to see that this transition probability is a specific form of equation (4.9) and satisfies the detailed balance condition.

By repeating this 'trial and decision' procedure many times, a sequence of random samples is obtained from the Gibbs-Boltzmann distribution in equation (4.13), which describes the states of a system in thermal equilibrium at temperature T.

The temperature T is simply a control parameter in the same unit as the misfit function. For a given T, a population of parameter configurations of the given optimization problem can be generated, and they are in the Boltzmann distribution as long as the number of samplings is large enough. The SA process begins at a high temperature, then slowly lowers the temperature until the system 'freezes' and no further changes occur. At each temperature stage, the iterations must proceed long enough for the system to reach a steady (equilibrium) state.

4.3 Numerical Examples

4.3.1 Subsurface Prism Detection

The Simulated Annealing is applied to detect a subsurface prism using synthetic gravitational gradient observation. As shown in Figure 4.4, a prism of different density from surrounding medium is buried underground, and its position, size, orientation and inclination can be fully described under a NED (north-east-down) Cartesian frame. x_0, y_0 and d give out the horizontal position and depth of one vetex of the prism; L, W and h describe the prism's length, width and height; s and δ denote orientation and inclination.

On the ground surface, the full tensor gravitational gradients (Γ^{calc}) generated by this subsurface prism anomaly can be calculated using the analytical formulas given by Jekeli (2003).
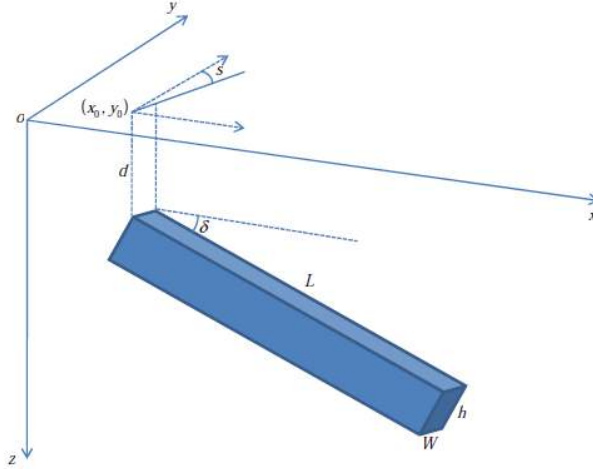
Figure 4.4: Position, size and orientation of a subsurface prism described using 8 parameters.

The optimization problem here is to find a set of model parameters which minimize the cost function:

$$\Phi(x_0, y_0, d, L, W, h, s, \delta) = \sum_{\omega \in \Omega} \left(\Gamma^{obs}(\omega) - \Gamma^{calc}(\omega) \right)^2 \tag{4.16}$$

where Γ^{obs} denotes the observed gravitational gradients on the ground surface, and Ω denotes the set of observation sites.

In the computation, a prism is set with $x_0 = 0\,\text{m}$, $y_0 = 0\,\text{m}$, $d = 5\,\text{m}$, $L = 100\,\text{m}$, $W = 1\text{m}$, $h = 2\,\text{m}$, $s = 30°$ and $\delta = 0°$. Assuming the prism has density contrast of 2.67g/cc with respect to surrounding homogeneous medium, the gravitational gradient were calculated over a 200m by 200m square region. Figure 2 shows the simulated T_{zz}

(the second derivative of gravitational potential with respect to the z-axis of the local NED frame in Figure 4.4) observation.
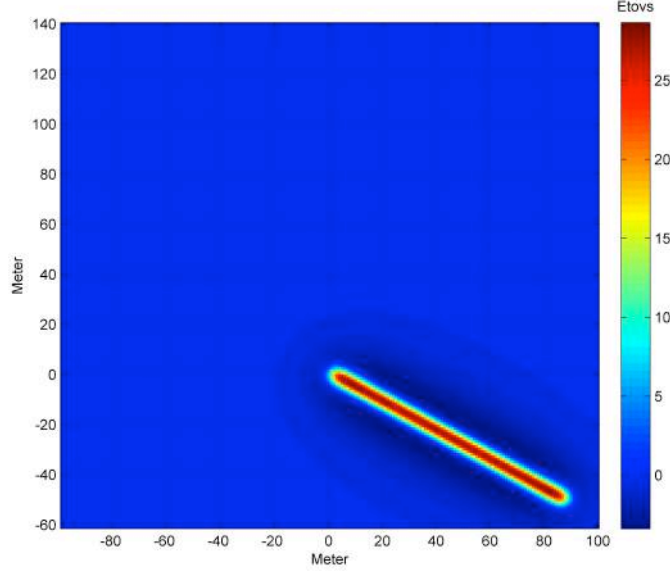
Figure 4.5: The simulated gravitational gradient anomaly (Tzz component) on the ground surface due to a prism with following configuration: $x_0 = 0\,\text{m}$, $y_0 = 0\,\text{m}$, $d = 5\,\text{m}$, $L = 100\,\text{m}$, $W = 1\,\text{m}$, $h = 2\,\text{m}$, $s = 30°$ and $\delta = 0°$.

Each possible combination of eight parameters represents as a point in an eight-dimensional state space. To start the search, initial values of parameters (i.e. initial state $\mathbf{x}_0$) should be given. In addition, the initial temperature T_0 should be assigned. In each iteration, only one of eight parameters is randomly perturbed, thereby, all eight parameters are perturbed sequentially in eight consecutive iterations, which is called a cycle counted by an integer variable N_c. As discussed before, whether or not the new trial state $\mathbf{x}_{i+1}$ is accepted depends on the value of corresponding objective function Φ_{i+1}. If Φ_{i+1} has the minimal value so far, it is stored as, $\Phi_{\min}$, an intermediate result for further comparison; and, the corresponding state $\mathbf{x}_{i+1}$ is accepted as the intermediate optimal point $\mathbf{x}_{optimal}$. Figure 4.6 gives the flow chart of the algorithm. N_T denotes the total cycles allowed in each temperature stage T_j, and should be large enough to allow the system to reach the thermal equilibrium. After N_T cycles, the temperature is reduced according to an 'annealing scheduling' of $T_{j+1} = 0.5T_j$ and a new sequence of moves is made starting from current $\mathbf{x}_{optimal}$, until the steady state is reached again, and so on. At higher temperature, gross features of the true configuration are sketched; Fine details are further revealed at lower temperatures. The process is stopped at a temperature low enough so that no more useful improvement can be expected.

In our test, 1000 cycles (8000 iterations) are executed at each temperature stage T_j to guarantee that the system would arrive at a steady/equilibrium state (the average value of Φ almost remains constant as i increases). The criterion of convergence is set to be $|\Phi_{i+1} - \Phi_{minimum}| < \varepsilon = 1 \times 10^{-20}$ in this test.

```
                    ⬡ Initialize parameters ⬡
                              │
                              ▼
    ┌─────────────────────────────────────────────────────┐
    │   Perform a cycle of random moves, N_c++;            │
    │   Accept or reject the trial;                        │
    │   Record the optimal point obtained so far: Θ_minimum &X_optimal │
    └─────────────────────────────────────────────────────┘
                              │
                              ▼
                        ◇ N_c ≥ N_T ? ◇ ──── No ──────►
                              │
                             Yes
                              ▼
              ┌──────────────────────────────┐
              │   Reduce temperature;        │
              │   Reset N_c=0;               │
              │   Set initial point as X_optimal │
              └──────────────────────────────┘
                              │
                              ▼
                    ◇ |Θ- Θ_min|< ε ◇ ──── No ──────►
                              │
                             Yes
                              ▼
                          ( End )
```
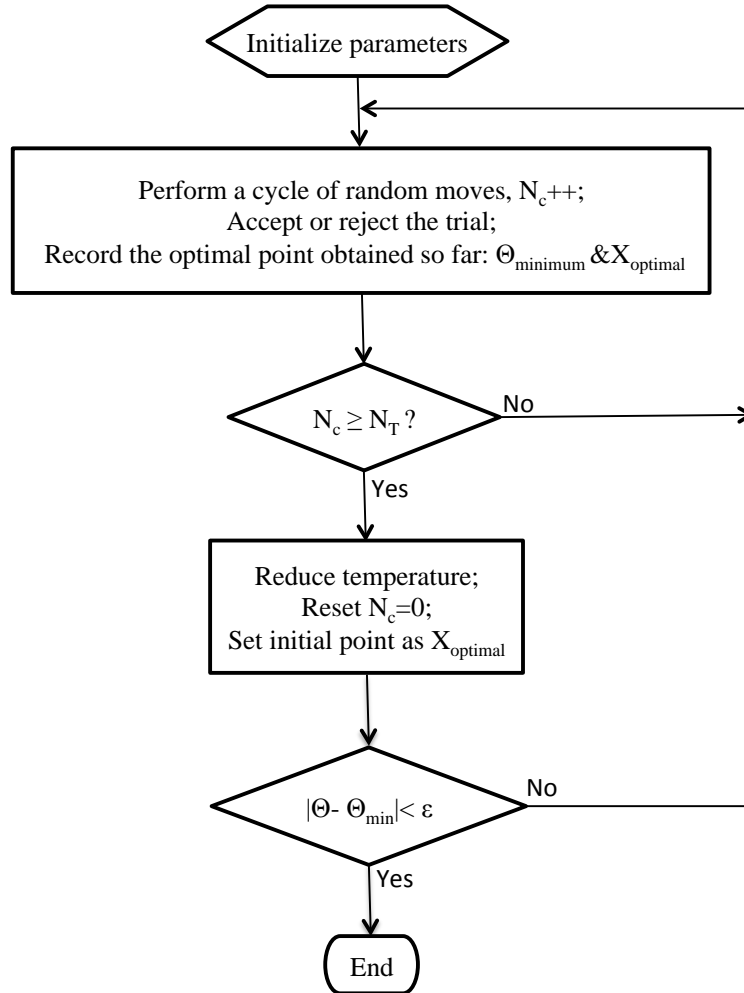
Figure 4.6: The flow chart of Simulated Annealing algorithm.

Figure 4.7 shows the histogram of accepted trials at four different temperatures. At a given temperature, the probability density function of the sytem at equilibrium state can be approximated by these random samples. These histograms also help to monitor the computation process as well as to validate the effect of lowering temperature. At relative high temperature, say $T = 50$, all samples equally distribute in the continuous state space. It is difficult to pick out a peak. As T decreases, the gross feature of the true state gradually shows up. For example, when T is lowered to 0.05,the samples for most

parameters (except inclination) locate in narrow ranges centered around their true values. The peaks in the histograms indicate the states which lead to even smaller cost functions; Finally at convergence, the algorithm gave a small subspace of the state space, where the global optimum resides.
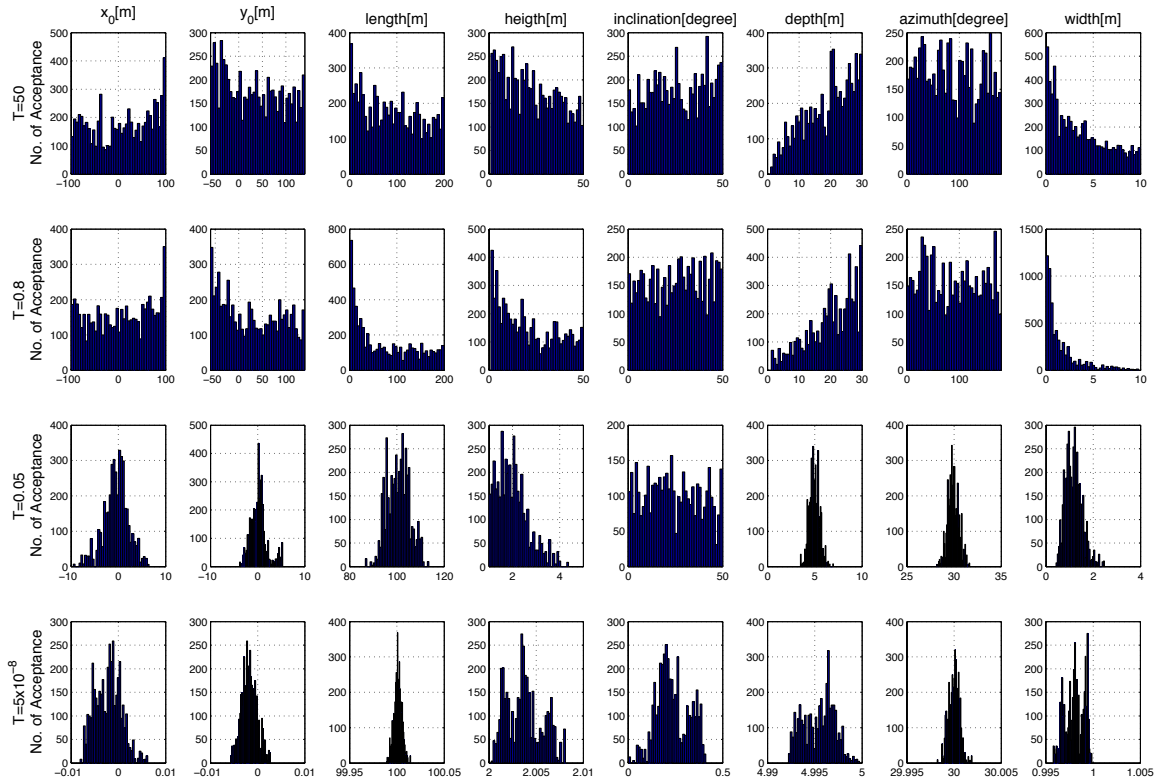
Figure 4.7: Histograms of the samples for prism parameters at different temperatures.

4.3.2 Fault Size and Slip Estimation

This example shows the feasibility of earthquake parameter estimation using observations from spaceborne gravimetry by the Simulated Annealing technique. A fictitious rectangular fault plane, whose length, width, strike and dip are 500km, 200km, 203° and 10° respectively, is buried at 1km depth east of Japan. The coseismic gravity change owing to a uniform thrust slip of 10m on the fault plane is computed at the surface of the earth under the assumption of a homogeneous elastic half-space. In order to make the spatial resolution of the synthetic observation commensurate with the resolution of spaceborne gravimetric observation, a 350km isotropic Gaussian filter is applied to the calculated coseismic gravity change. Figure 4.8 shows the coseimic gravity changes at

spatial resolution of ~350km half-wavelength, which mimic the observations by the GRACE satellites.
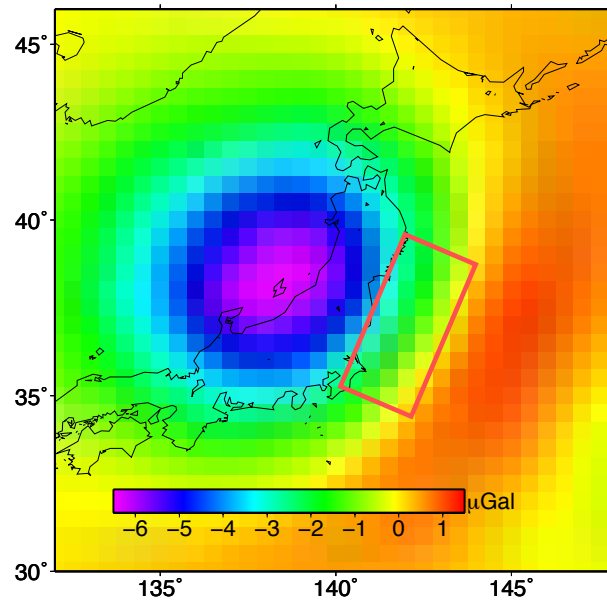
Figure 4.8: Coseismic gravity changes by a fictitious faulting with uniform thrust slip of 10m occurring on the megathrust interface at Japan trench. The fault plane, which is plotted as a red rectangular, has length of 500km, width of 200km, dip of 10° and strike of 203°.

In the inversion, the fault strike, dip and depth are assumed to be known. Only the fault size and the slip are estimated by the SA procedure. Figure 4.9 shows the histograms of samples at different temperatures. At very beginning of the iteration, the temperature T is set as high as 1000. As can be seen from Figure 4.9a~4.9c, all samples generated at this temperature are almost distributed uniformly in the state space; As the temperature decreases slowly, the distributions of samples gradually become narrowed; Finally, at the low temperature stage of T=0.04 (Figure 4.9j~l), the samples for all three parameters concentrate in a small space around their true value. The sample, which leads to the minimum misfit function, is chosen as the optimal estimate.
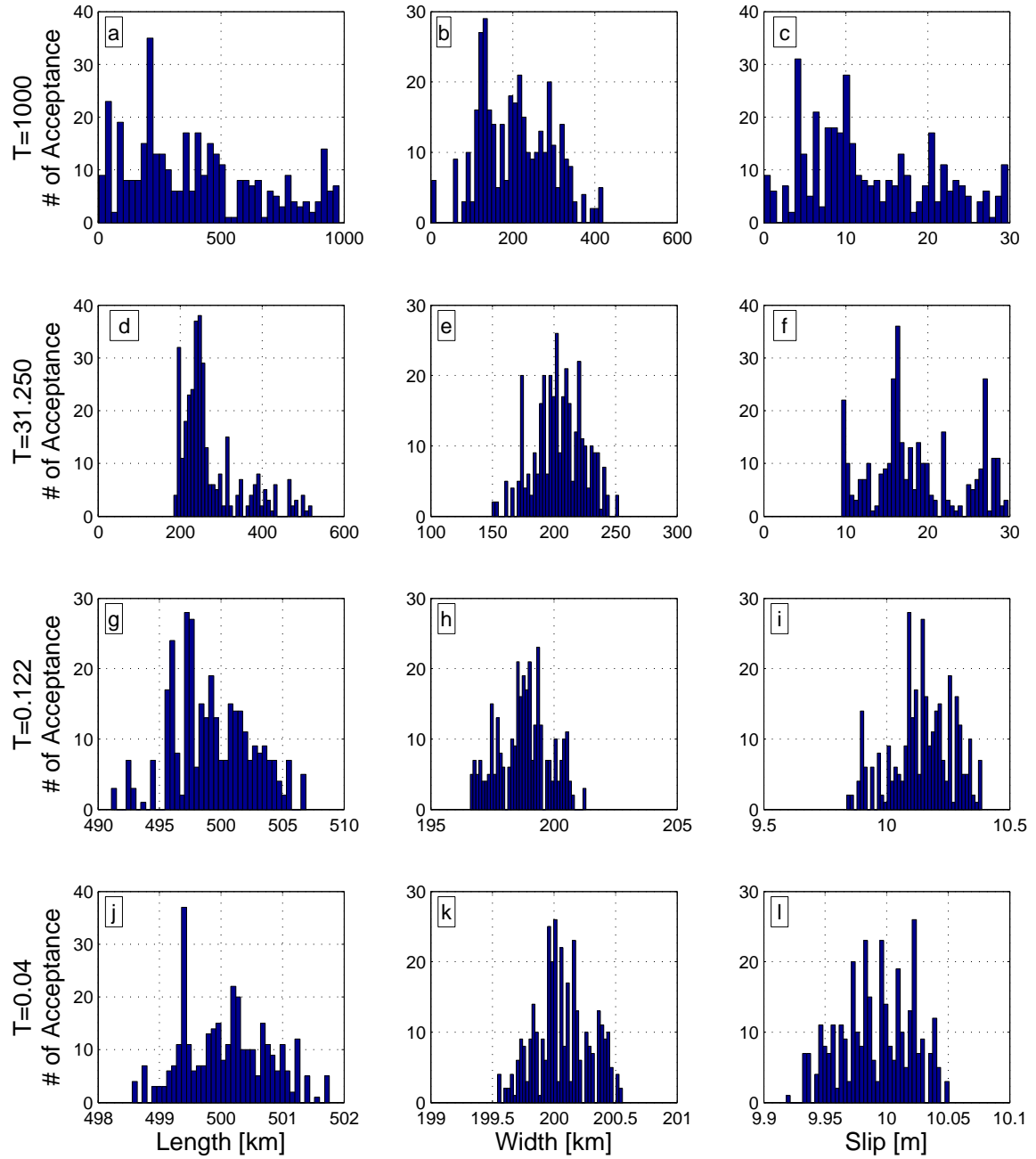
Figure 4.9 : Histograms of the samples of faulting parameters at different temperatures.

Chapter 5:   Application

In this chapter, the forward modeling, the spaceborne data processing scheme, and nonlinear inversion method developed in previous chapters are applied to study three recent great earthquakes: the 2004 Mw 9.1~9.2 Sumatra Andaman earthquake, the 2010 Mw 8.8 Maule, Chile earthquake, and the 2011 Mw 9.0 Tohoku-Oki earthquake, not only to describe the co/post-seismic gravitational signatures associated with them, but to quantitively constrain the faulting dimension and slip amplitude using spaceborne gravimetry observation.

5.1   Gravitational Gradient Changes Following the Sumatra-Andaman Earthquake Inferred from GRACE

5.1.1   Introduction

The 26 December 2004 Sumatra-Andaman Earthquake (Mw 9.1~9.3) is the largest event recorded in the last 50 years. This devastating shock was caused by the release of stress accumulated during the subduction of the oceanic plate (India plate) beneath the overriding continental plate (Burma plate). Due to the huge faulting area (~1000km long and ~200km wide), small dip angle (roughly 7°~15°), and large slips (more than 10m), the megathrust event ruptured 1200 to 1300km of a curved plate boundary (Lay *et al.,* 2005), and significantly deformed the crust and the mantle. On 28 March 2005, another thrust faulting event (Mw 8.6) occurred near Nias Island off the west coast of northern Sumatra. It ruptured an adjacent portion of the plate boundary by about 300km (Lay *et al.,* 2005).

After these great events, global seismogram data were collected to determine the fault geometry and rupture process (Ammon *et al.,* 2005; Lay *et al.,* 2005). In addition, surface displacement measurements observed by GPS on the surrounding nearby islands and on the continent were used in faulting inversion (Vigny *et al.,* 2005; Banerjee *et al.,* 2007; Chlieh *et al*., 2007). In addition to these methods, spaceborne gravimetry, though at much coarser spatial resolution, provided direct observation of mass redistribution caused by the earthquakes, thus leads to complementary constraints for the faulting mechanism studies. GRACE consists of two identical satellites that mutually track each other with a highly precise inter-satellite K-band microwave ranging (KBR) system. This system has the capability of monitor temporal changes in the Earth's gravitational field and can be used to estimate large scale mass redistributions within the Earth system. By applying the energy conservation principle to the satellites in their orbits and directly processing the KBR observations for regional gravitational field inversion, Han *et al.* (2006) demonstrated the detection of crust dilatation associated with the great Sumatra-Andaman

Earthquake. Ogawa & Heki (2007) processed the GRACE monthly gravitational field data sets to estimate postseismic changes. By using a tuned filter, Chen *et al.* (2007) showed that improved monthly gravity field data products from the University of Texas Center for Space Research (UTCSR) are able to reveal the coseismic change with greater spatial resolution. Other studies using GRACE to observe or constrain coseismic or postseismic deformation of these great earthquakes include: Panet *et al*. (2007), Han *et al*. (2008), and Cambiotti *et al.* (2011).

Due primarily to factors such as the GRACE along-track satellite-to-satellite tracking design which lacks observations in the radial and normal directions at a commensurate accuracy as the along-track KBR system, as well as errors in orbit, instrument, and background models, there are geographically correlated high-frequency errors in GRACE temporal gravity solutions. Post-processing of the GRACE monthly spherical harmonic (SH), or Stokes coefficient data products to infer temporal gravity signals thus requires the so-called "decorrelation" or "de-striping" techniques and spatial smoothing in order to suppress or minimize the high-frequency errors (Jekeli, 1981; Wahr *et al.,* 1998; Swenson & Wahr, 2006). Depending on the post-processing algorithms used, there could be a significant trade-off between the resulting attainable spatial resolution and the accuracy of the GRACE temporal gravitational field products. The typical resolution at present is about several hundreds km half-wavelength. However, geophysical signals associated to phenomena of regional scale, such as earthquakes, are characterized dominantly by high-frequency contents. The relatively coarse spatial resolution therefore limits the application of GRACE observation to earthquake studies.

Here, we infer the full gravitational gradient tensor from the GRACE Stokes coefficients by taking the second derivatives of the gravitational potential in a given orthogonal coordinate system, and apply these quantities to the study of the coseismic deformation resulting from the combined Sumatra-Andaman and the Nias undersea earthquake events. Although we do not obtain additional high-frequency content via the gravitational gradients, we actually amplify short-wavelength components in the observation, so that the spectral structures of observation and the signal source are more consistent. With the emphasis on the high-frequency components resulting from the second derivatives of the potential, the corresponding coseismic gravitational gradient changes delineate more clearly the rupture line, and reveal refined mass redistribution features caused by the earthquakes. In addition, some of the gradient components, which are not contaminated by GRACE high-frequency (striping) error, are used to refine the edges of the mass anomaly.

5.1.2   GRACE Data Processing

We use the CSR Release (RL) 04 GRACE Level 2 (L2) monthly gravity field data products, which are composed of fully normalized SH coefficients up to degree and order 60. A total of 47 monthly gravity field solutions covering the time period from January 2003 to March 2007 are used. The earthquakes in question disturbed the mass distribution in the crust and mantle (Han *et al.,* 2006), and therefore the Earth's gravitational field. In order to extract the coseismic signals and suppress the seasonal variations, we take the

difference of two 2-year mean gravitational fields before and after the two combined earthquakes (Sumatra-Andaman and Nias events). The mean gravity field before the earthquake is obtained by averaging 23 monthly solutions from January 2003 to December 2004 (there is no solution available for June 2003); and, the mean field after the 2005 Nias event is computed by taking the mean of 24 monthly solutions from April 2005 to March 2007. so that this mean field contains signals caused by both 26 December 2004 Sumatra earthquake and the 28 March 2005 Nias earthquake. The coefficient differences ΔC_{nm}, ΔS_{nm} between these two mean fields are then used to compute coseismic gravitational gradient changes due to the Sumatra-Andaman and the Nias earthquakes.

The gravitational field difference before and after the earthquake can be computed by:

$$\Delta V = \frac{GM}{r}\left(\sum_{n=2}^{\infty}\sum_{m=0}^{n}\left(\frac{a_e}{r}\right)^n\left(\Delta C_{nm}\cos m\lambda + \Delta S_{nm}\sin m\lambda\right)P_{nm}\left(\cos\theta\right)\right) \qquad (5.1)$$

a_e is the equatorial radius; r,θ,λ are the radius, colatitude, and longitude respectively; P_{nm} are the associated Legendre function; GM is the gravitational constant multiplied by the mass of the earth. Based on equation (5.1), the first derivatives of ΔV with respect to r,θ and λ can be easily derived as:

$$\Delta V_r = -\frac{GM}{R^2}\left(\sum_{n=2}^{\infty}(n+1)\left(\frac{R}{r}\right)^{n+2}\sum_{m=0}^{n}\left(\Delta C_{nm}\cos m\lambda + \Delta S_{nm}\sin m\lambda\right)P_{nm}\left(\cos\theta\right)\right) \qquad (5.2)$$

$$\Delta V_\theta = -\frac{GM}{R}\left(\sum_{n=2}^{\infty}\left(\frac{R}{r}\right)^{n+1}\sum_{m=0}^{n}\left(\Delta C_{nm}\cos m\lambda + \Delta S_{nm}\sin m\lambda\right)P'_{nm}\left(\cos\theta\right)\sin\theta\right) \qquad (5.3)$$

$$\Delta V_\lambda = \frac{GM}{R}\left(\sum_{n=2}^{\infty}\left(\frac{R}{r}\right)^{n+1}\sum_{m=0}^{n}m\left(-\Delta C_{nm}\sin m\lambda + \Delta S_{nm}\cos m\lambda\right)P_{nm}\left(\cos\theta\right)\right) \qquad (5.4)$$

and the second derivatives of ΔV with respect to r,θ and λ are:

$$\Delta V_{rr}(r,\theta,\lambda) = \frac{GM}{R^3}\left(\sum_{n=2}^{\infty}(n+1)(n+2)\left(\frac{R}{r}\right)^{n+3}\sum_{m=0}^{n}\left(\Delta C_{nm}\cos m\lambda + \Delta S_{nm}\sin m\lambda\right)P_{nm}\left(\cos\theta\right)\right) \qquad (5.5)$$

$$\Delta V_{r\theta}(r,\theta,\lambda) = \frac{GM}{R^2}\left(\sum_{n=2}^{\infty}(n+1)\left(\frac{R}{r}\right)^{n+2}\sum_{m=0}^{n}\left(\Delta C_{nm}\cos m\lambda + \Delta S_{nm}\sin m\lambda\right)P'_{nm}\left(\cos\theta\right)\sin\theta\right) \qquad (5.6)$$

$$\Delta V_{r\lambda}(r,\theta,\lambda) = \frac{GM}{R^2}\left(\sum_{n=2}^{\infty}(n+1)\left(\frac{R}{r}\right)^{n+2}\sum_{m=0}^{n}m\left(\Delta C_{nm}\sin m\lambda - \Delta S_{nm}\cos m\lambda\right)P_{nm}\left(\cos\theta\right)\right) \qquad (5.7)$$

$$\Delta V_{\theta\theta}(r,\theta,\lambda) = \frac{GM}{R}\left(\sum_{n=2}^{\infty}\left(\frac{R}{r}\right)^{n+1}\sum_{m=0}^{n}\left(\Delta C_{nm}\cos m\lambda + \Delta S_{nm}\sin m\lambda\right)\left(P''_{nm}\left(\cos\theta\right)\sin^2\theta - P'_{nm}\left(\cos\theta\right)\cos\theta\right)\right) \qquad (5.8)$$

$$\Delta V_{\theta\lambda}(r,\theta,\lambda) = \frac{GM}{R}\left(\sum_{n=2}^{\infty}\left(\frac{R}{r}\right)^{n+1}\sum_{m=0}^{n}m\left(\Delta C_{nm}\sin m\lambda - \Delta S_{nm}\cos m\lambda\right)P'_{nm}\left(\cos\theta\right)\sin\theta\right) \qquad (5.9)$$

$$\Delta V_{\lambda\lambda}(r,\theta,\lambda) = -\frac{GM}{R}\left(\sum_{n=2}^{\infty}\left(\frac{R}{r}\right)^{n+1}\sum_{m=0}^{n}m^2\left(\Delta C_{nm}\cos m\lambda + \Delta S_{nm}\sin m\lambda\right)P_{nm}\left(\cos\theta\right)\right) \qquad (5.10)$$

Based on equation (5.1)~(5.10), the coseismic changes are first computed in spherical coordinates. Since the local gradient changes are of interest here, the local North-East-Down (NED) frame at a point with spherical coordinates (r,θ,λ) is introduced: the x-axis is directed to the north, the y-axis to the east, and the z-axis downwards. According to the transformation principle of curvilinear coordinates, the full gravitational gradient tensor (second derivatives of the potential difference between two mean fields) in this local NED frame can be obtained using following equations:

$$\Delta V_{xx}(r,\theta,\lambda) = \frac{1}{r}\Delta V_r(r,\theta,\lambda) + \frac{1}{r^2}\Delta V_{\theta\theta}(r,\theta,\lambda) \qquad (5.11)$$

$$\Delta V_{xy}(r,\theta,\lambda) = \Delta V_{yx}(r,\theta,\lambda) = \frac{1}{r^2\sin\theta}\left(-\cot\theta\Delta V_{\lambda}(r,\theta,\lambda) + \Delta V_{\theta\lambda}(r,\theta,\lambda)\right) \qquad (5.12)$$

$$\Delta V_{xz}(r,\theta,\lambda) = \Delta V_{zx}(r,\theta,\lambda) = \frac{1}{r}\Delta V_{r\theta}(r,\theta,\lambda) - \frac{1}{r^2}\Delta V_{\theta}(r,\theta,\lambda) \qquad (5.13)$$

$$\Delta V_{yy}(r,\theta,\lambda) = \frac{1}{r}\Delta V_r(r,\theta,\lambda) + \frac{1}{r^2}\cot\theta\Delta V_{\theta}(r,\theta,\lambda) + \frac{1}{r^2\sin^2\theta}\Delta V_{\lambda\lambda}(r,\theta,\lambda) \qquad (5.14)$$

$$\Delta V_{yz}(r,\theta,\lambda) = \Delta V_{zy}(r,\theta,\lambda) = \frac{1}{r\sin\theta}\left(\Delta V_{r\lambda}(r,\theta,\lambda) - \frac{1}{r}\Delta V_{\lambda}(r,\theta,\lambda)\right) \qquad (5.15)$$

$$\Delta V_{zz}(r,\theta,\lambda) = \Delta V_{rr}(r,\theta,\lambda) \qquad (5.16)$$

Because of the large errors in the geographically-correlated and high-frequency components of GRACE data, decorrelation and filtering techniques are usually applied in order to obtain reasonable estimates of the time-varying signals. However, we did not apply any decorrelation to the GRACE SH solutions with the intent of preserving as much spatial resolution as possible. But, we did use an isotropic Gaussian filter with radius of 350km to take into account the large errors at high degrees and orders (Jekeli, 1981; Wahr *et al.,* 1998). The changes were then extracted by differencing the filtered mean gravitational gradient tensors before and after the earthquakes. The observation is a combination of coseismic signals associated to the 2004 Sumatra event and 2005 Nias event, as well as the viscoelastic relaxation of the asthenosphere (Pollitz *et al.,* 2006; Panet *et al.,* 2007; Han *et al.,* 2008;). However, we confine our discussions only to the coseismic signals which dominate the observation.

5.1.3 Model Predicted Coseismic Gravity Gradient Change

The finite fault model for the Sumatra-Andaman (24 December 2004) and the Nias (28 March 2005) earthquakes (courtesy of *C. Ji*, UCSB) are used to predict the coseismic gravitational gradient changes. The model consists of 7 sub-fault planes and

over 1000 slip vectors, which were determined from both seismic records and far-field GPS observations. For convenience, the 7 sub-faults were merged into 4 segments and named Andaman, Nicobar, Sumatra and Nias, respectively. The first three constitute the fault model for the 2004 Sumatra event, and the Nias segment refers to the 2005 Nias event. Figure 5.1 shows the fault planes and the slip distribution.
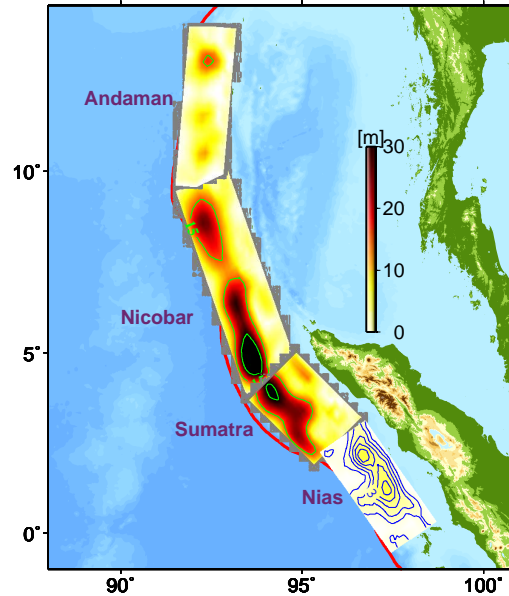
Figure 5.1: Finite fault model and slip distribution for 2004 Sumatra-Andaman and 2005 Nias earthquakes (courtesy of *C. Ji* at UCSB). On Audaman, Nicobar and Sumatra segments, the contours at interval of 15m are plotted in green. On Nias segment, contours at interval of 1m are plotted in blue.

In order to properly model the coseismic gravitational gradient changes, the total mass redistribution due to earthquakes was divided into the following two components: the vertical displacement (uplift and subsidence) at the sea floor and Moho, where significant density contrasts exist; and the density changes (both in crust and mantle) due to the internal deformation assuming an elastic Earth. The Fourier approach introduced in section 2.2 was used to model the gravitation and gravitational gradient changes caused by the above two factors.

59

Figure 5.2 shows the gravitational gradient changes due to topography change at the sea floor (Figure 5.2a~5.2f), the Moho (Figure 5.2g~5.2l), and the summation of them (Figure 5.2m~5.2r). In order to compare with GRACE-derived values, the 350km isotropic Gaussian filter was applied.
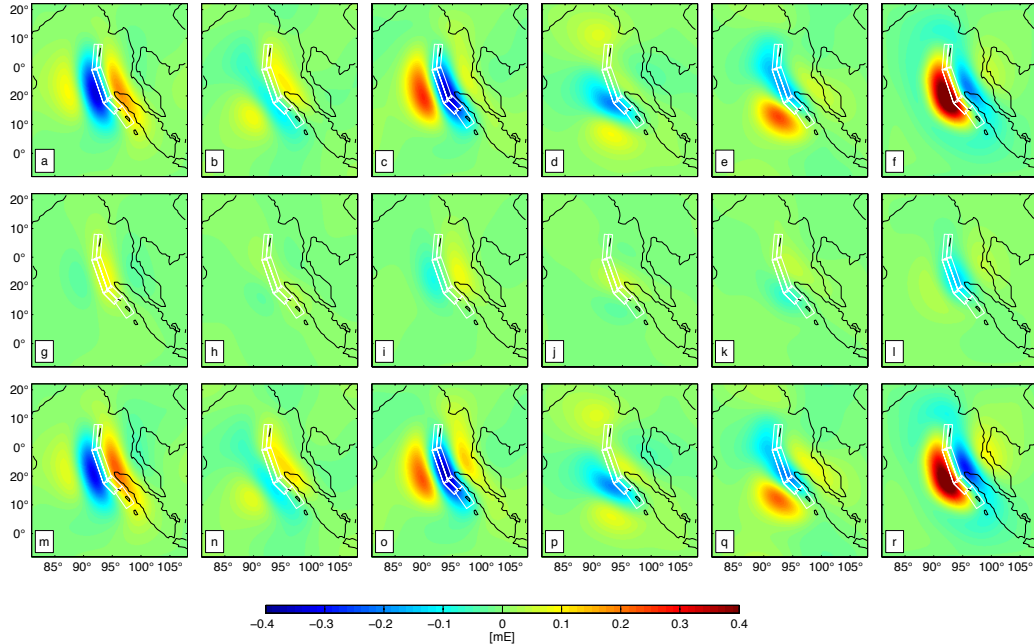
Figure 5.2: Seismic model predicted coseismic gravitational gradient changes [in unit of milli-Eötvös] due to uplift/subsidence at sea floor (a~f corresponds to $\Delta V_{xx}, \Delta V_{xy}, \Delta V_{xz}, \Delta V_{yy}, \Delta V_{yz}$ and ΔV_{zz}, respectively), Moho (g~l corresponds to $\Delta V_{xx}, \Delta V_{xy}, \Delta V_{xz}, \Delta V_{yy}, \Delta V_{yz}$ and ΔV_{zz}, respectively) and the total effect by summing them together (m~r corresponds to $\Delta V_{xx}, \Delta V_{xy}, \Delta V_{xz}, \Delta V_{yy}, \Delta V_{yz}$ and ΔV_{zz}, respectively). A 350km isotropic Gaussian filter was applied.

Figure 5.3 shows the gradient changes due to density change in the crust (Figure 5.3a~5.3f), the mantle (Figure 5.3g~5.3l) and their summation (Fig 5.3m~5.3r).
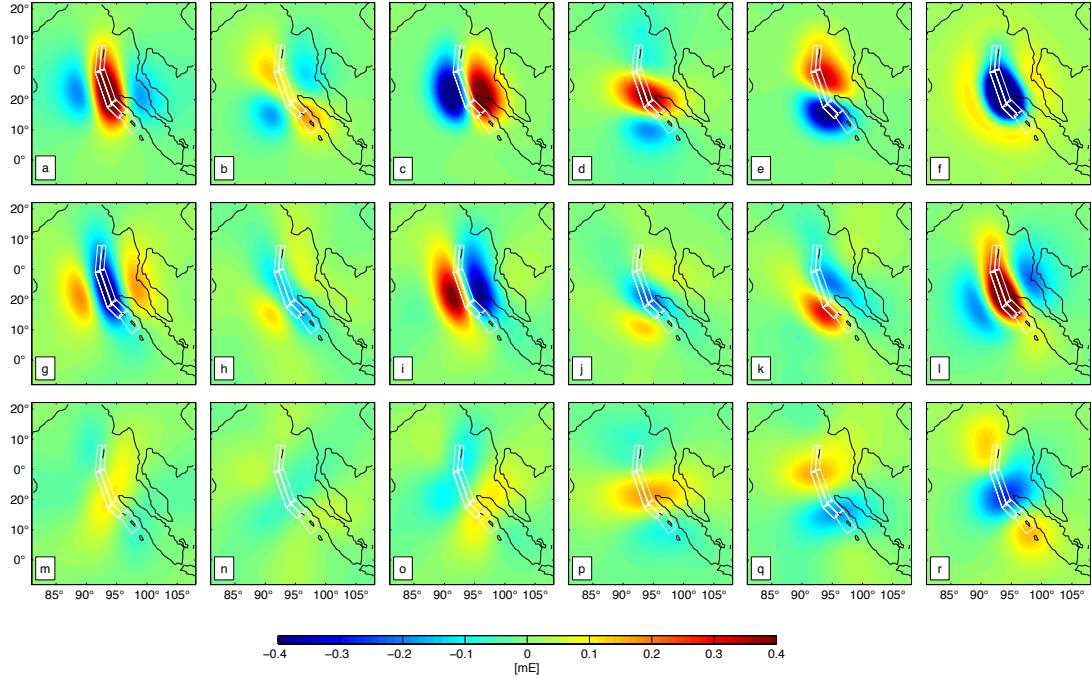
Figure 5.3: Seismic model predicted coseismic gravitational gradient changes (milli-Eötvös) due to density change in crust (a~f corresponds to ΔV_{xx}, ΔV_{xy}, ΔV_{xz}, ΔV_{yy}, ΔV_{yz} and ΔV_{zz}, respectively), mantle (g~l corresponds to ΔV_{xx}, ΔV_{xy}, ΔV_{xz}, ΔV_{yy}, ΔV_{yz} and ΔV_{zz}, respectively) and the total effect by summing them together (m~r corresponds to ΔV_{xx}, ΔV_{xy}, ΔV_{xz}, ΔV_{yy}, ΔV_{yz} and ΔV_{zz}, respectively). A 350km isotropic Gaussian filter was applied.

By adding the contributions from the vertical motion and the density changes, we obtained the total gravitational gradient changes, which are shown in Figure 5.4a~5.4f. Figure 5.4g~5.4l shows the GRACE-derived coseismic gravitational gradient changes, which were computed following the procedures described in Section 5.1.2.
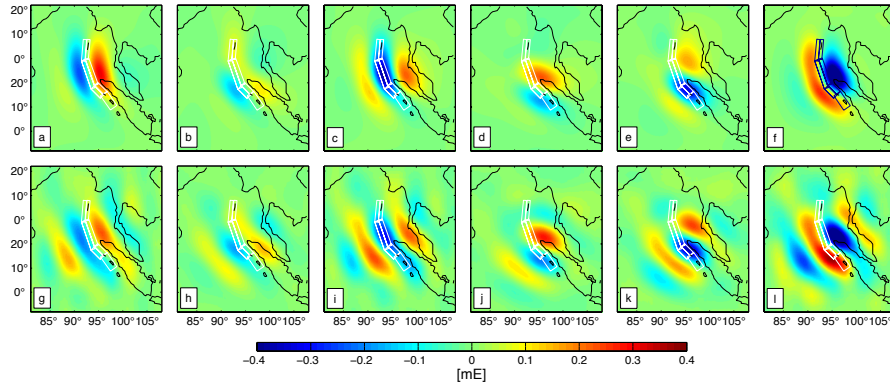
Figure 5.4: a~f: Seismic model predicted total coseismic gravitational gradient changes [in unit of milli-Eötvös] for components of ΔV_{xx}, ΔV_{xy}, ΔV_{xz}, ΔV_{yy}, ΔV_{yz} and ΔV_{zz} respectively, i.e., the sum of contributions from vertical displacements on the sea floor/Moho (m~r in Figure 5.2) and from density changes (m~r in Figure 5.3). g~l: GRACE-derived gravitational gradient changes.

For comparison with GRACE observed gravity changes, we also computed the gravity changes following the 2004 Sumatra and 2005 Nias earthquakes (Figure 5.5a) using the same GRACE data as the gravitational gradients were calculated.
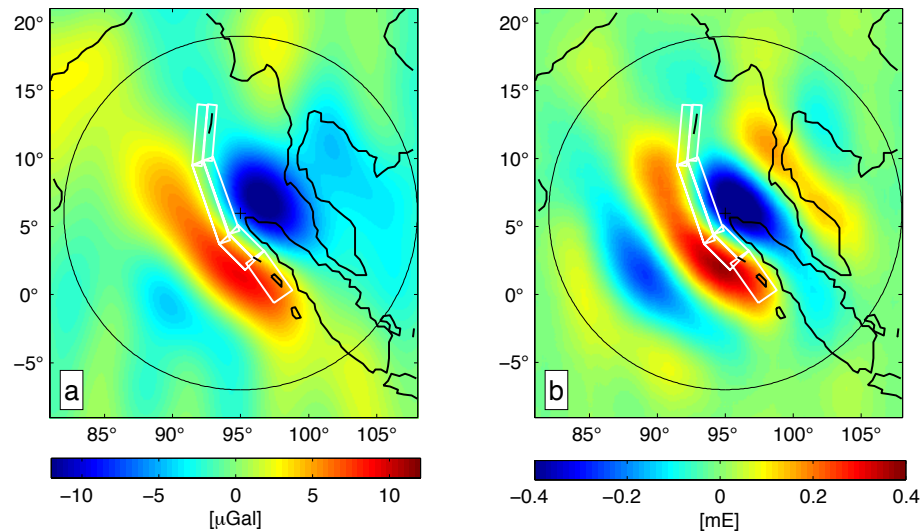
Figure 5.5: Comparison between GRACE-derived (**a**) gravity changes and (**b**) gravitational gradient change (component of ΔV_{zz}) caused by 2004 Sumatra event and 2005 Nias event.

5.1.4 Discussions

Large deformations caused by earthquakes are typically highly local, and large parts of the signal associated to the deformation reside in the high frequency band. Unfortunately, GRACE is only capable to provide reliable estimate at the low-to-medium frequency band for the gravitational changes. Therefore, the applications of spaceborne gravimetry to earthquake studies are seriously limited by its current spatial resolution. To show the spectrum structures of the earthquake deformation itself, as well as of the GRACE observed gravitational and gradient changes (ΔV_{zz} component), we applied localized spectrum estimation using Slepian tapers. The Slepian functions are a set of bandlimited functions that have their energy optimally concentrated inside a spherical cap (Simons *et al.,* 2006). It has been proven that it is an effective method to calculate the localized power spectrum using Slepian tapers (Wieczorek & Simons, 2005). Figure 5.6 shows the spectrum of the geometrical deformation (uplift/subsidence of seafloor) and the physical observation, i.e. gravitational changes and their gradient (ΔV_{zz} component).

Although other geodetic techniques, such as GPS and InSAR, directly measure the deformation of the accessible surface, physical quantities, such as gravitational gradients, indicate the total surface and subsurface mass deformation. Thus, for example, they can be used to estimate the deformation associated with the uplift/subsidence of the sea floor, which may have a larger effect on disturbing the surrounding gravitational field than the visible (accessible) land areas. On the other hand, in the frequency domain, we expect both the geometric and the gravitational deformations to occupy the same spectral band, specifically the relatively high-frequency part, so that the gravitational observation can be used to more directly describe the geometric deformation. The vertical deformations at seafloor, as can be directly measured by GPS if there were no ocean water, are first predicted at full resolution of 50km. Then, it is expanded using spherical harmonics up to degree of 60. Although there is a large part of signals resides beyond degree of 60, we only discuss the spectral structures of signals truncated to degree 60, which is the maximum spherical harmonic degree detectable by the GRACE satellites. As shown in Figure 5.6, the band-limited vertical deformation (maximum degree of 60) signal predicted by model has more than 70% of its energy residing in SH degrees higher than 35. However, the gravitational change predicted by the model at spatial resolution of ~350km, which approximately mimics GRACE observations, only has ~40% of its energy in the same frequency band. The value is ~31% for the actual observed gravitational changes as shown in Figure 5.5a. For model-predicted and actual observed ΔV_{zz} changes, the energy for SH degrees larger than 35 take 67% and 71% of the total energy, respectively, and therefore are more consistent with the spectrum structure of the geometric deformation. Figure 5.5 compares earthquake-induced gravitational changes (Figure 5.5a) with the gravitational gradient changes (Figure 5.5b) detected by GRACE in space domain. By amplifying the high-frequency content, GRACE-derived ΔV_{zz} changes, together with other gravitational gradient components, help to reveal more detail in the deformations induced by an earthquake.
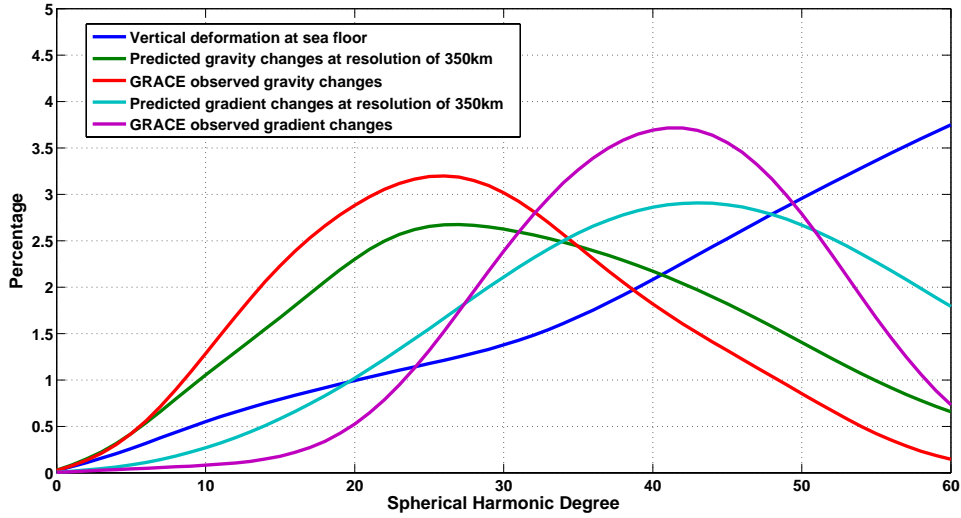
Figure 5.6: Spectrum structures of the earthquake deformation and the related gravity/gravitational gradients changes. The percentage of the total signal energy (truncated at SH degree 60) is plotted as a function of SH degree.

Considering the fact that the gradients often present complex patterns even for subsurface anomalies with simple geometries, their interpretation is not as straightforward as using the gravity anomaly data. The horizontal derivatives along the x and y directions act as a phase shifter, which shifts the locations of mass anomalies in corresponding directions. In addition, they enhance the high frequency components via the multiplication in the frequency domain with factors k_x and k_y. The vertical derivative along the z direction, on the other hand, emphasizes the high frequency components of the subsurface mass anomaly without changing its location. In the following, we will interpret the implications of observed gravitational gradients components.

Figure 5.4l shows the computed ΔV_{zz} using GRACE provided SH coefficients. The zero contour clearly delineates the shape of fault line, and helps to locate the hinge line corresponding to zero displacement. Along the fault line, two clearly separated patches of intensive positive anomalies are found: one located just west of the Sumatra segment, and the other one by the northwest corner of the Nicobar segment. The locations of these significant positive anomalies are consistent with the positions of discrete asperities on which coseismic slips are concentrated (Figure 5.1).

In the model-predicted value of ΔV_{zz} due to vertical displacement, there exist significant positive anomalies (Figure 5.2f) and negative anomalies (Figure 5.2l), which indicate uplift of the sea floor and a deepening of the Moho, respectively. The minimum value in the model-predicted total coseismic value of ΔV_{zz} due to vertical displacement (Figure 5.2r) is around –0.5 milli-Eötvös (mE), while the GRACE-derived minimal value of ΔV_{zz} (Figure 5.4l) is about –0.8 mE. The ~0.3mE discrepancy can be explained by the

64

effects of internal density change, primarily due to crust dilatation. Indeed, the model prediction shows the signatures of crust expansion (negative anomalies in Figure 5.3f) and mantle contraction (positive anomalies in Figure 5.3l). By summing these two parts, we obtain the total dilatation-induced value of ΔV_{zz}. The negative gravity gradient anomalies (due to crust expansion) reside over the middle of fault line, while positive signals (mantle contraction) occur at the two ends (Figure 5.3r). The ΔV_{zz} value due to crust dilatation is –0.34 mE, which explains the discrepancy between GRACE-derived total gravitational gradient changes and the contribution only from the modeled vertical displacement.

The gravitational gradient changes, ΔV_{xz} and ΔV_{yz}, were computed by taking x and y derivatives of ΔV_z, respectively. Since the horizontal derivative operator shifts the phase of the original anomaly distribution, the peaks (or troughs) in the results no longer indicate the maximum positive (or negative) mass anomaly. Instead, these peaks and troughs indicate the edges of the anomaly source, which can be better recognized since the peaks and troughs are sharpened due to the enhancement of the high frequency components. Furthermore, the GRACE-derived values of ΔV_{yz} (Figure 5.4k) are free from the geographically correlated errors in the GRACE monthly SH solutions, which manifest themselves as north-south stripes. Two peaks and two troughs can be found around the rupturing region in Figure 5.4k. They help to locate the southern and northern edges of the large mass anomaly as a result of the large slip in on south of Nicobar fault and north of Sumatra fault (Figure 5.1). Similarly, a symmetrical positive-negative-positive pattern with the fault line at the center can be found in both the GRACE-detected ΔV_{xz} (Figure 5.4i) and the corresponding model prediction (Figure 5.4c). This observed triplet around the faulting area should be close to the eastern and western edges of region with significant deformation induced by the earthquakes.

Similar to the computed ΔV_{xz} and ΔV_{yz} components, the changes, $\Delta V_{xx}, \Delta V_{yy}$, also give the locations of the edges. Figure 5.4j shows the GRACE-derived ΔV_{yy} component, which is also free from GRACE correlated errors. The zero contours between peak and trough indicate the southern and northern edges of mass anomaly. Similarly, the zero contours in the value of ΔV_{xx} components still follow the east-west edges.

5.2   Coseismic Slip of the 2010 Mw 8.8 Great Maule, Chile, Earthquake Quantified by GRACE Observation

5.2.1   Introduction
The 2010 Maule Chilean earthquake, which was caused by the subduction of the Nazca plate underneath the overlying South America plate, is the sixth largest event in the seismic record. Figure 5.7 shows the tectonic setting of the Andean subduction zone, and prior significant earthquakes around the Constitución gap (Beck *et al.,* 1998; Campos *et al.,* 2002; Moreno *et al.,* 2008; Nishenko, 1985; Ruegg *et al.,* 2002, 2009) since the

1835 Mw ~8.5 event (Darwin, 1845). The 1906 Mw 8.4, 1943 Mw 7.9 and 1985 Mw 7.8 earthquakes reduced the accumulated stresses in the segments north of the Constitución gap. The slip distribution of the 1960 Mw 9.5 event, the largest earthquake on record, extended north beneath the Arauco peninsula, accompanying stress release south of the gap. The middle locked zone (Constitución gap) had accumulated stresses for 175 years since 1835 until the 2010 Maule event, during which the rupture front propagated mostly upward (trench-ward) and bilaterally (northward and southward) rupturing a 500km long segment of the megathrust.
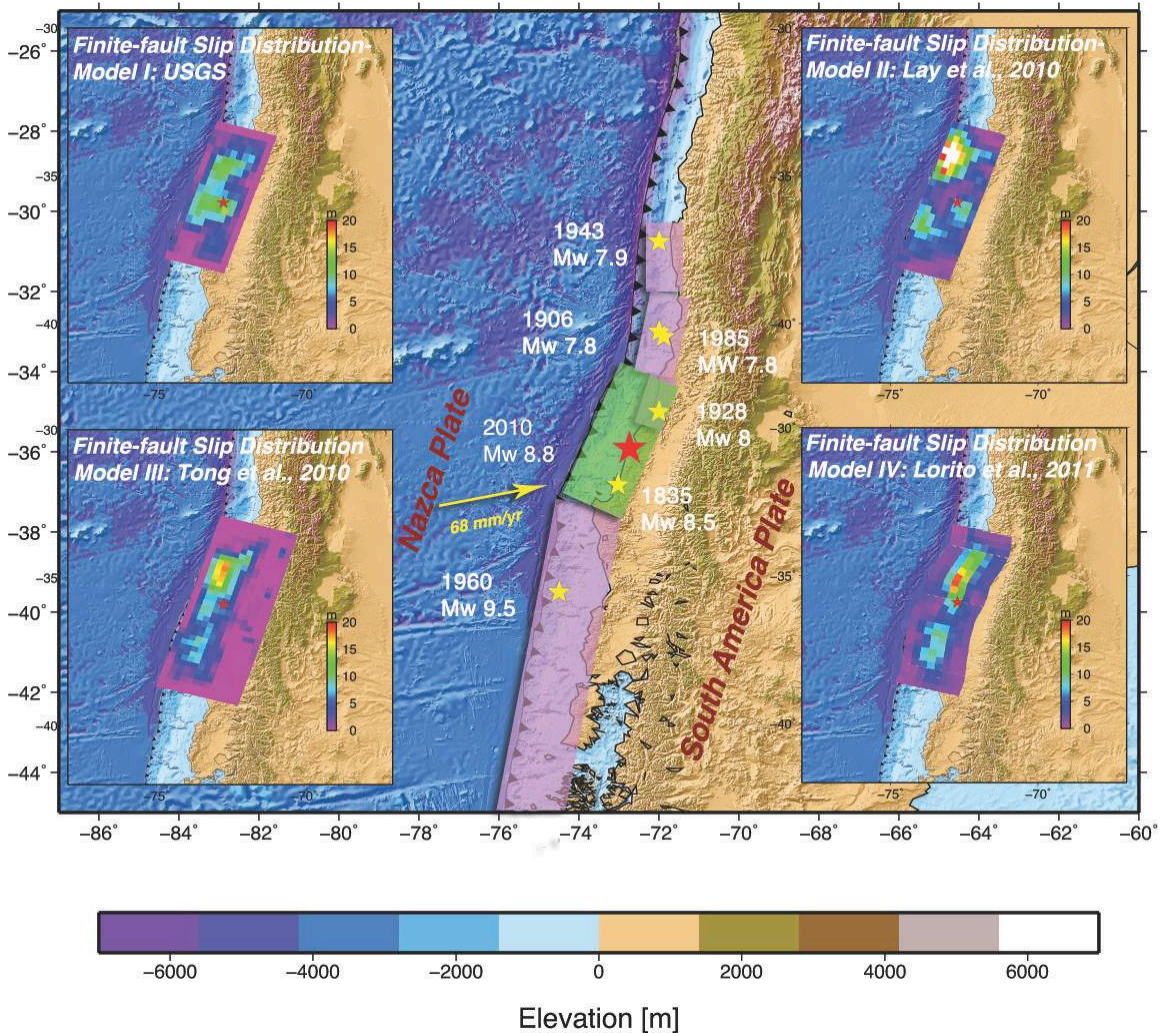

Figure 5.7: Tectonic setting of the region surrounding the 2010 Mw 8.8 Maule earthquake, with the epicenter denoted by a red star. The approximate rupture extents of previous large earthquakes (yellow stars indicate the approximate epicenters) are shown shaded in pink. The green shaded region is the Constitución seismic gap. The subplots

show the slip models by USGS (2010), Lay *et al.* (2010), Tong *et al.* (2010) and Lorito *et al.* (2011).

Data from teleseismic networks, coastal/river markers, tsunami sensors, Global Positioning System (GPS), and Interferometric Synthetic Aperture Radar (InSAR), have been used to observe and model the coseismic signature and slip history of this devastating event (Delouis *et al.,* 2010; Farías *et al.,* 2010; Lay *et al.,* 2010; Lorito *et al.,* 2011; Moreno *et al.,* 2010; Tong *et al.,* 2010; Vigny *et al.,* 2011). In addition, spaceborne gravimetry data from the Gravity Recovery And Climate Experiment (GRACE) satellites have been used to observe coseismic signature of the 2010 Maule earthquake (Heki & Matsuo, 2010; Han *et al.,* 2010).

The Mw 8.8 Maule earthquake permanently changed the mass distribution within the Earth and consequently its gravitational potential, which can be observed with temporal and spatial resolutions of a month and several hundred km, respectively, using data from the Gravity Recovery And Climate Experiment (GRACE) satellite mission (Tapley *et al.,* 2004). Previous analyses detected the coseismic signature of the Maule earthquake using GRACE, with different spatial resolutions, either based on global spherical harmonic analysis with additional filtering and decorrelation to remove high-frequency errors (Heki & Matsuo, 2010) or regional inversion directly using GRACE inter-satellite tracking data as geopotential disturbance observables with 500km spatial resolution (Han *et al.,* 2010). Our approach uses spatio-spectral localization with Slepian basis functions (Simons *et al.,* 2006). The spherical Slepian basis, a set of bandlimited functions that have the majority of their energy concentrated by optimization inside of an arbitrarily defined region, provides an efficient way for the analysis and representation of coseismic gravity signatures and other spatio-spectrally localized geophysical signals (Simons *et al.,* 2006, 2009).

While the slip distribution for the Maule earthquake has been modeled either seismically by analyzing teleseismic records (Lay *et al.,* 2010) or inverted using geodetic measurements including GPS and InSAR (Delouis *et al.,* 2010; Lorito *et al.,* 2010; Tong *et al.,* 2010; Vigny *et al.,* 2011), non-negligible discrepancies exist in the inverted fault parameters from these studies. The discrepancies are attributable to the following factors. Seismic and geologic data often do not completely constrain the fault geometry, particularly when the primary fault rupture does not reach Earth's surface. Determination of fault geometry often relies on aftershock distribution, which is complex: substantial aftershock activities often occur off the principal fault plane (Segall and Davis, 1997). Geodetic methods (GPS, InSAR etc.) play an important role in elucidating the geometry of the rupture. However, for undersea earthquakes, geodetic inversion tends to underestimate the slip due to lack of far-field offshore observation. In contrast, gravitational data are sensitive to deformation either on land or on the seafloor, in continental/oceanic crust and mantle, although the signal-to-noise ratio, particularly in oceanic settings, depends on the size of rupture. The question of interest is whether or not spaceborne gravimetry from GRACE may provide complementary constraints to aid fault inversion. Although previous studies reported observing coseismic and postseismic

deformation of recent great earthquakes by spaceborne gravimetry (Chen *et al.,* 2007; Han *et al.,* 2006, 2008, 2010; Heki and Matsuo, 2010; de Linage *et al.,* 2009; Panet *et al.,* 2007), none of them considered inverting the detected signals for fault parameters. Our study, for the first time, not only analyzes the sensitivity of coseismic gravity changes from spaceborne gravimetry to fault parameters, but attempts to use GRACE observations to constrain fault geometry and average slip for the 2010 Mw 8.8 Maule event.

5.2.2   Spatio-spectral Localization Analysis of GRACE Data

Here we use localized analysis with Slepian basis function to enhance the spatial resolution of the GRACE-observed coseismic gravity-change signal associated with the 2010 Maule Chilean earthquake. In this study, ninety-one GRACE Level 2 Release 04 geopotential fields from the Center for Space Research (CSR), spanning from January 2003 to August 2010, were used for analysis. These solutions, one for every month, consist of spherical harmonic coefficients up to degree and order 60, corresponding to a maximum resolution of 333km (half-wavelength).   Here in order to preserve the maximum spatial resolution, we did not decorrelate or filter the monthly Stokes coefficients (e.g., by Heki & Matsuo (2010)), in favor of using Slepian function based localization to enhance or retain the resolution of the GRACE observations, estimated at ~350km resolution.

A circularly symmetric cap of radius 10° is chosen as the concentration region. To give some examples for the Slepian bases, Figure 5.8 shows the first 9 band-limited (maximum degree $L = 60$) Slepian basis functions for the circularly symmetric region with a radius $\Theta = 10^o$ centered offshore Chile on the epicenter of the 2010 Maule earthquake. Their eigenvalues are all very close to unity indicating nearly perfect spatial concentration despite the limited bandwidth.
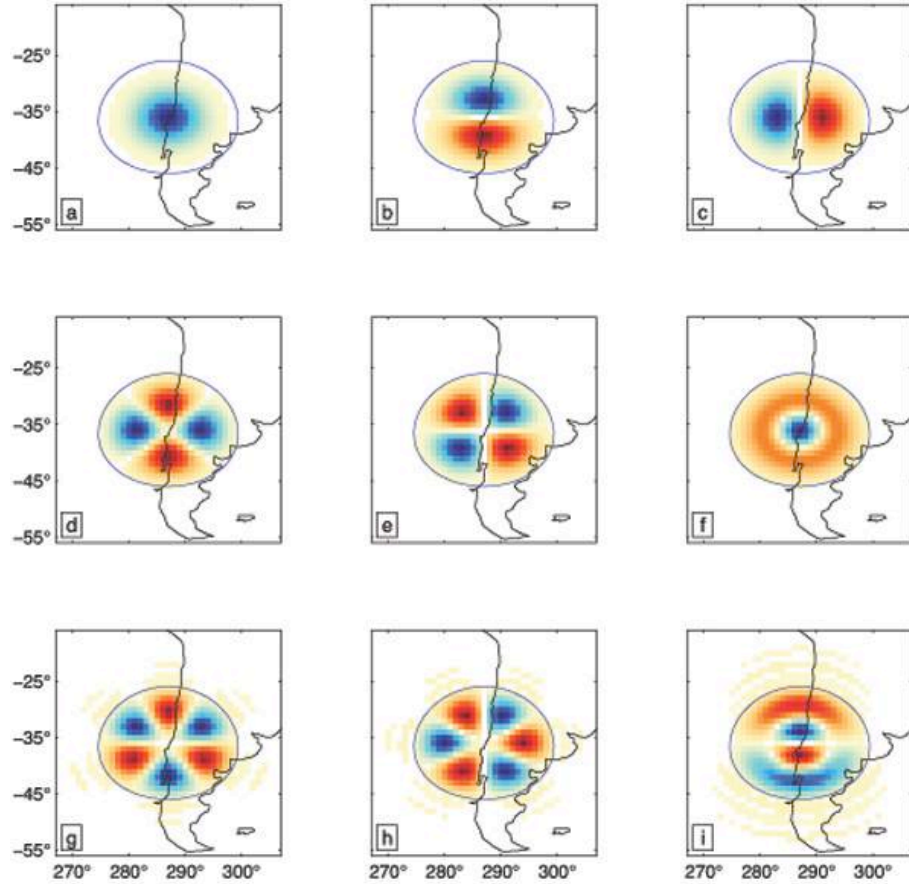
Figure 5.8: The nine best-concentrated members of the family of bandlimited Slepian eigenfunctions that are optimally concentrated within a circularly symmetric domain of radius $\Theta = 10°$ centered at the epicenter of the 2010 Maule earthquake. The bandwidth is $L = 60$. The color scale is symmetric and the sign is arbitrary.

To properly choose the center of concentration region, we check the behaviors of the time series of the Slepian coefficients as a function of the concentration center location. The concentration center is moved along a west-east profile across the epicenter, and the Slepian transformations are applied to GRACE geopotential fields every $0.5°$ on the profile. From the resulting Slepian coefficients obtained at different concentration centers, a constant term, a linear trend, the first six largest periodic components and a step function between the months of February and March 2010 were simultaneously fitted by least-squares adjustment.

In addition, the Student t-test is applied to check whether the estimated step functions, which are considered to be coseismic signals, are statistically significant. Figure 5.9 shows the estimated step values (Figure 5.9a) and the corresponding t-values (Figure 5.9b) from the 1st and 3rd Slepian coefficient series as a function of concentration

center location. No significant step is detected in other coefficients. Figure 5.9b shows that the estimated steps in the time series of the 1st Slepian coefficients are statistically significant within much of the range of the concentration centers, thus fulfilling a 95% confidence criterion ($t = 1.99$). The estimated step values achieve maximum magnitude when the concentration center is located at (69.9°W, 35.8°S), which is a point as far as almost 3° east of the earthquake epicenter. Although the jump in the time series of the 1st expansion coefficient is more pronounced when the concentration center moves eastwards from the epicenter, this comes at the expense of the 3rd coefficient, for which no other significant jumps can be detected. Figure 5.9b shows that the fitted step value in the 3rd Slepian coefficients are statistically significant (95% confidence level) only if the concentration center resides between 72.9°W and 70.9°W. If the concentration center moves eastwards further beyond 70.9°W, all the estimated step values in the 3rd coefficient become insignificant.
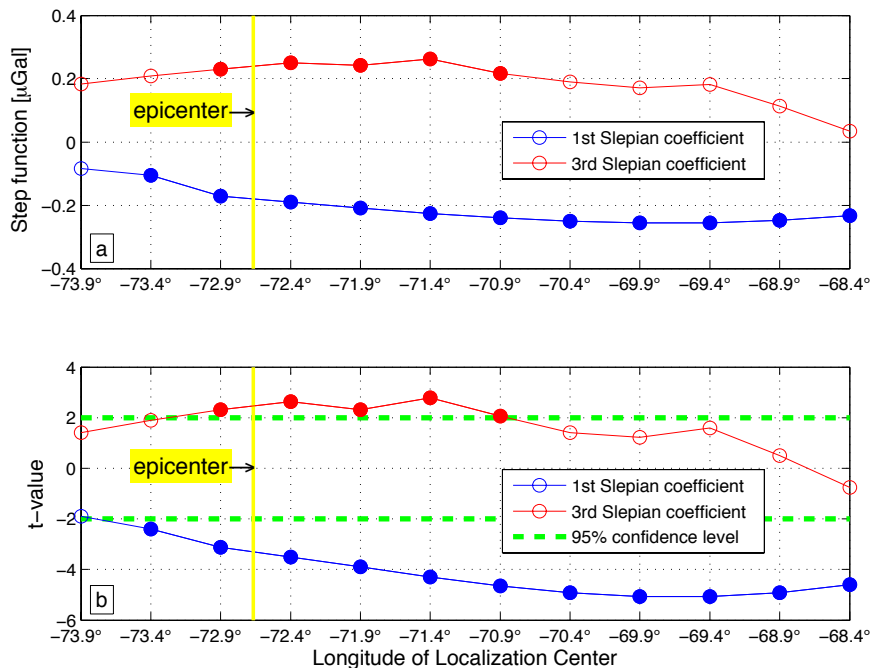
Figure 5.9: Step functions fitted from time series of the Slepian coefficients when varying the center location of the concentration domain. (a) Magnitudes of the estimated step functions; (b): the Student t-values of the estimates. Solid dots indicate estimates that are significant at the 95% confidence level.

Figure 5.10 explicitly shows the original and fitted time series when the concentration centers are located at (72.9°W, 35.8°S) and (69.9°W, 35.8°S), respectively.
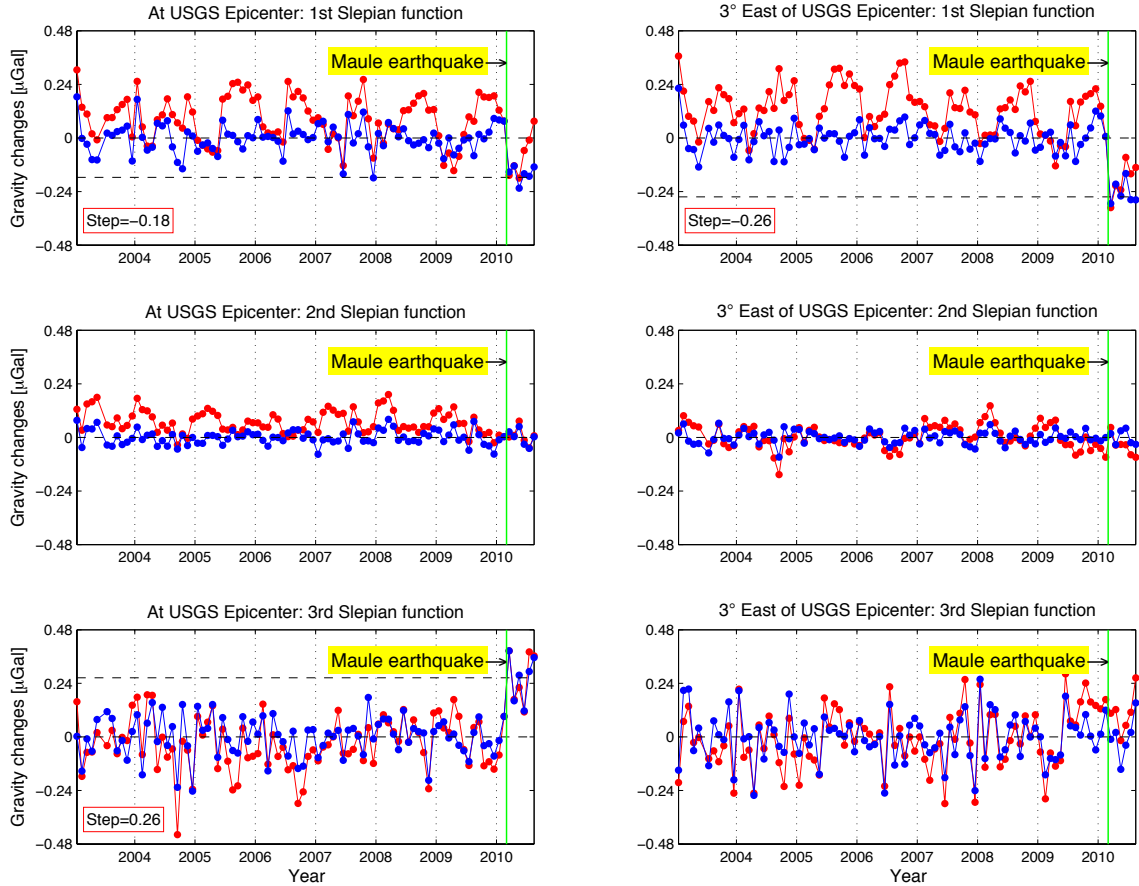
Figure 5.10: Time series of the Slepian expansion coefficients of the GRACE Level 2 Release 04 monthly gravity field solutions delivered by the Center for Space Research (CSR). Red: the original expansion coefficients. Blue: The residuals in the coefficients after removing the periodic variations fitted by the least-squares estimation. First column: the concentration region centered at the epicenter (72.9°W, 35.8°S). Second column: the concentration region centered east of the epicenter (at 69.9°W, 35.8°S).

Thus, in order to keep both significant jumps in the 1st and 3rd Slepian coefficient series and, meanwhile, to make sure that the concentration center is not too far from the epicenter, we choose the center of the concentration region at the mid point (71.9°W, 35.8°S) of the range between 72.9°W and 70.9°W, where both estimated step values in the 1st and 3rd Slepian coefficients are statistically significant. We use the step functions fitted from the 1st and 3rd functions to finally estimate the coseismic gravity changes. The results are shown in Figure 5.11.

The peak value in the negative signal on land from GRACE observation is ~8.0 μGal and the maximum positive signal is ~1.2 μGal in the ocean. It should be realized that our GRACE observation only consists of the 1st and 3rd Slepian basis functions, for which significant jumps (induced by earthquake) can be detected. We find that the

GRACE observed earthquake-induced jump is significant only in the 1st and 3rd Slepian coefficients. The positive signal in the ocean due to sea-floor uplift is only ~1 μGal at GRACE spatial resolution, this is close to the GRACE error level. We state that the GRACE observations shown in Fig 5.11 resolve almost all the negative signals on land caused by the Maule earthquake, while the detected positive signals over the ocean qualitatively correspond to seafloor uplift, but should not be quantitatively applied in the inversion.
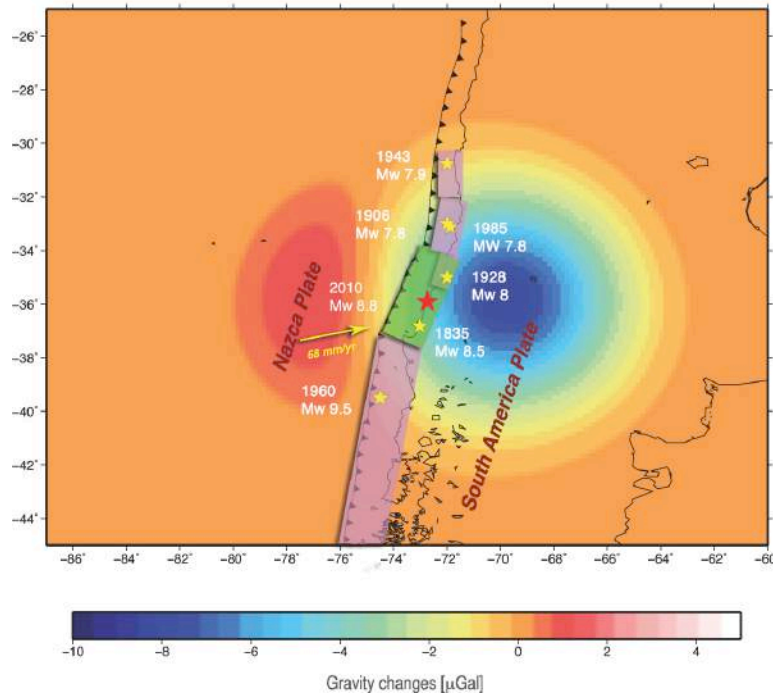
Figure 5.11: The sensitivity of coseismic gravity changes (at spatial resolution of 350km) to fault width and length in a bird's eye-view. The fault dip, strike and rake are fixed to be 16°, 17.5^o, and 90°, respectively. The upper edge of the fault is fixed at 5km depth, and the slip is fixed to be 7m uniformly. Each row has the same fault-width value, which is 50km, 150km and 250km for the 1st, 2nd and 3rd rows, respectively. Each column has the same fault-length value, which is 300km, 600km and 900km for the 1st, 2nd and 3rd columns, respectively.

5.2.3 Comparisons of current slip models

Reliable estimation of coseismic earthquake slip is necessary to evaluate the pre-locking status and the level of stress release. However, existing slip models obtained by various constraints or via inversion of observations, including uplifted/subsided biomarkers, teleseismic data, InSAR, GPS, and tsunami observations, exhibit notable differences, both in slip amplitude and distribution. Here we compare four published slip models: Model I is a finite-fault solution derived from seismic observations (USGS,

2010); Model II is an inversion using teleseismic *P* and *SH* waves (Lay *et al.,* 2010); Model III is an inversion based on InSAR interferograms and GPS displacement measurements (Tong *et al.,* 2010); and Model IV is derived by combining land-level changes from coastal bio-markers, InSAR deformation, GPS displacement and tsunami observations at tide-gauges and DART buoys (Lorito *et al.,* 2011). Inset plots (Figure 5.7) show the maps of the finite-fault slip distributions from these models, while Table 5.1 compares some key parameters. As can be seen from Table 5.1, other than the obvious discrepancies in the length and width of the fault plane, the difference in the predicted maximum slips between the four models is as large as ~13 m, and the difference in the fault depth ranges up to 6km. Significant discrepancies also can be found in the potency, the integral of the slip over the rupture surface (Ben-Menahem and Singh, 1981). Moreover, the slip distributions predicted by these models have large discrepancies. While Model I predicts more slip in the southern asperities, larger slips are concentrated to the north of the epicenter in Models II, III and IV (Figure 5.7). The last row in Table 5.1 also lists the fault parameters inverted in this study from GRACE observations, which will be discussed further below.

	Fault plane		Top edge depth	Strike	Dip	Max slip	Depth of max slip	Potency [$km^2 cm$]	Data source
	Length	Width							
Model I	540km	200km	2.9km	17.5^o	18°	14.6m	39.9km	4.6×10^7	Teleseismic waves
Model II	575km	180km	4km	18°	18°	27.8m	10.3km	6.3×10^7	Teleseismic waves
Model III	669.8km	260km	2.6km	16.8^o	15°	18.0m	18.1km	5.7×10^7	InSAR, GPS
Model IV	~625km	~200km	9km	2°–30°	10°~22°	18.8m	28.0km	5.5×10^7	InSAR, GPS, tsunami
This study	429km	146km	5km	19°	15°	8.1m (uniform)	NaN	5.1×10^7	Spaceborne gravimetry

Table 5.1: Comparisons of key characteristics in the finite-fault models of Model I by USGS (2010), Model II by Lay et al. (2010), Model III by Tong et al. (2010), and Lorito et al. (2011). The results from this study are listed as well.

Coseismic gravity changes can be computed from slip models, since coseismic slip due to the sudden unlocking of the megathrust causes an instantaneous elastic rebound of the upper plate, which translates into a distinctive pattern of uplift and subsidence at the surface and induces dilatation of the formerly compressed forearc volume. Assuming an elastic half-space, we use all four models to predict the coseismic gravity changes due to the effects of coseismic deformation including both the single-layer topographical change (uplift/subsidence) of the seafloor and the internal density changes (compression/dilatation) within the crust and mantle (Okubo, 1992). To make the model predictions commensurate with the approximate spatial resolution of the GRACE observations, all the model predictions, which are originally modeled with 0.25^o x 0.25^o grid at full resolution, are truncated to degree 60, and an isotropic Gaussian filter (Jekeli, 1981; Wahr *et al.,* 1998) with a smoothing radius of 350km is applied. The results are shown in Fig. 5.12.
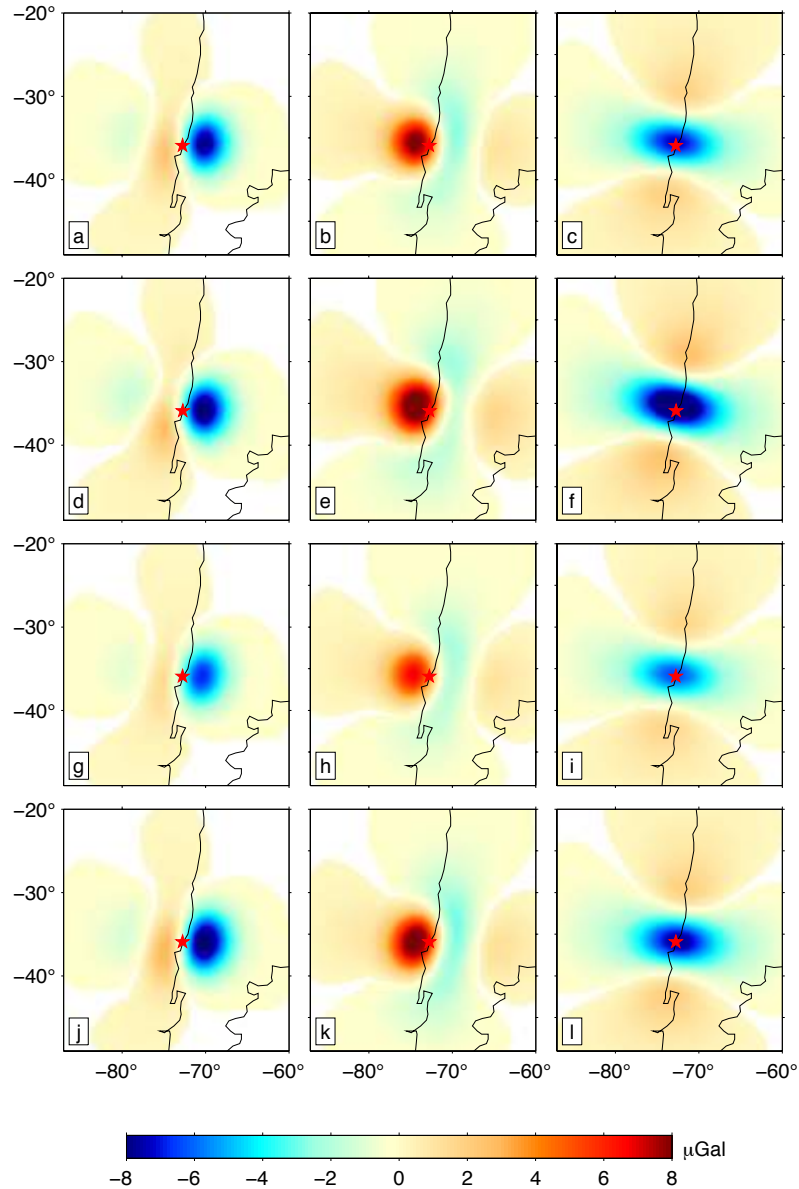
Figure 5.12: Coseismic gravity changes (μGal) predicted from the seismic fault models. (a) As inferred by adding the effect of the vertical motion of the surface shown in (b) to the effect due to internal density changes (compression and dilatation) shown in (c) from Model I; (d)–(f) are similar to (a)–(c) but predicted by Model II; (g)–(i) are similar to (a)–(c) but predicted by Model III; (j)–(l) are similar to (a)–(c) but predicted by Model IV. The data shown in each panel have been smoothed with an isotropic Gaussian filter having a radius of 350km. The red star denotes the location of the epicenter, at 35.909°S and 72.733°W (U.S. Geological Survey, Magnitude 8.8 offshore Maule, Chile, 2010, http://earthquake.usgs.gov/earthquakes/recenteqsww/Quakes/us2010tfan.php).

The spatial patterns of total gravity change predicted from all four slip models (Figure 5.12a, d, g, and j) are similar at the spatial resolution attainable by GRACE observations, and consistent with the GRACE-detected gravity changes (Figure 5.11), even though Model I places more slip in the southern asperities, whereas Models II, III and IV have larger slip north of the epicenter. All model predictions indicate apparent negative gravity changes on land east of the epicenter. Hence, we conclude that GRACE is not sensitive to the detailed slip distribution of the 2010 Chilean shock, mainly because the length of faulting is of the same order of magnitude as the limiting resolution of the GRACE data.

Although the coseismic gravity changes predicted by the models exhibit similar spatial patterns, the amplitudes from the four models are discernably different. Peak values in the negative signals on land predicted by Models I–IV are -8.1 µGal, –8.8 µGal, –6.9 µGal and -9.0 µGal, respectively (Figure 5.12). Since the four models give different slip amplitudes, they proportionally lead to different amplitude in the predicted coseismic gravity change. Although both Models I & II are derived from teleseismic wave analysis, the maximum slip amplitudes are 14.6 m and 27.8 m respectively, presumably because of different model assumptions and data distributions, and different intrinsic ranges of apparent velocities in the observations (Lay *et al.,* 2010). Both Models III and IV inverted data from land-based InSAR deformation and GPS displacement measurements. Model III, which has a maximum slip of 18 m, probably underestimates the amount of slip at shallower depth as a consequence of lacking offshore observations (Tong *et al.,* 2010). Using tsunami observations to further constrain the offshore displacement, Model IV provides a larger estimate of 18.8 m as the peak value in slip.

GRACE-detected gravity changes, which peak at –7.9 µGal over land, are compared with model predictions on three profiles along latitudes 32°S, 36°S and 39°S (Figure 5.13). Although both Models III and IV used the same InSAR data, they provide the smallest and largest magnitudes of gravity changes, respectively, among the GRACE observation and the models, along all three profiles (Figure 5.13). The large discrepancy between these two models can probably be attributed to the fact that the tsunami observations are used in Model IV to estimate the offshore displacement. The amplitudes of predicted gravity changes by seismically derived models (Models I and II) generally reside in the extent bounded by Models III and IV. Along the 32°S and 36°S profiles, GRACE observations have peak values around longitude 70°W, and they are approximately equal to the means of the model predicted maximum amplitudes. However, to the south of the rupture along 39°S profile, the GRACE-observed gravity change, which is of the same order of magnitude as the prediction from Model IV, is relatively larger than the predictions from Models I, II, and III.
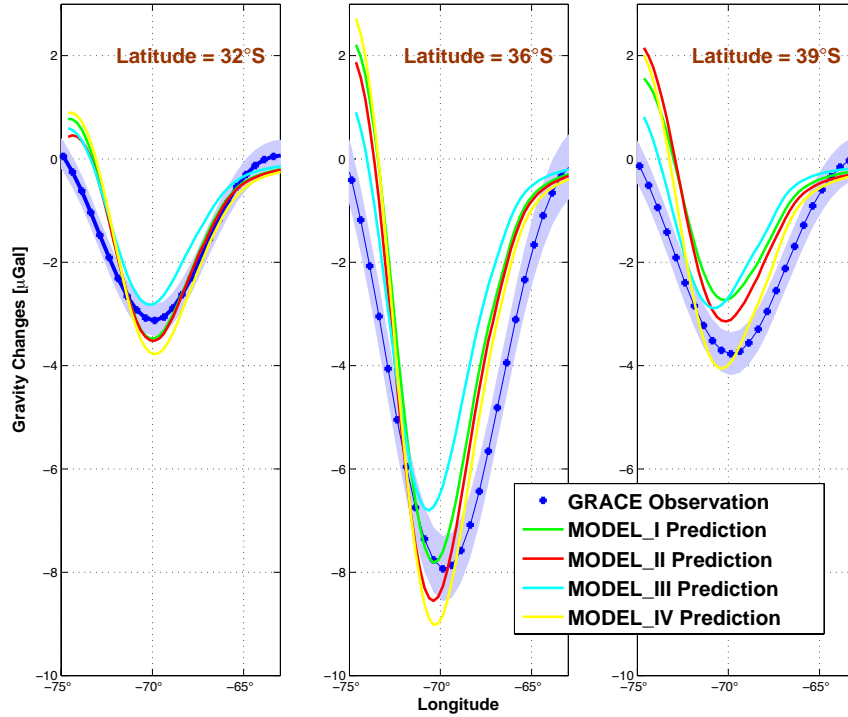
Figure 5.13: Comparisons of coseismic gravity changes for the profiles along 32°S (left), 36°S (middle) and 39°S (right) between GRACE observations (shading indicates the estimated error) and the predictions from the four finite-fault models.

Since there is no *a priori* error information available for the observations, we choose to use the model error (*a posteriori* error estimation) to provide error information for our GRACE observation. Since the earthquake-induced jumps are fitted from the time series of the 1st and 3rd Slepian coefficients by least-squares adjustment, we can estimate the data variance from the residuals in the time series, and thence the variance of the fitted jumps. The blue shadings along with the GRACE observation profiles in Figure 5.13 indicate the estimated model errors based on this procedure. We conclude that the GRACE–derived amplitude can be used to constrain the fault parameters of the Maule earthquake, but these are discernibly different from the amplitudes derived by other coseismic slip models.

5.2.4   Estimation of Fault Parameters From GRACE Observations

We first analyze the sensitivity of the coseismic gravity changes to various fault parameters. A finite fault plane is set with length, depth, dip, strike and rake fixed at 500km, 4km, 16°, 17.5°, and 90°, respectively. The width of the fault plane is made to vary between 100km and 200km in steps of 50km, and the uniform slip on the fault plane varies from 5m to 11m for each width value. Along an east-west profile across the middle of the fault plane, the coseismic gravity changes for each case are shown in Figure 5.14

78

(left). We can see from Figure 5.14 (left) that when the width of the fault plane is 100km, 150km, or 200km, the trough values of the predicted gravity change on the profile occur around longitudes -70.3^o, -69.8^o; and -68.8^o, respectively. In other words, with increasing of fault-plane width, the location of the minimum in the observed gravity change moves to the east. Moreover, for a fixed width, the amplitude of the predicted gravity change increases proportionally with slip amplitude. Therefore, the location and amplitude of the minimum value in the coseismic gravity observation, i.e., the shape/size of the observed gravity profile, provide constraints on the width of the fault plane and its average slip.
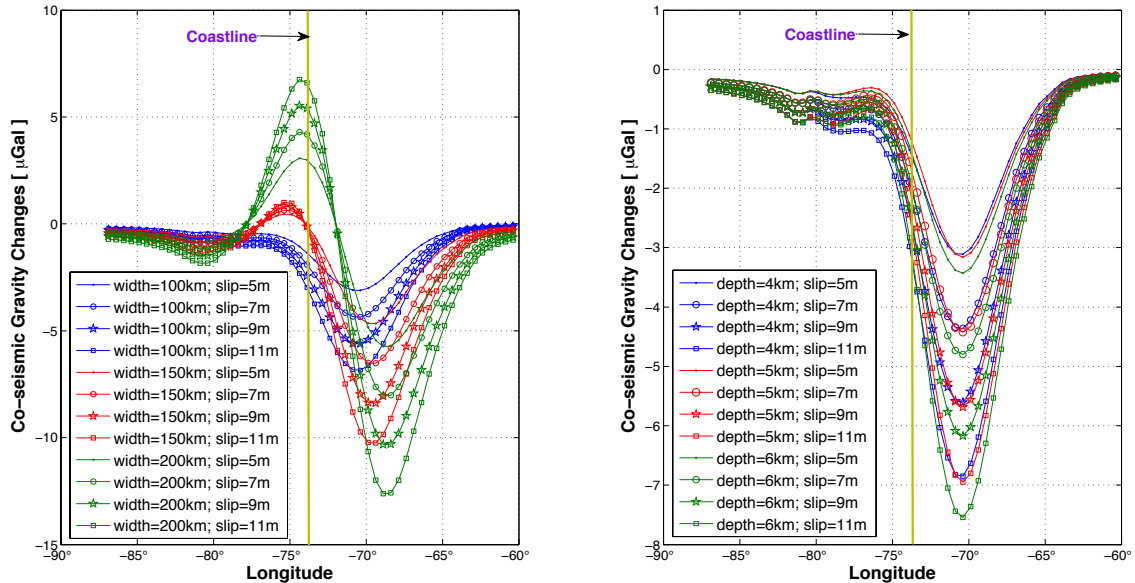
Figure 5.14: The coseismic gravity changes (at spatial resolution of 350km) along an east-west profile across the middle of the fault plane for synthetic faulting scenarios: (Left) Fault length, depth, dip, strike, rake are fixed at 500km, 4km, 16°, 17.5^o, and 90°, respectively. The width of the fault plane varies from 100km to 150km with steps of 50km, and the uniform slip on the fault plane take values from 5m to 11m for each width. (Right) Fault-plane length, width, dip, strike and rake are fixed at 500km, 100km, 16°, 17.5^o, and 90°, respectively. The depth of the top edge of the fault varies from 4km to 6km in steps of 1km, and the uniform slip on the fault plane take values from 5m to 11m for each width. This example shows the sensitivity of coseismic gravity changes to faulting parameters.

Figure 5.15 gives a map view to further show the sensitivity of coseismic gravity changes to fault width and length. As in the previous example, the fault dip, strike and rake are fixed to be 16°, 17.5^o, and 90°, respectively. The upper edge of the fault is set at 5km depth, and the slip is uniformly fixed at 7m. The width of the fault plane is set to be 50km, 150km and 250km, respectively, and for each fixed width, the coseismic gravity changes are computed for fault lengths of 300km, 600km and 900km. For certain fixed

fault lengths, the location of the negative peak in the predicted coseismic gravity changes moves eastwards with increased fault width. For fixed fault width, the spatial pattern of the gravity changes becomes more elongated in the north-south direction as the fault length grows.
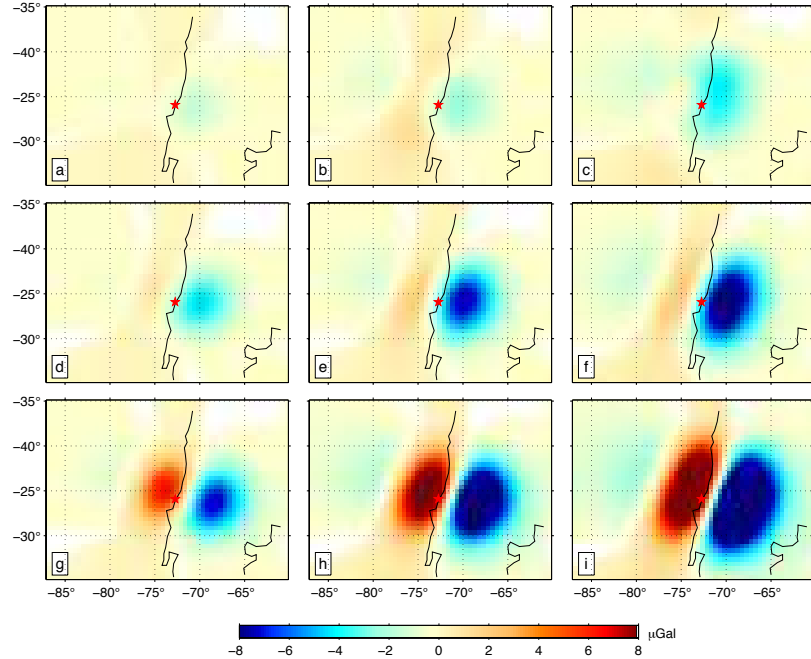
Figure 5.15: The sensitivity of coseismic gravity changes (at spatial resolution of 350km) to fault width and length in a map view. The fault dip, strike and rake are fixed to be 16°, 17.5^o, and 90°, respectively. The upper edge of the fault is fixed at 5km depth, and the slip is fixed to be 7m uniformly. Each row has the same fault-width value, which is 50km, 150km and 250km for the 1st, 2nd and 3rd rows, respectively. Each column has the same fault-length value, which is 300km, 600km and900 km for the 1st, 2nd and 3rd columns, respectively.

Although GRACE detected coseismic gravity change is sensitive to fault length, width and average slip, there is trade-off between fault depth and average slip. To show this, a fault plane (length, dip, strike and rake are fixed to be 500km, 16°, 17.5^o, and 90° respectively) is placed at depth (measured down to the upper edge of the fault) of 4km, 5km and 6km, respectively. At each depth, the coseismic gravity changes are computed with slip of 5m, 7m, 9m and 11m, respectively. Figure 5.14 (right) shows the gravity changes along the same profile as in Figure 5.14 (left). We can clearly see the trade-off between the depth and slip. To be specific, at a spatial resolution of 350km, the coseismic gravity changes given by a fault at a depth of 5km and slip of 11m are similar to the ones computed from a fault at a depth of 6km and slip of 10m. For the depth range from 4km to 6km in this case, the trade-off between depth and slip would cause maximum errors of

~1m in the slip estimation using coseismic gravity changes only. Thus, for the Maule earthquake, the coseismic gravity changes observed by GRACE add little constraint to the depth estimation for the fault plane. The depth information estimated from other observations (e.g. seismic or geodetic observations) should be used in order to invert GRACE-derived observations for other fault parameters.

Here, we use the GRACE observations to invert for fault parameters. A simplified elastic model with uniform slip on the fault plane is assumed for the study. Here we fix the strike angles to be 19° as given by the global CMT solutions (GCMT, 2011). We assume a uniform dip of 15°, which is consistent with the dip angle used by Vigny *et al.* (2011). By jointly inverting the continuous GPS, survey GPS and InSAR observations, Vigny *et al.* (2011) suggested that the rupture started from 5km depth along the megathrust interface. Therefore, we choose the depth to the top edge of the fault as 5km. Based on previous analysis, even if there is ±1km uncertainty in depth value, the trade-off effect in the slip estimate should be less than 1m. The rake angle is fixed as 90° in our inversion, i.e., we only invert for the thrust component and neglect the right-lateral strike slip component. This simplification can be justified by following two points: first of all, as shown by Tong *et al.* (2010), the strike-slip seismic moment is one order of magnitude smaller than the thrust (dip-slip) seismic moment; secondly, there is no significant jump detected in the time series of the coefficient associated to the 5th Slepian basis function (Fig. 5.8e), whose shape matches the spatial pattern of the coseismic gravity changes due to strike slip motion.

We apply the SA algorithm by defining the cost function (energy function) as the sum of squares of the differences between GRACE-observed gravity changes and model predictions on three profiles along latitudes 32^oS, 36^oS, and 39^oS. The state space consists of the length, width and average slip. Figure 5.16*a through c* show that the histograms of the accepted samplings for fault length, width and slip after convergence of the iterations. The ultimate optimal estimate for fault length, width and slip are, 429km, 146km, and 8.1m, respectively. In order to further investigate uncertainties induced by GRACE observation errors in these estimated parameters, we also use the lower and upper bounds of the *a posteriori* error estimates for the GRACE observations to invert for fault-plane size and average slip. At the lower bound (shaded light blue in Figure 5.13) the algorithm converges to a fault plane with length 430km, width 143km, and average slip of 9.1m (see Figure 5.16*d* through *f* for the histograms of the solutions), while using the upper bound of the GRACE data yields estimates of fault-plane length, width and average slip of 427km, 149km and 7.1m, respectively. Similarly, Figure 5.16*g* through *i* shows the converged of fault length, width and slip estimates at the end of iteration. The maximum widths of the global minimum in state space for above three inversions are 8km, 4km and 0.3m for length, width and slip, respectively.
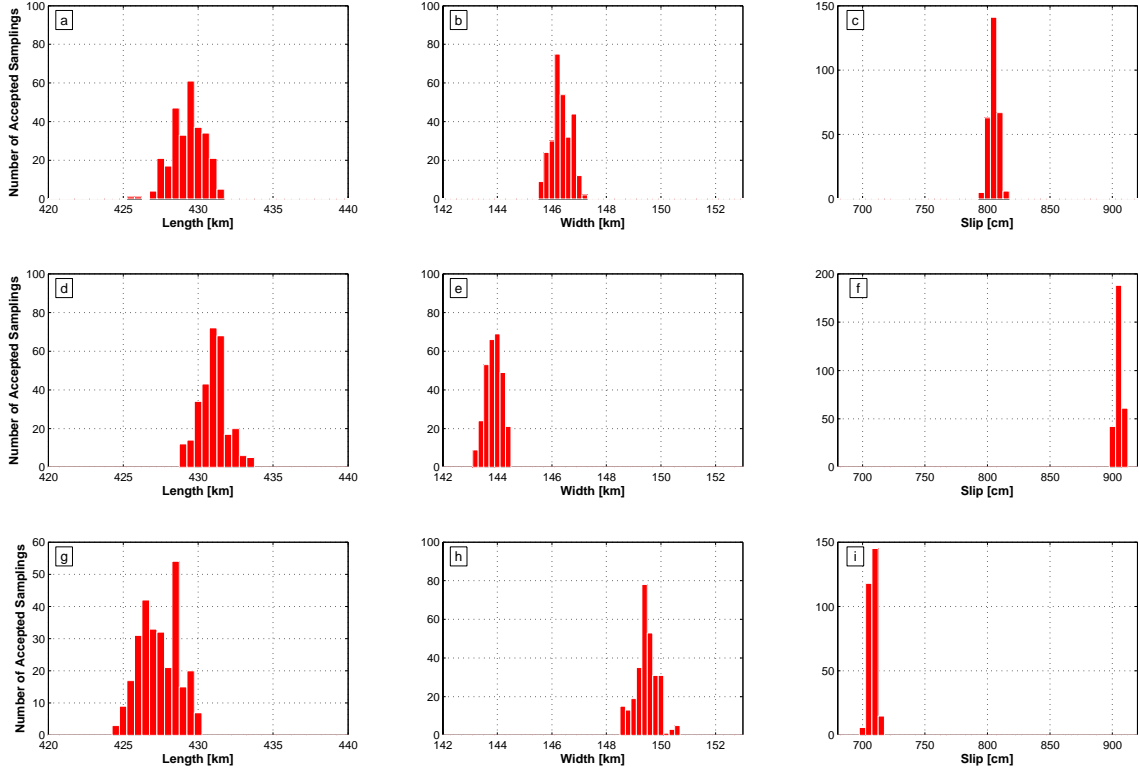
Figure 5.16: Histogram of the accepted samplings for variables of fault length, width and slip in their state spaces at the lowest temperature of convergence of the simulated annealing algorithm. (a)–(c): using GRACE detected gravity changes as input for inversion; (d)–(f): using the lower bounds of the *a posteriori* error estimates for the GRACE observations as input for inversion; (g)–(i): using the upper bounds of the *a posteriori* error estimates for the GRACE observations as input for inversion.

We finally estimate the fault length and width as 429±6km, 146±5km, respectively, and the average slip as 8.1±1.2m. Assuming a mean rigidity of 33GPa (Vigny *et al.* 2011), the new GRACE-derived total seismic moment is 1.67×10^{22} Nm, resulting in a moment-magnitude Mw 8.75, which is comparable to contemporary solutions (Mw 8.8). Since the rake is fixed as 90° in the inversion, our estimated Mw 8.75 value only corresponds to the thrust part of the total moment magnitude, although the seismic moment of the strike-slip component is one order of magnitude smaller than that of thrust component.

5.2.5   Discussion

To acquire the information on ruptured fault geometry and co-seismic slip distribution helps one to better understand the earthquake mechanism and to evaluate the seismic hazard potential after large earthquakes. Due to the intrinsic limitations in fault inversions using either teleseismic records or geodetic measurements, discrepancies exist

in published slip models for the Mw8.8 2010 Maule earthquake, that translate in uncertainties regarding the assessment of short-term seismic hazard left inside the Concepción-Constitución seismic gap (Moreno *et al.,* 2010; Lorito *et al.,* 2011; Lay, 2011). Despite its low spatial resolution (currently at 350km half-wavelength), we have demonstrated here that GRACE spaceborne gravimetry is useful to complement seismic and geodetic observations because the total permanent gravity change result from great earthquakes observed by GRACE is a distinct observation type, and that the observation extends to both on land and offshore.

By investigating the sensitivity of coseismic gravity changes to various fault parameters, we find that variations observed by GRACE cannot identify differences in detailed slip distributions for the 2010 Mw 8.8 Maule earthquake. However, using a simple elastic dislocation model we can estimate uniform average slip, length and width of the rupture interface. Although we noted a tradeoff between average slip and fault depth, fixing the later with independent information (Vigny *et al.,* 2011), we find the amplitude of the observed coseismic gravity change is proportional to the average slip on the fault plane. The location of the peak value of coseismic gravity change indicates the down-dip limit of the rupture, i.e., the width the fault plane (~146km), while the south-north extent of the gravity change signature constrains the fault length (~429km). The dimensions and location of our ruptured fault coincide with the extent of significant co-seismic slip (> 2m) predicted by published models. Our inversion algorithm estimated an average slip of 8.1 m, which gives a seismic moment ($1.67\text{x}10^{22}$ Nm) and moment-magnitude (Mw 8.75), similar to previous estimations.

Rapid afterslip on the ruptured fault is the predominant post-seismic deformation mechanism and typically occurs over timescales of ~months (Perfettini *et al.,* 2010). Afterslip can be attributed to either aseismic slip in the sedimentary layer overlying the fault, coseismic slip generated by aftershocks, or silent slow slip triggered by the mainshock-induced stress and friction changes (Vigny *et al.,* 2011). Because of its temporal resolution of a month, GRACE cannot identify gravity changes due to these earliest manifestations of post-seismic deformation, and therefore is not able to separate them from the coseismic estimates. By using campaign- and continuous-GPS observations, Vigny *et al.* (2011) has shown that afterslip on the mega-thrust interface within 12 days following the main shock accounts for only 4% of the coseismic moment, and the maximum post-seismic slip is estimated to be ~50 cm. This lies within the error range of the GRACE-estimated slip provided in the previous section and it seems unlikely that afterslip could seriously contaminate our co-seismic slip estimation.

In the extreme case that the plate interface in Constitución gap has remained fully locked for 175 years between 1835 and 2010, the cumulated slip deficit before the Maule earthquake at a rate of 62–68 mm/yr of plate convergence (Kendrick *et al.,* 2003) would be on the order of 11–12 m. The difference with our estimated average slip could indicate that a remaining slip deficit of 3–4 m could still generate a large earthquake (Mw8.5 if occurring in the same fault plane of our model) to fully close the gap, supporting the

conclusion of Lorito *et al.* (2011). However, some alternatives must be considered on this limiting case.

GPS-derived velocity fields for the decade before the 2010 Maule earthquake show an overall strong coupling in this region (Khazaradze & Klotz, 2003; Ruegg *et al.,* 2009; Moreno *et al.,* 2010). However, there is no evidence that bears on whether the plate interface ever experienced aseismic slip during interseismic phase before 2000, especially as afterslips after the 1835 earthquake. It has been shown (Perfettini *et al.,* 2010; Ide *et al.,* 2007) that slow or silent slip events during the interseismic and post-seismic phases are common features of subduction-zone megathrusts, and can release large amounts of seismic moment (10-70% of the budget predicted by plate convergence). With the available information, it is impossible to discard such events as potential factors reducing the slip deficit before the Maule earthquake and hence explaining the difference with our average co-seismic estimation. Moreover, aseismic slip normally occurs on discrete patches of the megathrust, hence generates a spatially variable distribution of plate locking, which can be imaged by interseismic GPS velocity fields (Moreno *et al.,* 2010; Loveless & Meade, 2011). When computed with the same model for geometry and rheology of the subduction zone, co-seismic slip patches seem to roughly coincide with strongly locked regions over the megathrust, as shown by Moreno *et al.* (2010) for the Maule event, and by Loveless & Meade (2011) for the 2011 Mw9 Tohoku-Oki earthquake. GRACE can't recognize the detailed spatially variable slip distribution, but the averaged slip over the whole ruptured megathrust. Therefore, it is hard to tell whether or not the Constitución gap is completely closed just from the slip deficit of 3-4m between GRACE observed average coseismic slip (~8m) and expected value (11-12m). However, we conclude that most of the strain accumulated since 1835 in the Concepción-Constitución gap had been released by the 2010 Maule earthquake.

5.3   Coseismic and Postseismic Deformation of the 2011 Tohoku-Oki Earthquake Constrained by GRACE

5.3.1   Introduction

The 11 March 2011 moment magnitude (Mw) 9.0 Tohoku-Oki earthquake ruptured along the interplate boundary off the eastern shore of northern Honshu, and generated a devastating tsunami that swept the coastal area along the northern part of Japan. This event released a large part of the strain accumulated for a long time interval due to the subduction of the Pacific plate underneath the North America plate at a rate of 92 mm/yr (DeMets *et al.,* 1990). There is no historical record for any massive earthquakes near this location and with similar magnitude as the 2011 event, except for the 869 AD Jōgan Sanriku earthquake and the resulting tsunami of the Mutsu province (Minoura *et al.,* 2001).

After the Tohoku-Oki earthquake, large postseismic deformations were observed by the GPS Earth Observation Network (GEONET) operated by the Geospatial Information Authority of Japan (GSI). Based on the geodetic observations, large after-

slip with thrust mechanisms, is found outside of the area of the major coseismic slip (Ozawa *et al.,* 2011*;* Simons *et al.,* 2011). About 14 days after the Tohoku-Oki earthquake, the moment of after-slip reached a value ~10% of the main shock (Ozawa *et al.,* 2011).

The slip on the megathrust interface of the 2011 Tohoku-Oki event led to a large deformation on the sea floor, on land, and in the crust and upper mantle surrounding the rupture region. For example, the seafloor near the trench was moved east-southeast tens of meters horizontally, and with several meters of uplift (Fujiwara *et al.,* 2011; Sato *et al.,* 2011). On land, the largest coseismic displacement was ~5m toward the east-southeast with ~1m subsidence as observed by the GEONET. The earthquake-induced deformation consequently changed the Earth's gravity field permanently. Matsuo and Heki (2011) were the first to publish an observation of the coseismic deformation of the Tohoku-Oki earthquake using GRACE data. Here our focus is to use GRACE observations to invert for the composite slip, and thus to provide a complimentary constraint on the coseismic and postseimic deformation resulting from the great March 2011 Mw 9.0 Tohoku-Oki earthquake.

5.3.2   Spatiospectial Localization Analysis of GRACE Data

In this study, seventy-seven GRACE Level 2 Release 04 monthly geopotential fields from the University of Texas Center for Space Research (CSR), spanning the interval from January 2005 through July 2011, were processed. No solutions for January 2011 and June 2011 are available. Each monthly solution consists of fully normalized spherical harmonic Stokes coefficients complete to degree and order 60, corresponding to a maximum spatial resolution on the order of 333 km (half-wavelength) at the equator. The spatial resolution increases with latitude as the satellite orbits converge at the polar region. Our approach relies on a spatio-spectral localization method which represents the gravity changes resulting from the earthquake, via the spherical harmonic representations of changes in the global gravity field solution transformed to the Slepian basis [*Simons et al.,* 2006].

In order to preserve or maximize the spatial resolution of the coseismic (and postseismic) gravity changes, no post-processing is applied to remove the 'longitudinal-stripe' high-frequency errors in the GRACE temporal gravitational solutions, since any post-processing such as de-striping or decorrelation (e.g., Swenson and Wahr, 2006) would remove errors as well as seismic gravity change signals which happen to be near the longitudinal patterns or stripes, distorting the resulting gravity change observations. Here, we just applied a 350 km isotropic Gaussian filter to suppress the errors at short wavelength of the GRACE L2 monthly gravity field solutions. The annual, semi-annual signals and 161-day tidal S_2 aliasing terms are further removed from these solutions, creating an immediate data set close to the spatial resolution of the original GRACE solution at 333 km (half-wavelength at the equator). Finally, the Slepian transformation is applied to the filtered spherical harmonic coefficients with the concentration domain defined by a circularly symmetric sphere cap of co-latitudinal radius $\Theta=7^o$ centered at the Global Centroid Moment Tensor Project (GCMT) epicenter of the Tohoku-Oki

earthquake ($\lambda=143.05^{o}$,$\varphi=37.52^{o}$) (http://www.globalcmt.org). Figure 5.17 shows the Slepian coefficients (Figure 5.17*b, d, f, h, j*) of the top five optimally localized Slepian basis functions (Figure 5.17*a, c, e, g, i*), whose spatial patterns match the pattern of the gravitational potential perturbations due to double-couple point-source earthquakes (Simons *et al.,* 2009). Significant jumps can be clearly seen in the time series of the 1st, 3rd, 4th and 5th Slepian coefficients during the period of March 2011 Tohoku-Oki earthquake. We hereby assume that the jumps are due to earthquake-induced seismic deformations.
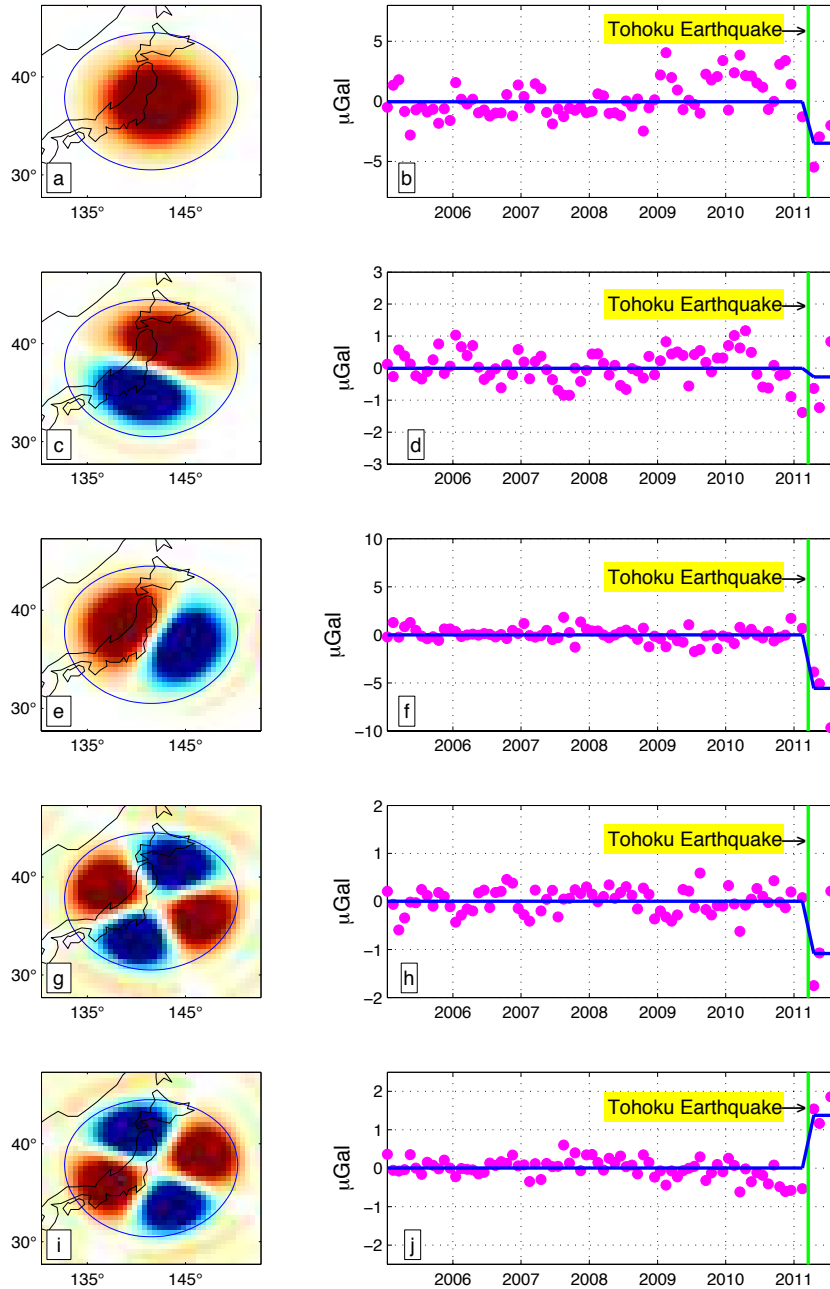
Figure 5.17: a), c), e), g) and i): Top five bandlimited Slepian functions (maximum spherical harmonic degree of 60) that are optimally concentrated within a circularly symmetric domain of colatitudinal radius $\Theta=7^{o}$ center on the Global Centroid Moment Tensor Project (GCMT) epicenter of Tohoku-Oki earthquake ($\lambda=143.05^{o}$,$\varphi=37.52^{o}$); b), d), f), h), j): Time series of the corresponding Slepian expansion coefficients of the GRACE Level 2 Release 04 monthly gravity field solutions delivered by the Center for Space Research (CSR). Pink: the original expansion coefficients (after removal of the

87

annual, semi-annual and tidal S2 aliasing terms). Blue: The mean values before and after Tohoku-Oki earthquake, as well as the earthquake-induced jump in the time series computed by differentiating the two mean values.

Figure 5.18 shows the gravity change in the space domain, which is recovered from fitted parameters representing a jump in Slepian domain. The maximum positive gravity changes detected by GRACE is 3.69 μgal in the ocean east of Honshu, Japan. These positive gravity change signals result from seafloor uplift. The negative gravity changes, which are jointly caused by seafloor and land subsidence and crust dilatation, mainly reside over the west boundary of Tohoku, with the peak value of -8.75 μgal located just north of Sado Island. By estimating the *a posteriori* variance of unit weight, we deduced that the 1-σ uncertainty is at ~1.60 μgal for our Slepian localized GRACE observations of the Tohoku-Oki seismic deformation.
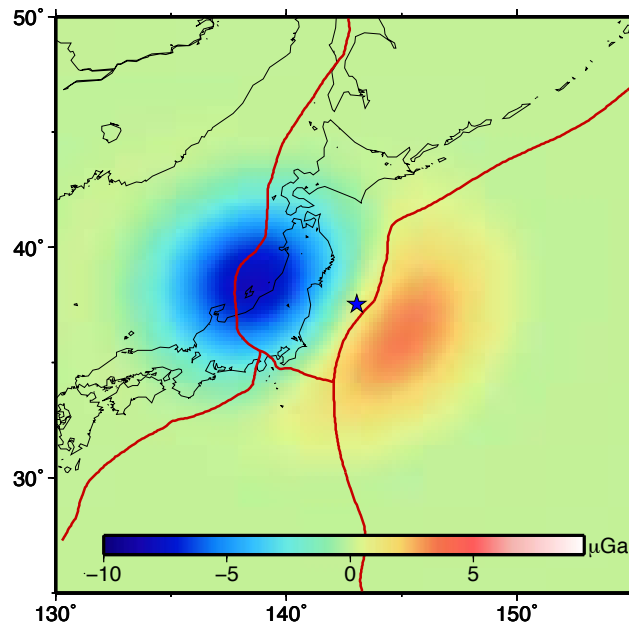
Figure 5.18: The gravity changes, in units of μGal, due to coseismic and postseimic deformation associated to the March 2011 Tohoku-Oki earthquake obtained using spatio-spectral Slepian localization analysis of monthly GRACE solutions. The postseismic signal refers to the deformation during period between March 11 and the end of July. The blue star denotes the GCMT epicenter.

5.3.3   Model Predictions

Figure 5.19 (left to right, the first three panels) shows three slip models considered in this study: Model I (Figure 5.19a) is jointly inverted from teleseismic *P* waves, broadband Rayleigh wave records as well as high-rate GPS measurements [Ammon *et al.,* 2011], while Model II (Figure 5.19b, Shao *et al.,* 2011) and Model III

(Figure 5.19c, Hayes, 2011,
http://earthquake.usgs.gov/earthquakes/eqinthenews/2011/usc0001xgp/finite_fault.php)
are derived from teleseismic body and surface waves. The predicted postseismic slip
displacement model (Figure 5.19d, last panel, with a different color scale) is from Ozawa
et al. (2011) over the time period between 12–25 March 2011. Table 5.2 lists some key
parameters for the three coseismic slip models (Models I, II and III).

	Fault plane		Max slip [m]	Depth of max slip [km]	Potency [km²cm]	Slip > 10m		Slip > 20m		Data source
	Length	Width				Area [km²]	Average slip [m]	Area [km²]	Average slip [m]	
Model I	600 km	210 km	41.0	19.7	10.5×10^7	81000	23.2	46000	29.8	Teleseismic waves, GPS
Model II	475 km	200 km	60.0	16.1	11.9×10^7	37000	27.4	20500	37.7	Teleseismic waves
Model III	625 km	260 km	33.5	14.6	9.2×10^7	30500	17.6	8500	26.7	Teleseismic waves

Table 5.2: Comparisons among key parameters of different slip models of 2011 Tohoku-Oki earthquake.

The coseismic and postseismic gravity changes are then computed for the four models assuming a homogeneous half-space formalism (Okubo, 1992). The effect of water layer is taken into account by considering the density contrast between crust and ocean water as the sea floor moves vertically. In order to compare with GRACE observations, the model-predicted coseismic gravity changes at full resolution are truncated to spherical harmonic degree complete to 60, and then spatially filtered using a Gaussian filter with radius of 350 km half-wavelength. Figure 5.19e~g shows, respectively, the coseismic gravity changes predicted by the three models (Figures 5.19a~c), and Figure 5.19h shows the postseismic gravity changes predicted from the Ozawa *et al.* (2011) model with a different color scale. Similar to the Slepian-localized GRACE observations (for composite co- and postseismic deformations) given in Figure 5.18, all predictions shows a bi-polar pattern, with negative gravity changes west of the epicenter and positive changes over the ocean east of the Japan trench. The peak negative gravity changes calculated from Model I, II and III are –7.0, –6.7 and –6.7μGal, respectively, while the predicted maximum positive values are 1.6, 2.8 and 2.0μGal. The amplitudes of all gravity changes predicted in the coseismic model are smaller than the signal detected by GRACE, which gives –8.75±1.62 and 3.69±1.62μGal as peak values in negative and positive gravity changes, respectively.
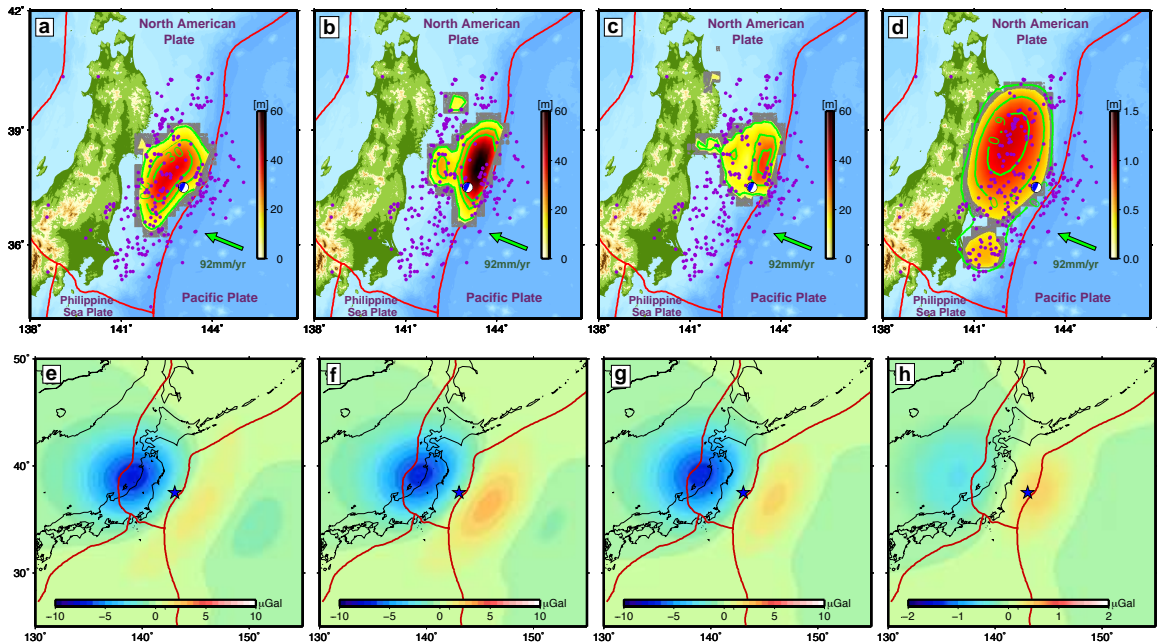
Figure 5.19: a) ~ c): Coseismic slip distributions (in units of m) estimated by three models: (a) Model I by Ammon *et al.* (2011), (b) Model II by Shao *et al.* (2011) and (c) Model III by Hayes (2011) (http://earthquake.usgs.gov/earthquakes/eqinthenews/2011/usc0001xgp/finite_fault.php). The green contours of slips are at 10m, 20m and 30m, respectively. (d): postseismic slip estimated by Ozawa *et al.* (2011) for 12-25 March 2011. The contours are at 0.3m 0.6m

and 0.9m (at a different scale). The red lines describe plate boundaries, and the green arrow indicates relative motions between the Pacific Plate and North American Plate. The purple dots show the epicenters of the Tohoku-Oki earthquake aftershocks between 11 March–24 April 2011, which are taken from the GCMT. The focal mechanism of Tohoku-Oki earthquake is plotted in blue. e)~h): The gravity changes predicted by the corresponding models in a)~d) respectively, but truncated to spherical harmonic degree 60 and spatially smoothed using a Gaussian filter of radius 350km.

In order to further check the effect of Earth's curvature and radial heterogeneity on predicted coseismic gravity change, we calculated the coseismic gravity changes from three models: (1) by Ammon *et al*. (2011), (2) by Shao *et al.* (2011) and (3) by Hayes (2011), using the numerical codes developed by W. Sun (Sun & Okubo, 1998), which assumes the dislocation is in a layered spherical Earth. Figure 5.20 shows the results. The peak negative gravity changes predicted by three models are –4.9, –6.3 and –6.0μGal, respectively; while the maximum positive gravity changes are 4.7, 3.1 and 3.5μGal, respectively. Comparing with the predictions based on the assumption of a homogeneous half-space, the magnitudes of negative gravity change become even smaller when spherical model is used, while the magnitudes of positive signals get amplified. For Model III, the maximum discrepancy between these two sets of predictions is 0.7μGal. However, for Model I, the maximum discrepancy are considerably bigger. Model I places large slips in much deeper than the other two, which is much harder to support the slip model, but combined with large slip, such slip is larger. such information as the direct seafloor measurement, large tsunami signals, or the aftershocks. Thus, we think the uncertainty in the predictions due to the spherical and layered Earth, should be around 1μGal for Tohoku-Oki earthquake, at the commensurate GRACE spatial resolution currently estimated at 350km, half-wavelength.
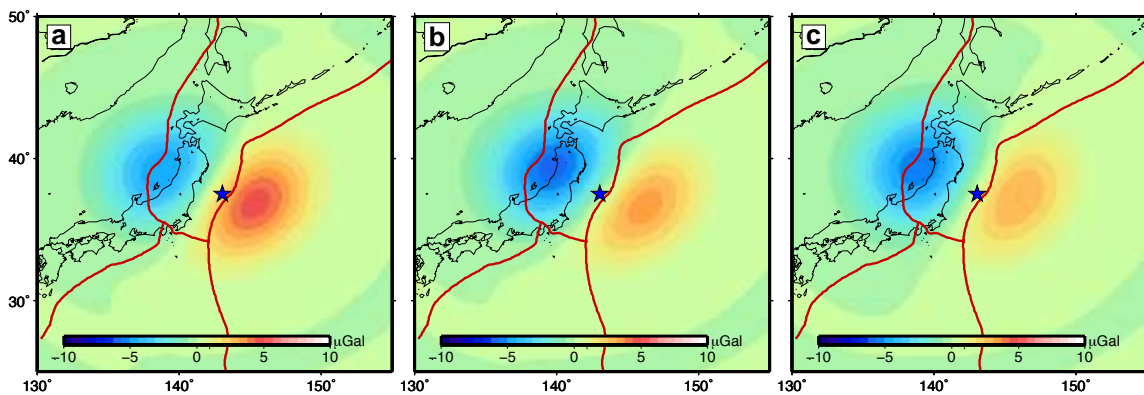
Figure 5.20: Coseismic gravity changes calculated by three models: a) by Ammon *et al*. (2011), b) by Shao *et al.* (2011) and c) by Hayes (2011) [http://earthquake.usgs.gov/earthquakes/eqinthenews/2011/usc0001xgp/finite_fault.php]. The calculation is implemented by the numerical codes by W. Sun (Sun & Okubo, 1998).

5.3.4 Sensitivity Analysis

Here, we analyze the sensitivity of GRACE observed coseismic and postseismic gravity changes to fault parameters, i.e., fault length, width, depth and slip. For this purpose, an artificial fault plane, which has strike, dip, and rake of 203°, 10° and 90° respectively, is placed with its top edge parallel to Japan trench.

First, the fault length and depth are fixed at 300km and 1km, respectively, and the fault width is allowed to take values of 100km, 200km and300 km. For each width value, the seismic gravity changes at resolution of 350km half-wavelength are computed for uniform slip of 5m, 7m and 9m, respectively. Figure 5.21 shows the calculated coseismic gravity changes along the profile of latitude 39°. It can be seen that the location of the peak negative signal moves westwards as the fault width increases. When the fault width is fixed, the location of the peak negative signal stays at the same longitude even though the slip magnitude increases. Thus, the location of the minimum value in the seismic gravity changes provides constraints on the width of the fault plane.
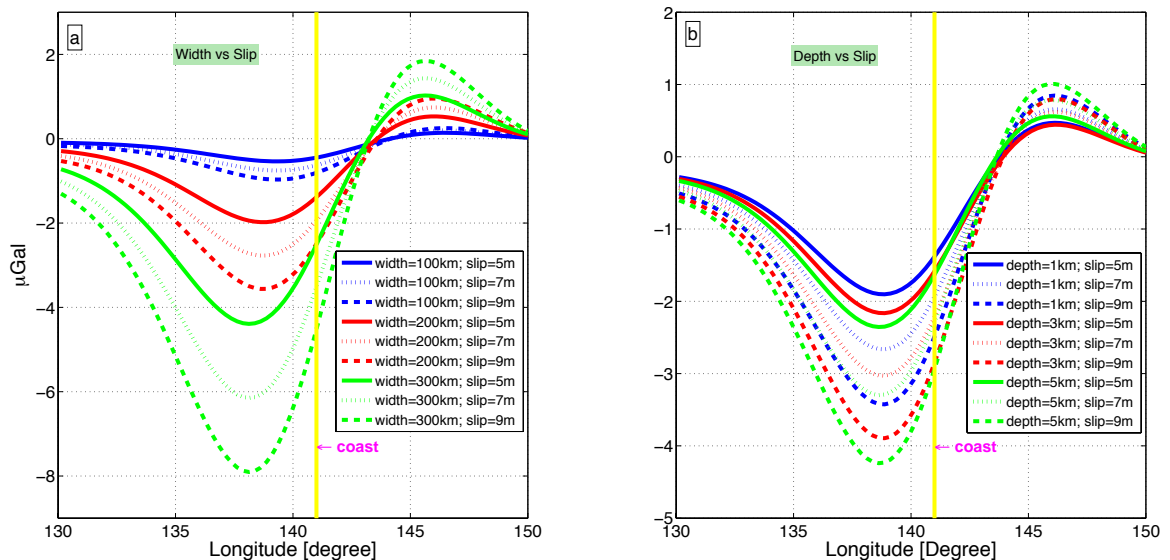
Figure 5.21: The coseismic gravity changes (at spatial resolution of 350km) along the profile across the middle of the fault plane for synthetic faulting scenarios: (**a**) Fault length, depth, dip, strike, rake are fixed at 300km, 1km, 10°, 203°, and 90°, respectively. The width of the fault plane varies from 100km to 300km with step of 100 km, and the uniform slip on the fault plane take values from 5m to 9m for each width. (**b**) Fault-plane length, width, dip, strike and rake are fixed at 300km, 200km, 10°, 203°, and 90°, respectively. The depth of the top edge of the fault varies from 1 km to 5km in steps of 2km, and the uniform slip on the fault plane take values from 5m to 9m for each width. This example shows the sensitivity of coseismic gravity changes to faulting parameters.

93

Figure 5.22 provides a map view to further illustrate the sensitivity of coseismic gravity changes (at GRACE's spatial resolution) to fault width. In Figure 5.22, the fault depth, length and uniform slip are fixed at 1km, 300km and 7m, respectively. The contours at gravity changes of -2μGal are shown for fault widths of 200km, 300km and 400km, respectively. Similarly to the aforementioned conclusion, the location of the peak in negative gravity changes moves westward as fault width increases from 200km to 400km.
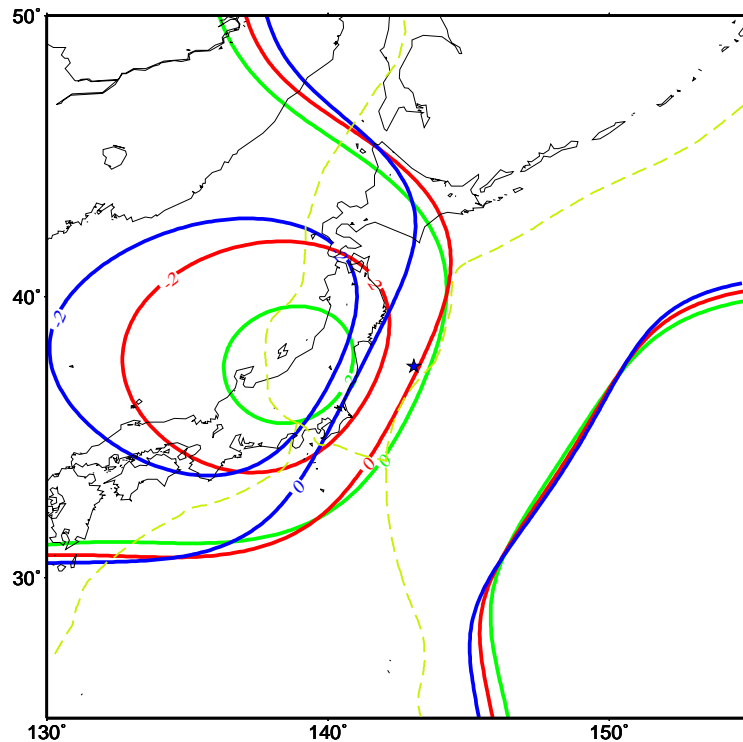
Figure 5.22: The coseismic gravity changes (at GRACE's spatial resolution) generated by faults with different widths. The fault depth, length and uniform slip are fixed as 1km, 300km and 7m, respectively. The contours at gravity changes of -2*μgal* are shown for fault width of 200km(in green), 300km(in red) and 400km(in blue), respectively.

In another example, we test the GRACE's sensitivity to fault depth. Fault length and width are chosen to be 300km and 200km, respectively. The depth of the top edge of the fault varies from 1m to 5m, and the uniform slip takes the values of 5m, 7m and 9m at each depth. From Figure 5.21b, we can see that there is a trade-off in the calculated coseismic gravity changes between fault depth and slip magnitude. For example, along the profile of 39° N, the seismic gravity changes predicted by slip of 7m on a fault at depth of 5km are similar to the gravity changes induced by a slip of 9m on a fault at depth of 1km. Consequently, GRACE data add little constraint to the depth estimation for

94

Tohoku-Oki earthquake. The depth information inverted from other observations should be used if one wants to estimate the other fault parameters using GRACE.

5.3.5 Slip Inversion Using GRACE Observation

We use Simulated Annealing (SA), a nonlinear inversion algorithm (Kirkpatrick *et al*., 1983) to simultaneously invert for the fault width and slip. Although various coseismic models exhibit substantial differences in terms of slip distribution on fault planes, the coseismic gravity changes predicted from them have similar spatial patterns at the spatial resolution commensurate with the GRACE solutions. In other words, GRACE is not able to help discriminate detailed slip distribution for Tohoku-Oki earthquake. Thus, a simplified fault model, i.e., a rectangular fault plane with uniform slip on it, is assumed for inversion. The strike, dip and rake are fixed to be 203°, 10° and 88° respectively, to be consistent with the GCMT solution. Unlike the 2004 Mw 9.1−9.2 Sumatra earthquake and the 2010 Mw 8.8 Maule earthquake, which ruptured segments of more than 1000km and 500km along the subduction zones, respectively, the area of appreciable slip for the Tohoku-Oki earthquake is relatively compact, only about half of the 2010 Maule earthquake (Simons *et al*., 2011). As a result, GRACE observations are less sensitive to the rupture length resulting from the 2011 Tohoku-Oki earthquake. In the inversion, the fault length is fixed to be 240km, which is the average rupture extent in the three coseismic models for the area bearing slips of >10m (~80% of the total moment). It has been suggested that the strong slip of the Tohoku-Oki earthquake is shallow and occupies the concave seaward end in the trench (Ide *et al*., 2011; Lay *et al.,* 2011; Shao *et al.,* 2011). Furthermore, the deformation of the seafloor near the toe of the wedge directly measured by multi-beam bathymetry also provides evidence for the strong up-dip slip all the way to the trench axis (Fujiwara *et al.,* 2011). Therefore, we fixed the fault's top edge at 0 km in the inversion.

The drawback of Simulated Annealing is that the technique does not provide uncertainty estimates for the inversion. In order to take into account the uncertainties in the inversion results caused by GRACE observation errors, the fault parameters are also inverted by using the upper and lower bounds of estimated GRACE observation errors (i.e. *a* posteriori unit-weight variance of 1.62μGal). Finally, the fault width and the uniform slip are estimated as 211±1km and 22.7±2.4m, respectively. Figure 5.23 shows the histograms at convergence in the inversion.
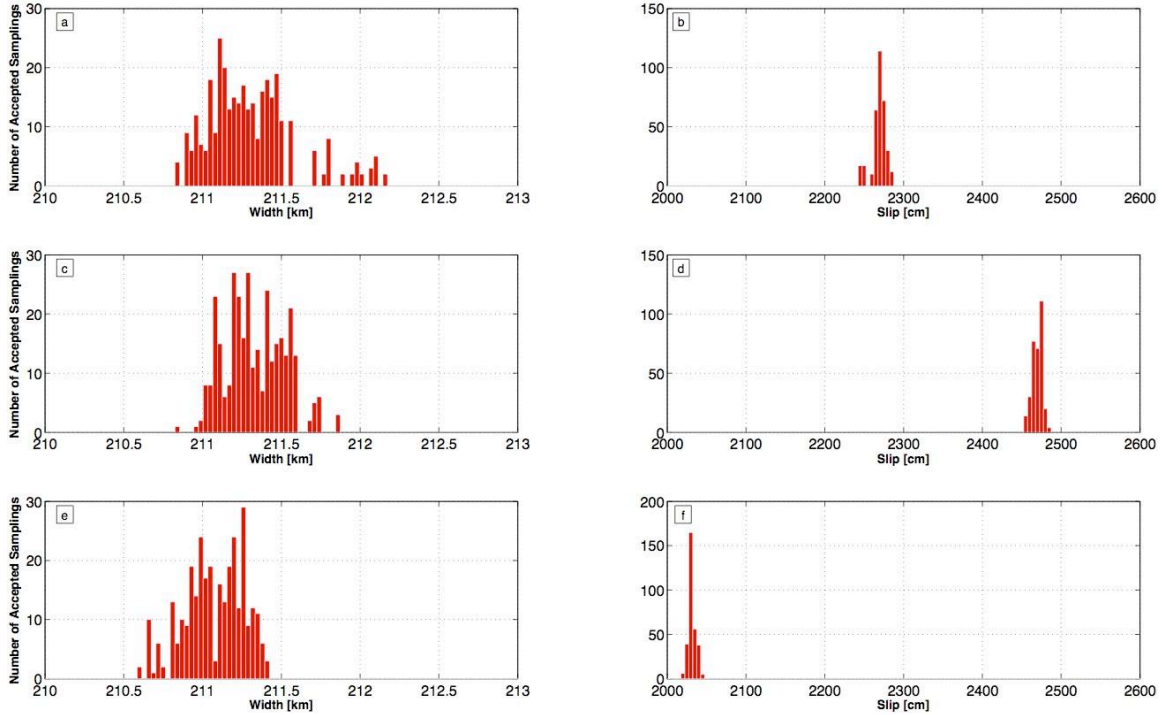
Figure 5.23: Histograms of accepted samplings for variables of fault width and slip in their state spaces when the simulated annealing algorithm converges. (a) and (b): using GRACE detected gravity changes as input; (c) and (d): using the lower bounds of a posteriori error estimates for GRACE observations as input; (e) and (f): using the upper bounds of a posteriori error estimates for GRACE observations as input.

5.3.6 Discussion

Using the estimated values of the total fault width and the uniform slip inverted using GRACE observations (211±1km and 22.7±2.4m, respectively) accounting for both the coseismic and postseismic deformations, and assuming a shear modulus of 40GPa, which is a rough average of the rigidities of upper crust, lower crust and upper mantle in northeastern Japan based on seismic data (Nakajima *et al.,* 2001; Ozawa *et al.,* 2011), the total composite moment is (4.59±0.49) x10^{22} N m, equivalent to a moment magnitude of Mw 9.07±0.65. Our GRACE-inverted model estimate (comprising both coseismic and postseismic slips) is larger than previous estimates, which accounted only for the coseismic moment of the Tohoku-Oki earthquake, i.e., 3.43x10^{22}N m (Ozawa *et al.,* 2011), 4.0x10^{22} N m (Lay *et al.,* 2011), and 3.9x20^{22} N m (Ammon *et al.,* 2011), respectively. If we assume that 3.8x10^{22}N m, as the averaged moment estimate from these studies, is the main shock moment, the post-seismic moment is estimated to be 3.0 x10^{21}−11.7x10^{21} N m, equivalent to a Mw 8.28−8.68 earthquake.

After the main shock, large postseismic deformation, resembling the coseismic displacement, but distributed more broadly (reaching further to the north and south to the

area of coseismic displacement), has been detected by the GPS network (Ozawa *et al.,* 2011). Based on the postseismic displacement measured by GPS, Ozawa *et al.* (2011) found that a large after-slip is distributed in and surrounding the area of the coseismic slip, extending to the north, the south and in the down-dip directions (Figure 5.19d). By using the collected GPS measurement up to March 25, 2011, they estimated the maximum slip of ~1m and moment of the 3.35×10^{21} N m for the after-slip, equivalent to a Mw 8.3 earthquake and very close to the lower bound of the remaining moment (3.0×10^{21} N m) in our estimate. However, this agreement is possibly fortuitous given the uncertainty in the moment estimate of the main shock, the uncertainty range in the GRACE estimate of slip, as well as possible errors in the after-slip model derived based on only far-field GPS measurements. We argue that the effect of the after-slip is indeed a reasonable explanation for the relatively larger amplitude in the gravity changes detected by GRACE. Although the peak gravity change predicted by the model including after-slip during March 11 and March 25 is about –0.8μGal (Figure 5.19h), it should be noticed that, in our GRACE data analysis, the earthquake-induced jump is computed by subtracting the reference field before the earthquake from the mean field after the earthquake, which is the mean GRACE field of April, May and July 2011 (after removing periodic terms). Thus, what sensed by GRACE is the average after-slip during the interval between March 11th and the end of July 2011. By the end of July, the preliminary after-slip model inferred from GEONET data has a maximum slip of ~2.3m and an equivalent moment of Mw 8.5 (http://www.gsi.go.jp/cais/topic110315.2-index-e.html).

As shown by our GRACE sensitivity analysis, the location of the peak in negative gravity changes is diagnostic of the down-dip width of the rupture. The fault width estimate of ~210km in our GRACE observation partially covers the after-slip regions (Figure 5.19d), deeper than the co-seismic area. Additional GRACE data or improved solution after the earthquake will help further constrain the rupture width, as well as the co- and post-seismic moment estimates of the great March 2011 Tohoku-Oki earthquake.

Chapter 6:   Conclusion

The basic causes of earthquakes are stress accumulations resulting from relative plate motions with various patterns such as convergence, divergence, and relative horizontal slide between two plates. Earthquake quantification, which is an important topic in seismology, means to determine several geometric and physical parameters during the rupture, such as location of main shock, rupture area, amplitude of displacement, slip distribution on the fault plane, duration of rupturing, particle velocity at the fault, et cetera. To precisely describe earthquakes helps to understand many natural processes, such as the large scale relative motions of lithospheric plates, properties of Earth's crust and upper mantle, volcanic and tsunami activities and so on. For instance, the map of earthquake distribution identifies the plate boundaries, and thus plays an important role in the development of plate tectonics; faulting patterns can be used to infer the direction of relative motion between plates; and slip amplitude helps to estimate the relative motion rate, re-estimate the seismic moment budget and evaluate the seismic hazard risk.

Teleseismic wave records and geodetic measurements, such as GPS and inSAR, are the most common data types used to constrain fault geometry, displacement amplitude and rupturing history. Unfortunately, intrinsic limitations exist in both techniques. Seismic inversion depends on the estimated velocity structure in which large uncertainties exist. In addition, it is instable to determine the geometry of the fault, particularly when the rupture doesn't break through to the ground surface, thereby the orientation can't be observed directly. Geodetic inversion, which typically uses displacement measurements on land by GPS or InSAR, lacks sensitivity to offshore slips of great earthquakes, which generally occur in subduction zones at ocean trend.

Spaceborne gravimetry provides anther type of geodetic observation for great earthquake studies. Instead of directly measuring the displacement in near-source region, it detects the gravitation changes as the consequence of mass redistribution excited by various faulting processes. This study not only develops new data analysis procedures which prove to be advantageous for extracting co/post-seismic gravitation signals from spaceborne gravimetry observations, but explores a feasible nonlinear inversion scheme to estimate faulting parameters using the detected gravitation changes.

The precondition, for either examining the observation or implementing inversion, is the forward modeling of coseismic gravitation changes. Two approaches, i.e. analytical evaluation and numerical approximation, are developed to model coseismic gravity and gravitational gradient changes under the assumption of a homogeneous elastic half-space. It has been demonstrated by numerical examples that both methods are effective in

calculating the coseismic gravity and gravitational gradient changes triggered by dislocation on a rectangular fault plane. The computation is fast when the analytical method is used, while the effect of layered density structure in the half-space can be taken into account if the numerical approach is adopted.

Different from routine GRACE data processing, the data processing scheme developed in this study is based on spatiospectral localization analysis, which preserves the primitive satellite observation and improves spatial resolution. It is efficient to represent and analyze a regional signal using Slepian function, since local signals are sparse in Slepian domain. Furthermore, the spatial patterns of gravitational potential perturbation owing to earthquakes are similar to those of optimally localized Slepian functions. The Slepian function is thus eminently suitable to analyze the seismic gravitation changes using GRACE observation.

It is a highly nonlinear problem to estimate faulting parameters using GRACE detected coseismic gravity changes. Simulated annealing, which is a Markov Chain Monte Carlo method, is shown to be able to solve inversion problem of high nonlinearity and dimensionality, and it avoids any numerical instabilities due to ill-conditioned matrices. Before inverting for faulting parameters, the sensitivity of GRACE observed gravity changes to various faulting parameters, including fault length, width, depth and average slip, should be tested. Generally, there is a trade-off between the estimates of fault depth and average slip if they are simultaneously inverted. Thus, this study chooses to invert for fault length, width and average slip using GRACE observation. The fault depth, strike and dip are assumed to be known since either GRACE is not sensitive to them or they can be better determined by other observations.

It has been well demonstrated that the GRACE spaceborne gravimetry data are capable of observing coseismic gravity changes resulting from the 26 December 2004 Sumatra-Andaman event (Mw 9.2). This study shows for the first time that refined deformation signals resulting from the Sumatra-Andaman and the 28 March 2005 Nias earthquakes (Mw 8.6) are detectable by processing the GRACE data in terms of the full gravitational gradient tensor. The GRACE-inferred gravitational gradients agree well with coseismic model predictions. Due to the characteristics of these gradients, which have enhanced high-frequency content, the GRACE observations provide a clear delineation of the fault lines, locate significant slips, and better define the extent of the coseismic deformation.

The 27 February 2010 Mw 8.8 Maule (Chile) earthquake ruptured over 500km along a mature seismic gap between 34°S and 38°S – the Concepción-Constitución gap, where no large megathrust earthquakes had occurred since the 1835 Mw ~8.5 event. Notable discrepancies exist in estimated slip distribution and moment magnitude by various models inverted using traditional observations such as teleseismic networks, coastal/river markers, tsunami sensors, Global Positioning System (GPS) and Interferometric Synthetic Aperture Radar (InSAR). This study conducts a spatio-spectral localization analysis, based on Slepian basis functions, of data from GRACE to extract coseismic gravity change signals of the Maule earthquake with improved spatial

resolution (350km half-wavelength). The results reveal discernable differences in the average slip between the GRACE observations and predictions from various coseismic models. Using a simulated annealing algorithm, the fault-plane area and the average slip are simultaneously inverted for. The GRACE-inverted fault plane length and width are 429 ± 6km, 146 ± 5km, respectively. The estimated slip is 8.1 ± 1.2m, indicating most of the strain accumulated since 1835 in the Concepción-Constitución gap had been released by the 2010 Maule earthquake.

GRACE data are processed using spatiospectral localization analysis to detect high-resolution permanent gravity changes due to both coseismic and postseismic deformation associated with the great 11 March 2011 Mw 9.0 Tohoku-Oki earthquake. The GRACE observations are then used in a geophysical inversion to derive a new coseismic slip and after-slip model. The GRACE estimated moment for the total slip, up to the end of July 2011, is $(4.59\pm0.49) \times 10^{22}$ N m, equivalent to a composite Mw of 9.07 ± 0.65. If the moment for the Tohoku-Oki main shock is assumed to be 3.8×10^{22} N m, the contribution from the after-slip is estimated to be $3.0 \times10^{21} \sim 11.7\times10^{21}$ N m, in good agreement with a postseismic slip model inverted from GPS data. Thus, GRACE data provides an independent constraint to quantify co- and post-seismic deformation for the Tohoku-Oki event.

This study demonstrates that spaceborne gravimetry provides an independent and thus valuable constraint on the co-seismic slip for great megathrust events, although the spatial resolution attained by GRACE does not allow for a distinction of the variable slip distribution. However, the detection of the total gravity change produced by coseismic mass redistributions provides a complementary observation to geodetic measurements available on land. Future studies on simultaneous inversion of both data types could further improve the fidelity of coseismic slip models.

Bibliography

Aki, K., and P. G. Richard (2002). *Quantitative Seismology*, 2nd ed, University Science Books, Sausalito, CA.

Ammon, C.J., C. Ji, H. K. Thio, D. Robinson, S. Ni, V. Hjoriefsdottir, H. Kanamori, T. Lay, S. Das, D. Helmberger, G. Ichinoise, J. Poler, and D. Alld (2005). Rupture Process of the 2004 Sumatra-Andaman Earthquake, *Science,* 308, 1133-1139.

Banerjee, P., F. F. Pollitz, and R. Bürgmann (2005). The size and duration of the Sumatra-Andaman earthquake from far-field static offsets, *Science*, 308**,** 1769 –1772.

Beck, S., S. Barrientos, E. Kausel, and M. Reyes (1998). Source characteristics of historic earthquakes along the central Chile subduction zone, *J. S. Am. Earth Sci.,* 11, 115-129.

Ben-Menahem, A. and S. J. Singh (1981). Seismic Waves and Sources, Springer-Verlag, New York.

Broerse, D.B.T., L.L.A. Vermeersen, R.E.M. Riva, and W. van der Wal (2011). Ocean contribution to co-seismic crustal deformation and geoid anomalies: Application to the 2004 December 26 Sumatran-Andaman earthquake, *Earth Planet. Sci. Lett.*, 305, 341-349.

Cambiotti, G., A. Bordoni, R. Sabadini, and L. Colli (2011). GRACE gravity data help constraining seismic models of the 2004 Sumatran earthquake, *J. Geophys. Res.*, 116, B10403.

Campos, J., D. Hatzfeld, R. Madariaga, G. Lopez, E. Kausel, A. Zollo, G. Iannacone, R. Fromm, S. Barrientos, and H. Lyon-Caen (2002). A seismological study of the 1835 seismic gap in south-central Chile, *Phys. Earth Planet. Int.,* 132, 177-195.

Chen, J.L., C.R. Wilson, B. D. Tapley, and S. Grand (2007). GRACE detects coseismic and postseismic deformation from the Sumatra-Andaman earthquake, *Geophys. Res. Letts.,* 34, L13302.

Chlieh, M., J. P. Avouac, V. Hjorleifsdottir, T. R. A. Song, C. Ji, K. Sieh, A. Sladen, H. Hebert, L. Prawirodirdjo, Y. Bock, and J. Galetzka (2007). Coseismic slip and afterslip of the great M-w 9.15 Sumatra-Andaman earthquake of 2004, *Bull. Seismol. Soc. Am.*, 97, S152-S173.

Darwin, C. (1845). Journal of the Researches into the Natural History and Geology of the Countries Visited During the Voyage of the HMS Beagle Round the World, 2nd ed., John Murray.

De Linage, C., L. Rivera, J. Hinderer, J. P. Boy, Y. Rogister, S. Lambotte, and R. Biancale (2009). Separation of coseismic and postseismic gravity changes for the 2004 Sumatran earthquake from 4.6 yr of GRACE observations and modelling of the coseismic change by normal mode summation, *Geophys. J. Int.,* 176, 695–714.

Delouis, B., J. –M Nocquet, and M. Vallée (2010). Slip distribution of the February 27, 2010 Mw = 8.8 Maule Earthquake, central Chile, from static and high-rate GPS, InSAR, and broadband teleseismic data, *Geophys. Res. Lett.,* 37, L17305.

DeMets, C., R. G. Gordon, D. F. Argus, and S. Stein (1990). Current plate motions, *Geophys. J. Int., 101*, 425–478.

Drinkwater, M., R. Haagmans, M. Kern, D. Muzi, and R. Floberghagen (2008). GOCE: Obtaining a Portrait of Earth's Most Intimate Features, European Space Agency (ESA) Bulletin 133.

Duan, X., J. Guo, C. K. Shum, and W. van der Wal (2009). On the postprocessing removal of correlated errors in GRACE temporal gravity field solutions, *J. Geod.,* 83, 1095–1106.

Farías, M., G. Vargas, A. Tassara, S. Carretier, S. Baize, D. Melnick, and K. Bataille (2010). Land-level changes produced by the M_w 8.8 2010 Chilean Earthquake, *Science*, 329, 916.

Finite fault model, U.S. Geological Survey (USGS), 2010. http://earthquake.usgs.gov/earthquakes/eqinthenews/2010/us2010tfan/finite_fault.php

Fujiwara, T., S. Kodaira, T. No, Y. Kaiho, N. Takahashi, and Y. Kaneda (2011). The 2011 Tohoku-Oki Earthquake: Displacement Reaching the Trench Axis, *Science,* 334, 1240.

Gahalaut, V. K., B. Nagarajan, J. K. Catherine, and S. Kumar (2006). Constraints on 2004 Sumatra-Andaman earthquake rupture from GPS measurements in Andaman-Nicobar Islands, *Earth Planet. Sci. Lett.,* 242**,** 365 –374.

Global Centroid-Moment-Tensor (CMT) project, 2011. http://www.globalcmt.org

Han, S. C., C. K. Shum, C. Jekeli, C. Y. Kuo, C. Wilson, and K. Seo (2005). Non-isotropic filtering of GRACE temporal gravity for geophysical signal enhancement, *Geophys. J. Int*., 163, 18-25.

Han, S. C., C. K. Shum, M. Bevis, C. Ji, and C. Y. Kuo (2006). Crustal dilatation

observed by GRACE after the 2004 Sumatra-Andaman earthquake, *Science*, 313, 658-661.

Han, S.C., J. Sauber, S. B. Luthcke, C. Ji, and F. F. Pollitz (2008). Implications of postseismic gravity change following the great 2004 Sumatra-Andaman earthquake from the regional harmonic analysis of GRACE intersatellite tracking data, *J. Geophys. Res*., 113, B11413.

Han, S.C., J. Sauber, and S. Luthcke (2010). Regional gravity decrease after the 2010 Maule (Chile) earthquake indicates large-scale mass redistribution, *Geophys. Res. Lett*., 37, L23307.

Heki, K. and K. Matsuo (2010). Coseismic gravity changes of the 2010 earthquake in central Chile from satellite gravimetry, *Geophys. Res. Lett*., 37, L24306.

Ide, S., A. Baltay, and G. C. Beroza (2011). Shallow dynamic overshoot and energetic deep rupture in the 2011 *Mw* 9.0 Tohoku-Oki earthquake, *Science,* 332**,** 1426–1429.

Iinuma, T., M. Ohzono, Y. Ohta, and S. Miura (2011). Coseismic slip distribution of the 2011 off the Pacific coast of Tohoku earthquake (M9.0) estimated based on GPS data- Was the asperity in Miyagi-oki ruptured?, *Earth Planets Space*, in press

Jade, J., M. B. Ananda, P. Dileep Kumar, and S. Banerjee (2005). Co- seismic and post- seismic displacements in Andaman and Nicobar Islands from GPS measurements, *Curr. Sci.*, 88 **,**1980 –1984.

Jekeli, C. (1981). Alternative methods to smooth the Earth's gravity field, *Rep.* 327, Dep. of Geod. Sci. and Surv., Ohio State Univ., Columbus, Ohio.

Jekeli, C. (2003). Formulas for the gravitational gradient due to a rectangular block, *Ohio State University*.

Khazaradze, G. and J. Klotz (2003). Short and Long-term effects of GPS measured crustal deformation rates along the South-Central Andes, *J. Geophys. Res.,* 108 (B4), 1-13.

Kirkpatrick, S., C. D. Jr. Gelatt, and M. P. Vecchi (1983). Optimization by simulated annealing, *Science*, 220, 671-680.

Klees, R., E. A. Revtova, B. C. Gunter, P. Ditmar, E. Oudman, H. C. Winsemius, and H. H. G. Savenije (2008). The design of an optimal filter for monthly GRACE gravity models, *Geophys. J. Int.,* 175, 417-432.

Kusche, J. (2007). Approximate decorrelation and non-isotropic smoothing of time-variable GRACE-type gravity field models, *J. Geod.,* 81, 733-749.

Lay, T. (2011). A Chilean surprise, *Nature*, 471, 174-175.

Lay, T., C. J. Ammon, H. Kanamori, K. D. Koper, O. Sufri, and A. R. Hutko (2010). Teleseismic inversion for rupture process of the 27 February 2010 Chile (Mw 8.8) earthquake, *Geophys. Res. Lett.,* 37, L13301.

Lay, T., C. J. Ammon, H. Kanamori, L. Xue, and M. J. Kim (2011). Possible large near-trench slip during the 2011 *Mw* 9.0 off the Pacific coast of Tohoku Earthquake, *Earth Planets Space,* 63, 687–692.

Lay, T., H. Kanamori, C. Ammon, M. Nettles, S. Ward, R. Aster, S. Beck, S. Bilek, M. Brudzinski, R. Butler, H. Deshon, G. Ekstrom, K. Satake, and S. Sipkin (2005). The Great Sumatra-Andaman Earthquake of 26 December 2004, *Science*, 308, 1127.

Lorito, S., F. Romano, S. Atzori, X. Tong, A. Avallone, J. McCloskey, M. Cocco, E. Boschi, and A. Piatanesi (2011). Limited overlap between the seismic gap and coseismic slip of the great 2010 Chile earthquake, *Nature Geoscience*, 4, 173-177.

Lay, T. and T. C. Wallace (1995). Modern global seismology, Academic Press, San Diego, CA.

Loveless, J. P. and B. J. Meade (2011). Spatial correlation of interseismic coupling and coseismic rupture extent of the 2011 Mw = 9.0 Tohoku-oki eqrthquake, *Geophys. Res. Lett.,* 38, L17306.

Massonnet, D. and K. L. Feigl (1998). Radar interferometry and its application to changes in the earth's surface, *Rev. Geophys.*, 36(4), 441 – 500.

Matsuo, K. and K. Heki (2011). Coseismic gravity changes of the 2011 Tohoku-Oki earthquake from satellite gravimetry, *Geophys. Res. Lett*., 38, L00G12.

Mindli, R. D., and D. H. Cheng (1950). Nuclei of strain in the semi-infinite solid, *J. appl. Phys.*, 21, 926-930.

Minoura, K., F. Imamura, D. Sugawara, Y. Kono, and T. Iwashita (2001). The 869 Jogan tsunami deposit and recurrence interval of large-scale tsunami on the Pacific coast of northeast Japan, *J. Natural Disaster Sci.,* 23, 83-88.

Moreno, M. S., J. Klotz, D. Melnick, H. Echtler, and K. Bataille (2008). Active faulting and heterogeneous deformation across a megathrust segment boundary from GPS data, south central Chile (36-39°S), *Geochem. Geophys. Geosyst.,* 9, Q12024.

Moreno, M., M. Rosenau, and O. Oncken (2010). 2010 Maule earthquake slip correlates with pre-seismic locking of Andean subduction zone, *Nature*, 467**,** 198–202.

Nakajima, J., T. Matsuzawa, A. Hasegawa, and D. Zhao (2001). Seismic imaging of arc magma and fluids under the central part of northeastern Japan, *Tectonophysics,* 341, 1-17.

Nishenko, S.P. (1985). Seismic potential for large and great interplate earthquakes along the Chilean and Southern Peruvian Margins of South America: A quantitative reappraisal, *J. Geophys. Res.,* 90, 3589-3615.

Ogawa, R. and K. Heki (2007). Slow postseismic recovery of geoid depression formed by the 2004 Sumatra-Andaman Earthquake by mantle water diffusion, *Geophys. Res. Lett.*, 34, L06313.

Okada, Y. (1985). Surface deformation due to shear and tensile faults in a half-space, *Bull. Seism. Soc. Am.,* 75, 1135-1154.

Okubo, S. (1991). Potential and gravity changes raised by point dislocations, *Geophys. J. Int.,* 105, 573-586.

Okubo, S. (1992). Gravity and potential changes due to shear and tensile faults in a half-space, *J. Geophys. Res.*, 97(B5), 7137–7144.

Ozawa, S., T. Nishimura, H. Suito, T. Kobayashi, M. Tobita, and T. Imakiire (2011). Coseismic and postseismic slip of the 2011 magnitude-9 Tohoku- Oki earthquake, *Nature,* 475, 373-376.

Panet, I., V. Mikhailov, M. Diament, F. Pollitz, G. King, O. de Viron, M. Holschneider, R. Biancale, and J. M. Lemoine (2007). Coseismic and post-seismic signatures of the Sumatra 2004 December and 2005 March earthquakes in GRACE satellite gravity, *Geophys. J. Int*., 171, 177-190.

Perfettini, H., J. P. Avouac, H. Travera, A. Kositsy, J. M. Nocquet, F. Bondoux, M. Chlieh, A. Sladen, L. Audin, D. L. Farber, and P. Soler (2010). Seismic and aseismic slip on the Central Peru megathrust, *Nature*, 465, 78-81.

Pincus, M. (1970). A Monte Carlo method for the approximate solution of certain types of constrained optimization problems, *Oper. Res*., 18, 1225-1228.

Pollitz, F. F., B. Brooks, X. Tong, M. Bevis, J. Foster, R. Bürgmann, R. Smalley, Jr., C. Vigny, A. Socquet, J. -C Ruegg, J. Campos, S. Barrientos, H. Parra, J. C. B. Soto, S. Cimbaro, and M. Blanco (2011). Coseismic slip distribution of the February 27, 2010 Mw 8.8 Maule, Chile earthquake, *Geophys. Res. Lett.*, 38, L09309.

Pollitz, F. F., R. Bürgmann, and P. Banerjee (2006). Post-seismic relaxation following the great 2004 Sumatra-Andaman earthquake on a compressible self-gravitating Earth, *Geophys. J. Int*., 167, 397–420.

Pollitz, F. F., R. Bürgmann, and P. Banerjee (2011). Geodetic slip model of the 2011 M9.0 Tohoku earthquake, *Geophys. Res. Lett.,* 38, L00G08.

Press, F. (1965). Displacements, strains, and tilts at telesesmic distances, *J. Geophys. Res.,* 70, 1135-2412.

Ruegg, J. C., J. Campos, R. Madariaga, E. Kausel, E., J. B. de Chabalier, R. Armijo, D. Dimitrov, I. Georgiev, and S. Barrientos (2002). Interseismic strain accumulation in south central Chile from GPS measurements, 1996-1999, *Geophys. Res. Lett.,* 29, 1517-1520.

Ruegg, J. C., A. Rudloff, C. Vigny, R. Madariaga, J. B. de Chabalier, J. Campos, E. Kausel, S. Barrientos, and D. Dimitrov (2009). Interseismic strain accumulation measured by GPS in the seismic gap between Constitución and Concepción in Chile, *Phys. Earth Planet. Int.,* 175, 78-85.

Sambridge, M. and K. Mosegaard (2002). Monte Carlo methods in geophysical inverse problems, *Rev. Geophys.*, 40(3), 1009.

Sandwell, D. (1982). Poisson's Equation in Cartesian Coordinates, http://topex.ucsd.edu/geodynamics/15gravity2_2.pdf

Sato, M., T. Ishikawa, N. Ujihara, S. Yoshida, M. Fujita, M. Mochizuki, and A. Asada (2011). Displacement above the hypocenter of the 2011 Tohoku-oki earthquake, *Science,* 332, 1395.

Segall, P. and J.L. Davis (1997). GPS applications for geodynamics and earthquake studies, *Annual Reviews of Earth and Planetary Science*, 25, 301-336.

Shao, G., X. Li, C. Ji, and T. Maeda (2011). Focal mechanism and slip history of the 2011 Mw 9.1 off the Pacific coast of Tohoku earthquake, constrained with teleseismic body and surface waves, *Earth Planets Space*, 63, 559–564.

Simons, F. J., F. A. Dahlen, and M. A. Wieczorek (2006). Spatiospectral concentration on a sphere, *SIAM Rev.*, 48(3), 504-536.

Simons, F. J., J. C. Hawthorne, and C. D. Beggan (2009). Efficient analysis and representation of geophysical processes using localized spherical basis functions, *Proc. SPIE*, 7446.

Simons, M., S. E. Minson, A. Sladen, F. Ortega, J. Jiang, S. E. Owen, L. Meng, J.-P. Ampuero, S. Wei, R. Chu, D. V. Helmberger, H. Kanamori, E. Hetland, A. W. Moore, and F. H. Webb (2011). The 2011 magnitude 9.0 Tohoku-Oki earthquake: Mosaicking the megathrust from seconds to centuries, *Science*, 332,1421-1425.

Steketee, J. A. (1958). Some geophysical applications of the elasticity theory of dislocations, *Can. J. Phys.*, 36, 1168–1198.

Subarya, C., M. Chlieh, L. Prawirodirdjo, J. P. Avouac, Y. Bock, K. Sieh, A. J. Meltzner, D. H. Natawidjaja, and R. McCaffrey (2006). Plate- boundary deformation associated with the great Sumatra-Andaman earthquake, *Nature*, 440**,** 46 –51.

Sun, W. and S. Okubo (1998). Surface potential and gravity changes due to internal dislocations in a spherical earth—II. Application to a finite fault, *Geophys. J. Int.,* 132, 79–88.

Swenson, S. and Wahr, J. (2006). Post-processing removal of correlated errors in GRACE data, *Geophys. Res. Lett*., 33, L08402.

Tapley, B., S. Bettadpur, J. Ries, P. Thompson, and M. Watkins (2004). GRACE measurements of mass variability in the Earth system, *Science,* 305, 503-505.

Tong, X., D. Sandwell, K. Luttrell, B. Brooks, M. Bevis, M. Shimada, J. Foster, R. Smalley Jr., H. Parra, J. C. B. Soto, M. Blanco, E. Kendrick, J. Genrich, and D. J. Caccamise II (2010). The 2010 Maule, Chile earthquake: Downdip rupture limit revealed by space geodesy, *Geophys. Res. Lett.,* 37, L24311.

Vigny, C., A. Socquet, S. Peyrat, J.-C. Ruegg, M. Métois, R. Madariaga, S. Morvan, M. Lancieri, R. Lacassin, J. Campos, D. Carrizo, M. Bejar-Pizarro, S. Barrientos, R. Armijo, C. Aranda, M.-C. Valderas-Bermejo, I. Ortega, F. Bondoux, S. Baize, H. Lyon-Caen, A. Pavez, J. P. Vilotte, M. Bevis, B. Brooks, R. Smalley, H. Parra, J.-C. Baez, M. Blanco, S. Cimbaro, and E. Kendrick (2011). The 2010 Mw 8.8 Maule Megathrust Earthquake of Central Chile, Monitored by GPS, *Science*, 332, 1417-1421.

Vigny, C., W. J. F. Simons, S. Abu, R. Bamphenyu, C. Satirapod, N. Choosakul, C. Subarya, A. Socquet, K. Omar, H. Z. Abidin, and B. A. C. Ambrosius (2005). Insight into the 2004 Sumatra-Andaman earthquake from GPS measurements in southeast Asia, *Nature*, 436**,** 201 – 206.

Wahr, J., F. Molenaar, and F. Bryan (1998). Time variability of the Earth's gravity field: hydrological and oceanic effects and their possible detection using GRACE, *J. Geophys. Res*., 103(B12), 30205-30229.

Wang, L., C. K. Shum, F. J. Simons, A. Tassara, K. Erkan, C. Jekeli, A. Braun, C. Y. Kuo, H. Lee, and D. Y. Yuan (2012a). Coseismic slip of the 2010 Mw 8.8 Great Maule, Chile Earthquake quantified by GRACE observation, *Earth & Planet. Sci. Lett.,* in revision.

Wang, L., C. K. Shum, F. J. Simons, B. Tapley, and C. Dai (2012b). Coseismic and postseismic deformation of the 2011 Tohoku-Oki earthquake constrained by GRACE

gravimetry, *Geophys. Res. Lett.,* accepted.

Wang, L., C. K. Shum, and C. Jekeli (2012c). Gravitational gradient changes following the Summatra-Andaman earthquake inferred from GRACE, *Geophys. J. Int.*, in revision.

Wieczorek, M. A. and F. J. Simons (2005). Localized spectral analysis on the sphere, *Geophys. J. Int.*, 162, 655-675.

Appendix A: Galerkin Vector

$$\vec{\Gamma}^{(1)}\left(\vec{r},\vec{\xi}\right) = \begin{pmatrix} R+Q-\dfrac{2\xi_3^2}{Q}+4(1-v)(1-2v)\left[(x_3+\xi_3)\log(Q+x_3+\xi_3)-Q\right] \\ 0 \\ \dfrac{2\xi_3(x_1-\xi_1)}{Q}+2(1-2v)(x_1-\xi_1)\log(Q+x_3+\xi_3) \end{pmatrix} \tag{A.1}$$

$$\vec{\Gamma}^{(2)}\left(\vec{r},\vec{\xi}\right) = \begin{pmatrix} 0 \\ R+Q-\dfrac{2\xi_3^2}{Q}+4(1-v)(1-2v)\left[(x_3+\xi_3)\log(Q+x_3+\xi_3)-Q\right] \\ \dfrac{2\xi_3(x_1-\xi_1)}{Q}+2(1-2v)(x_2-\xi_2)\log(Q+x_3+\xi_3) \end{pmatrix} \tag{A.2}$$

$$\vec{\Gamma}^{(3)}\left(\vec{r},\vec{\xi}\right) = \begin{pmatrix} 0 \\ 0 \\ R+\left[8v(1-v)-1\right]Q+4(1-2v)\left[(1-v)x_3-v\xi_3\right]\log(Q+x_3+\xi_3)-\dfrac{2\xi_3 x_3}{Q} \end{pmatrix} \tag{A.3}$$

where

$$R = \sqrt{(x_1-\xi_1)^2+(x_2-\xi_2)^2+(x_3-\xi_3)^2} \tag{A.4}$$

$$Q = \sqrt{(x_1-\xi_1)^2+(x_2-\xi_2)^2+(x_3+\xi_3)^2} \tag{A.5}$$

109

Appendix B: Gravitational Potential Change Caused by Point Dislocation

Gravitational potential change due to density change:

$$\psi^{(11)}\left(\vec{r},\xi_3\right) = G\rho(1-2v)\left[-\frac{1}{R}+\frac{1}{R+\xi_3-x_3}-\frac{x_1^2}{R\left(R+\xi_3-x_3\right)^2}\right]+\frac{G\rho}{R} \tag{B.1}$$

$$\psi^{(33)}\left(\vec{r},\xi_3\right) = \frac{G\rho}{R} \tag{B.2}$$

$$\psi^{(12)}\left(\vec{r},\xi_3\right) = -G\rho(1-2v)\frac{x_1 x_2}{R\left(R+\xi_3-x_3\right)^2} \tag{B.3}$$

$$\psi^{(13)}\left(\vec{r},\xi_3\right) = 0 \tag{B.4}$$

Gravitational potential change due to surface vertical deformation:

$$\phi^{(11)}\left(\vec{r};\xi_3\right) = -G\rho\left\{\frac{1}{\hat{R}}-\frac{\xi_3}{\hat{R}\left(\hat{R}+\xi_3+|x_3|\right)}+\frac{\xi_3 x_1^2\left(2\hat{R}+\xi_3+|x_3|\right)}{\hat{R}^3\left(\hat{R}+\xi_3+|x_3|\right)^2}\right.$$
$$\left.-(1-2v)\left[\frac{x_1^2}{\hat{R}\left(\hat{R}+\xi_3+|x_3|\right)^2}+\frac{\xi_3+|x_3|}{\hat{R}\left(\hat{R}+\xi_3+|x_3|\right)}\right]\right\} \tag{B.5}$$

$$\phi^{(33)}\left(\vec{r};\xi_3\right) = -G\rho\left[\frac{1}{\hat{R}}+\frac{\xi_3\left(\xi_3+|x_3|\right)}{\hat{R}^3}\right] \tag{B.6}$$

$$\phi^{(12)}\left(\vec{r};\xi_3\right) = -G\rho\left[\frac{\xi_3 x_1 x_2\left(2\hat{R}+\xi_3+|x_3|\right)}{\hat{R}^3\left(\hat{R}+\xi_3+|x_3|\right)^2}-(1-2v)\frac{x_1 x_2}{\hat{R}\left(\hat{R}+\xi_3+|x_3|\right)^2}\right] \tag{B.7}$$

$$\phi^{(13)}\left(\vec{r};\xi_3\right) = G\rho\frac{\xi_3 x_1}{\hat{R}^3} \tag{B.8}$$

where

$$\hat{R} \equiv \sqrt{x_1^2+x_2^2+\left(x_3-\xi_3\right)^2} \tag{B.9}$$

Total gravitational potential change:

$$\Psi^{(11)}\left(\bar{r};\xi_3\right) = G\rho\xi_3 \left[\frac{1}{R\left(R+\xi_3-x_3\right)} - \frac{x_1^2\left(2R+\xi_3-x_3\right)}{R^3\left(R+\xi_3-x_3\right)^2} \right] \tag{B.10}$$

$$\Psi^{(33)}\left(\bar{r};\xi_3\right) = G\rho\frac{\xi_3\left(x_3-\xi_3\right)}{R^3} \tag{B.11}$$

$$\Psi^{(12)}\left(\bar{r};\xi_3\right) = -G\rho\frac{\xi_3 x_1 x_2\left(2R+\xi_3-x_3\right)}{R^3\left(R+\xi_3-x_3\right)^2} \tag{B.12}$$

$$\Psi^{(13)}\left(\bar{r};\xi_3\right) = G\rho\frac{\xi_3 x_1}{R^3} \tag{B.13}$$

Appendix C: Gravitational Potential Change Caused by Fault

Total potential change

$$\Delta\Psi(x_1, x_2, x_3) = \left\{ G\rho\left[U_1 S(\xi, \eta) + U_2 D(\xi, \eta) + U_3 T(\xi, \eta)\right] + G\Delta\rho U_3 C(\xi, \eta) \right\} \Big\| \tag{C.1}$$

where

$$\Delta\rho = \rho' - \rho \tag{C.2}$$

S, D, T and *C* denote the contributions from strike-slip, dip-slip, tensile components and intrusions into the cavity formed due to tensile opening, respectively.

If $\cos\delta \neq 0$:

$$S(\xi, \eta) = -q_0 I_0 \sec^2\delta + R\tan\delta + 2\xi I_1 \tan^2\delta \tag{C.3}$$

$$D(\xi, \eta) = -\xi I_0 \tan\delta - 2x_3 I_2 \sin\delta - q_0\left[\log(R+\xi) + 2I_1\tan\delta\right] \tag{C.4}$$

$$C(\xi, \eta) = -\xi\log(R+\eta) - \eta\log(R+\xi) - 2qI_2 \tag{C.5}$$

$$T(\xi, \eta) = \xi I_0 \tan^2\delta - x_3\sin\delta\log(R+\xi) + 2q_0\left(I_1\tan^2\delta + I_2\right) + C(\xi, \eta) \tag{C.6}$$

where

$$I_0(\xi, \eta) = \log(R+\eta) - \sin\delta\log(R+\bar{d}) \tag{C.7}$$

$$I_1(\xi, \eta) = \tan^{-1}\left(\frac{-q\cos\delta + (1+\sin\delta)(R+\eta)}{\xi\cos\delta}\right) \tag{C.8}$$

$$I_2(\xi, \eta) = \tan^{-1}\left(\frac{R+\xi+\eta}{q}\right) \tag{C.9}$$

$$R = \sqrt{\xi^2 + \eta^2 + q^2} \tag{C.10}$$

$$q = x_2\sin\delta - (d - x_3)\cos\delta \tag{C.11}$$

$$q_0 = q - x_3\cos\delta \tag{C.12}$$

$$\bar{d} = \eta\sin\delta - q\cos\delta \tag{C.13}$$

If $\cos\delta = 0$:

$$S(\xi, \eta) = \frac{q\sin\delta}{2}\left[\frac{2x_3 + \eta\sin\delta}{R+\bar{d}} - 2\sin\delta\log(R+\eta) + \log(R+\bar{d})\right] \tag{C.14}$$

$$D(\xi, \eta) = -q_0\log(R+\xi) - 2\sin\delta x_3 I_2 \tag{C.15}$$

$$T(\xi, \eta) = C(\xi, \eta) + 2q_0 I_2 + \frac{\xi(2x_3\sin\delta + \eta)}{2(R+\bar{d})} + \frac{\sin\delta}{2}\left[-2x_3\log(R+\xi) + \xi\log(R+\bar{d})\right]$$

$$\text{(C.16)}$$

Potential Change From Expansion/Contraction and Cavity-filling Materials

$$\Delta\psi\left(x_1, x_2, x_3\right) = \left\{G\Delta\rho U_3 C^*\left(\xi,\eta\right) + G\rho\left[U_1 S^*\left(\xi,\eta\right) + U_2 D^*\left(\xi,\eta\right) + U_3 T^*\left(\xi,\eta\right)\right]\right\}\Big\|$$

$$\text{(C.17)}$$

where
If $\cos\delta \neq 0$:

$$S^*\left(\xi,\eta\right) = \left(1-2v\right)\tan\delta\left\{-R - 2\xi I_1 \tan\delta + q\sec\delta\left[\sin\delta\log\left(R+\eta\right) - \log\left(R+\overline{d}\right)\right]\right\}$$

$$\text{(C.18)}$$

$$D^*\left(\xi,\eta\right) = \left(1-2v\right)I_3 \sin\delta\cos\delta \tag{C.19}$$

$$T^*\left(\xi,\eta\right) = -\left(1-2v\right)I_3 \sin^2\delta \tag{C.20}$$

$$C^*\left(\xi,\eta\right) = C\left(\xi,\eta\right) \tag{C.21}$$

$$I_3\left(\xi,\eta\right) = \left(\xi I_0 + 2q I_1\right)\sec^2\delta \tag{C.22}$$

If $\cos\delta = 0$:

$$S^*\left(\xi,\eta\right) = -\left(1-2v\right)\frac{q\sin\delta}{2}\left[\log\left(R+\overline{d}\right) + \frac{\overline{d}}{R+\overline{d}}\right] \tag{C.23}$$

$$D^*\left(\xi,\eta\right) = 0 \tag{C.24}$$

$$T^*\left(\xi,\eta\right) = -\left(1-2v\right)\frac{\xi\sin\delta}{2}\left[\log\left(R+\overline{d}\right) + \frac{\overline{d}}{R+\overline{d}}\right] \tag{C.25}$$

Appendix D: Vertical Deformation and Gravity Change Caused by Fault

Vertical deformation:

$$\Delta h\left(x_1, x_2, 0\right) = \frac{1}{2\pi}\left[U_1 S_h\left(\xi, \eta\right) + U_2 D_h\left(\xi, \eta\right) + U_3 T_h\left(\xi, \eta\right)\right]\Big\|$$ (D.1)

where

$$S_h\left(\xi, \eta\right) = -\frac{\overline{d}q}{R\left(R+\eta\right)} - \frac{q\sin\delta}{R+\eta} - I_4 \sin\delta$$ (D.2)

$$D_h\left(\xi, \eta\right) = -\frac{\overline{d}q}{R\left(R+\xi\right)} - \sin\delta\tan^{-1}\left(\frac{\xi\eta}{qR}\right) + I_5 \sin\delta\cos\delta$$ (D.3)

$$T_h\left(\xi, \eta\right) = \frac{\overline{y}q}{R\left(R+\xi\right)} + \cos\delta\left[\frac{\xi q}{R\left(R+\eta\right)} - \tan^{-1}\left(\frac{\xi\eta}{qR}\right)\right] - I_5 \sin^2\delta$$ (D.4)

and

$$\overline{d} = \eta\sin\delta - q\cos\delta$$ (D.5)

$$\overline{y} = \eta\cos\delta + q\sin\delta$$ (D.6)

$$I_4\left(\xi, \eta\right) = \left(1-2v\right)\left[\log\left(R+\overline{d}\right) - \sin\delta\log\left(R+\eta\right)\right]\sec\delta$$ (D.7)

$$I_5\left(\xi, \eta\right) = 2\left(1-2v\right)I_1 \sec\delta$$ (D.8)

If $\cos\delta = 0$

$$I_4\left(\xi, \eta\right) = -\left(1-2v\right)\frac{q}{R+\overline{d}}$$ (D.9)

$$I_5\left(\xi, \eta\right) = -\left(1-2v\right)\frac{\xi\sin\delta}{R+\overline{d}}$$ (D.10)

Total gravity change:

$$S_g\left(\xi, \eta\right) = -\frac{q\sin\delta}{R} + \frac{q^2\cos\delta}{R\left(R+\eta\right)}$$ (D.11)

$$D_g\left(\xi, \eta\right) = 2I_2 \sin\delta - \frac{q\overline{d}}{R\left(R+\xi\right)}$$ (D.12)

$$T_g\left(\xi, \eta\right) = 2I_2 \cos\delta + \frac{q\overline{y}}{R\left(R+\xi\right)} + \frac{q\xi\cos\delta}{R\left(R+\eta\right)}$$ (D.13)

$$C_g\left(\xi, \eta\right) = 2I_2 \cos\delta - \sin\delta\log\left(R+\xi\right)$$ (D.14)

115

Gravity change due to density change:

$$S_g^*(\xi,\eta) = I_4 \sin\delta \qquad \text{(D.15)}$$

$$D_g^*(\xi,\eta) = -I_5 \sin\delta\cos\delta \qquad \text{(D.16)}$$

$$T_g^*(\xi,\eta) = I_5 \sin^2\delta \qquad \text{(D.17)}$$

$$C_g^*(\xi,\eta) = C_g(\xi,\eta) \qquad \text{(D.18)}$$

If $\cos\delta = 0$, equations (D.9) and (D.10) are used for I_4 and I_5.

Appendix E: Gravitational Gradient Change Caused by Fault

$$S_{12}(\xi,\eta) = -\sin\delta\sec^2\delta\frac{\partial I_0}{\partial x_1} - (q\sec\delta - x_3)\sec\delta\frac{\partial^2 I_0}{\partial x_1\partial x_2} + 2\tan^2\delta\frac{\partial I_1}{\partial x_2} + 2\xi\tan^2\delta\frac{\partial^2 I_1}{\partial x_1\partial x_2} - \frac{\overline{y}\xi\tan\delta}{R^3}$$

(E.1)

$$D_{12}(\xi,\eta) = -\tan\delta\frac{\partial I_0}{\partial x_2} - \xi\tan\delta\frac{\partial^2 I_0}{\partial x_1\partial x_2} - 2\sin\delta\tan\delta\frac{\partial I_1}{\partial x_1} - 2q\tan\delta\frac{\partial^2 I_1}{\partial x_1\partial x_2} - \frac{\sin\delta}{R} + \frac{\overline{y}q}{R^3}$$

(E.2)

$$T_{12}(\xi,\eta) = \tan^2\delta\left(\frac{\partial I_0}{\partial x_2} + \xi\frac{\partial^2 I_0}{\partial x_1\partial x_2}\right) + 2\tan^2\delta\left(\sin\delta\frac{\partial I_1}{\partial x_1} + q\frac{\partial^2 I_1}{\partial x_1\partial x_2}\right) + 2\left(\sin\delta\frac{\partial I_2}{\partial x_1} + q\frac{\partial^2 I_2}{\partial x_1\partial x_2}\right) + C_{12}(\xi,\eta)$$

(E.3)

$$C_{12}(\xi,\eta) = -\frac{\cos\delta}{R} - \frac{q\sin\delta}{R(R+\eta)}$$

(E.4)

$$S_{13}(\xi,\eta) = -\frac{\xi q\sin\delta}{R^3} + \frac{\xi q^2(2R+\eta)\cos\delta}{R^3(R+\eta)^2}$$

(E.5)

$$D_{13}(\xi,\eta) = -\frac{q\overline{d}}{R^3} - \frac{q\sin\delta}{R(R+\eta)}$$

(E.6)

$$T_{13}(\xi,\eta) = \frac{q\overline{y}}{R^3} - \frac{2q\cos\delta}{R(R+\eta)} + \frac{q\xi^2(2R+\eta)\cos\delta}{R^3(R+\eta)^2}$$

(E.7)

$$C_{13}(\xi,\eta) = \frac{\sin\delta}{R} - \frac{q\cos\delta}{R(R+\eta)}$$

(E.8)

$$S_{22}(\xi,\eta) = \left(\frac{1}{R} - \frac{\overline{y}^2}{R^3}\right)\tan\delta - 2\frac{\partial I_0}{\partial x_2}\sin\delta\sec^2\delta - q\frac{\partial^2 I_0}{\partial x_2^2}\sec^2\delta + 2\xi\frac{\partial^2 I_1}{\partial x_2^2}\tan^2\delta$$

(E.9)

$$D_{22}(\xi,\eta) = -\frac{2\overline{y}\sin\delta + q}{R(R+\xi)} + \frac{\overline{y}^2 q(2R+\xi)}{R^3(R+\xi)^2} - \xi\frac{\partial^2 I_0}{\partial x_2^2}\tan\delta - 4\frac{\partial I_1}{\partial x_2}\sin\delta\tan\delta - 2q\frac{\partial^2 I_1}{\partial x_2^2}\tan\delta$$

(E.10)

$$T_{22}(\xi,\eta) = \xi\frac{\partial^2 I_0}{\partial x_2^2}\tan^2\delta + 2\left(2\frac{\partial I_1}{\partial x_2}\sin\delta + q\frac{\partial^2 I_1}{\partial x_2^2}\right)\tan^2\delta + 2\left(2\frac{\partial I_2}{\partial x_2}\sin\delta + q\frac{\partial^2 I_2}{\partial x_2^2}\right) + C_{22}(\xi,\eta)$$

(E.11)

$$C_{22}(\xi,\eta) = \frac{2\overline{d}\sin\delta - \eta}{R(R+\xi)} + \frac{\xi\sin^2\delta}{R(R+\eta)}$$

(E.12)

$$S_{23}(\xi,\eta) = \frac{\sin^2 \delta}{R} - \frac{2q \sin \delta \cos \delta}{R(R+\eta)} - \frac{\bar{y} q \sin \delta}{R^3} + \frac{\bar{y} q^2 (2R+\eta) \cos \delta + R^2 q^2 \cos^2 \delta}{R^3 (R+\eta)^2} \tag{E.13}$$

$$D_{23}(\xi,\eta) = \frac{2\bar{d} \sin \delta}{R(R+\xi)} + \frac{\xi \sin^2 \delta}{R(R+\eta)} - \frac{q \bar{d} \bar{y} (2R+\xi)}{R^3 (R+\xi)^2} \tag{E.14}$$

$$T_{23}(\xi,\eta) = -\frac{2q}{R(R+\xi)} + \frac{q \bar{y}^2 (2R+\xi)}{R^3 (R+\xi)^2} + \frac{\xi q \bar{y} (2R+\eta) \cos \delta + \xi q R^2 \cos^2 \delta}{R^3 (R+\eta)^2} \tag{E.15}$$

$$C_{23}(\xi,\eta) = \frac{\bar{y} \sin \delta + \bar{d} \cos \delta}{R(R+\xi)} + \frac{\xi \sin \delta \cos \delta}{R(R+\eta)} \tag{E.16}$$

$$S_{33}(\xi,\eta) = \frac{\sin \delta \cos \delta}{R} + \frac{q(\sin^2 \delta - \cos^2 \delta)}{R(R+\eta)} + \frac{\bar{d} q \sin \delta}{R^3} - \frac{\bar{d} q^2 (2R+\eta) \cos \delta + R^2 q^2 \sin \delta \cos \delta}{R^3 (R+\eta)^2} \tag{E.17}$$

$$D_{33}(\xi,\eta) = \frac{\bar{y} \sin \delta + \bar{d} \cos \delta}{R(R+\xi)} + \frac{\xi \sin \delta \cos \delta}{R(R+\eta)} + \frac{q \bar{d}^2 (2R+\xi)}{R^3 (R+\xi)^2} \tag{E.18}$$

$$T_{33}(\xi,\eta) = \frac{\eta}{R(R+\xi)} + \frac{\xi}{R(R+\eta)} - \frac{q \bar{d} \bar{y} (2R+\xi)}{R^3 (R+\xi)^2} - \frac{\xi q [\bar{d}(2R+\eta) + R^2 \sin \delta] \cos \delta}{R^3 (R+\eta)^2} \tag{E.19}$$

$$C_{33}(\xi,\eta) = -\frac{2\bar{d} \sin \delta - \eta}{R(R+\xi)} + \frac{\xi \cos^2 \delta}{R(R+\eta)} \tag{E.20}$$

$$\frac{\partial I_0}{\partial x_1} = \frac{\xi}{R} \left(\frac{1}{R+\eta} - \frac{\sin \delta}{R+\bar{d}} \right) \tag{E.21}$$

$$\frac{\partial I_0}{\partial x_2} = \frac{\bar{y} + R \cos \delta}{R(R+\eta)} - \frac{\bar{y} \sin \delta}{R(R+\bar{d})} \tag{E.22}$$

$$\frac{\partial^2 I_0}{\partial x_1 \partial x_2} = -\frac{\xi (R \cos \delta - q)(2R+\bar{d})}{R^3 (R+\bar{d})^2} + \frac{\xi \cos \delta}{R^2 (R+\bar{d})} - \frac{q \xi (2R+\eta) \sin \delta}{R^3 (R+\eta)^2} \tag{E.23}$$

$$\frac{\partial^2 I_0}{\partial x_2^2} = \frac{q \bar{y} (2R+\bar{d}) - R^2 (R \sin \delta + \eta)}{R^3 (R+\bar{d})^2} - \frac{q \bar{y} (2R+\eta) \sin \delta - R^2 (R \sin \delta + \bar{d}) \sin \delta}{R^3 (R+\eta)^2} \tag{E.24}$$

$$\frac{\partial I_1}{\partial x_1} = -\frac{\eta \cos \delta}{2R(R+\bar{d})} - \frac{q^2 \cos \delta}{2R(R+\eta)(R+\bar{d})} + \frac{q(1 - \sin \delta)}{2(R+\eta)(R+\bar{d})} \tag{E.25}$$

$$\frac{\partial I_1}{\partial x_2} = \frac{\xi}{2R(R+\bar{d})} - \frac{\xi \sin \delta}{2R(R+\eta)} \tag{E.26}$$

$$\frac{\partial^2 I_1}{\partial x_1 \partial x_2} = \frac{1}{2R(R+\bar{d})} - \frac{\xi^2 (2R+\bar{d})}{2R^3 (R+\bar{d})^2} - \frac{\sin \delta}{2R(R+\eta)} + \frac{\xi^2 (2R+\eta) \sin \delta}{2R^3 (R+\eta)^2} \tag{E.27}$$

$$\frac{\partial^2 I_1}{\partial x_2^2} = \frac{\xi\left(\overline{y}\left(2R+\eta\right)+R^2\cos\delta\right)\sin\delta}{2R^3\left(R+\eta\right)^2} - \frac{\xi\overline{y}\left(2R+\overline{d}\right)}{2R^3\left(R+\overline{d}\right)^2} \tag{E.28}$$

$$\frac{\partial I_2}{\partial x_1} = \frac{q}{2R\left(R+\eta\right)} \tag{E.29}$$

$$\frac{\partial I_2}{\partial x_2} = -\frac{\overline{d}}{2R\left(R+\xi\right)} - \frac{\xi\sin\delta}{2R\left(R+\eta\right)} \tag{E.30}$$

$$\frac{\partial^2 I_2}{\partial x_1 \partial x_2} = \frac{\overline{d}}{2R^3} - \frac{\sin\delta}{2R\left(R+\eta\right)} + \frac{\xi^2\left(2R+\eta\right)\sin\delta}{2R^3\left(R+\eta\right)^2} \tag{E.31}$$

$$\frac{\partial^2 I_2}{\partial x_2^2} = \frac{\overline{d}\,\overline{y}\left(2R+\xi\right)}{2R^3\left(R+\xi\right)^2} + \frac{\xi\sin\delta\left(\overline{y}\left(2R+\eta\right)+R^2\cos\delta\right)}{2R^3\left(R+\eta\right)^2} \tag{E.32}$$

If $\cos\delta = 0$

$$S_{12}\left(\xi,\eta\right) = \frac{\xi\sin^2\delta}{2R\left(R+\overline{d}\right)} - \frac{\left(\eta\sin\delta+q\cos\delta\right)\xi\sin^2\delta}{2R\left(R+\overline{d}\right)^2} - \frac{\xi\left(R\sin\delta+q\cos\delta\right)\sin^2\delta}{R^2\left(R+\eta\right)}$$

$$+ \frac{\xi q\left(\overline{y}+R\cos\delta\right)\left(2R+\eta\right)\sin^2\delta}{R^3\left(R+\eta\right)^2} - \frac{\xi q\overline{y}\left(2R+\overline{d}\right)\sin\delta}{2R^3\left(R+\overline{d}\right)^2} + \frac{\xi q\eta\overline{y}\left(3R+\overline{d}\right)\sin^2\delta}{2R^3\left(R+\overline{d}\right)^3} \tag{E.33}$$

$$D_{12}\left(\xi,\eta\right) = -\frac{\sin\delta}{R} + \frac{q\overline{y}}{R^3} \tag{E.34}$$

$$T_{12}\left(\xi,\eta\right) = 2\frac{\partial I_2}{\partial x_1}\sin\delta + 2q\frac{\partial^2 I_2}{\partial x_1 \partial x_2} + \frac{R\cos\delta+\overline{y}\sin\delta}{2R\left(R+\overline{d}\right)} - \left(\frac{\xi^2\cos\delta+\eta\overline{y}}{2R\left(R+\overline{d}\right)^2}\right)$$

$$- \frac{\xi^2\overline{y}\left(2R+\overline{d}\right)\sin\delta}{2R^3\left(R+\overline{d}\right)^2} + \frac{\xi^2\eta\overline{y}\left(3R+\overline{d}\right)}{2R^3\left(R+\overline{d}\right)^3} \tag{E.35}$$

$$S_{22}\left(\xi,\eta\right) = -\frac{\left(2\overline{y}\sin\delta+q\right)\sin^2\delta}{R\left(R+\eta\right)} + \frac{\overline{y}\sin^2\delta}{2R\left(R+\overline{d}\right)} - \frac{\left(R\eta\sin^2\delta+q\overline{y}\right)\overline{y}\sin\delta}{2R^2\left(R+\overline{d}\right)^2}$$

$$- \frac{\left(\eta\sin\delta-R-\overline{d}\right)\sin\delta}{2R\left(R+\overline{d}\right)^2}\left(\overline{y}\sin\delta+q-\frac{q\overline{y}^2\left(3R+\overline{d}\right)}{R^2\left(R+\overline{d}\right)}\right) + \frac{q\overline{y}^2\left(2R+\eta\right)\sin^2\delta}{R^3\left(R+\eta\right)^2} \tag{E.36}$$

$$D_{22}\left(\xi,\eta\right) = -\frac{2\overline{y}\sin\delta+q}{R\left(R+\xi\right)} + \frac{q\overline{y}^2\left(2R+\xi\right)}{R^3\left(R+\xi\right)^2} \tag{E.37}$$

$$T_{22}(\xi,\eta) = \frac{\partial^2 C}{\partial x^2} + 2\frac{\partial I_2}{\partial x_2}\sin\delta + 2(q+\sin\delta)\frac{\partial^2 I_2}{\partial x_2^2} + \frac{\xi R\sin\delta}{2R^2(R+\overline{d})} - \frac{\xi\eta}{2R(R+\overline{d})^2}$$

$$-\frac{\xi\overline{y}^2(2R+\overline{d})\sin\delta}{2R^3(R+\overline{d})^2} + \frac{\xi\eta\overline{y}^2(3R+\overline{d})}{2R^3(R+\overline{d})^3} \tag{E.38}$$

Appendix F: Markov Chain Model

A Markov chain is a random process having the property of 'memoryless': future state only depends on the present state, and past states have no influence on the future. This property is called the Markov property, and can be formally expressed by:

$$P(X_{n+1} = x \mid X_n = x_n, X_{n-1} = x_{n-1}, \cdots, X_2 = x_2, X_1 = x_1) = P(X_{n+1} = x \mid X_n = x_n) \qquad \text{(F.1)}$$

where X_1, X_2, X_3 … are random variable; x_1, x_2, x_3 … are their realizations, i.e., the state of the system. All the possible states form a countable set E, which is called the state space of the Markov chain. $P(A \mid B)$ denotes the conditional probability of A given B. Followings are some general definition and properties about Markov chain.

Transition probability

In a system, the probability for going from state i to state j in n time steps can be expressed as:

$$p_{ij}^{(n)} = P(X(n) = j \mid X(0) = i) \qquad \text{(F.2)}$$

which is call n-step transition probability. Specifically, the 1-step transition probability can be simply written as p_{ij}.

If the transition probability does not depend on time, the Markov chain is time-homogeneous, i.e.,

$$p_{ij}^{(n)} = P(X(n+k) = j \mid X(k) = i) \text{ for all k.} \qquad \text{(F.3)}$$

Reducibility

If the probability of transitioning from state i to state j is non-zero, i.e.,

$$p_{ij}^{(n)} = P(X(n) = j \mid X(0) = i) > 0, \text{ for } n \geq 0 \qquad \text{(F.4)}$$

then, state j is said to be accessible from state i.

Two states are said to communicate with each other if both states are accessible from each other. Assuming a set of states C, if every pair of states in C communicates with each other, we call C is a communicating class. If the state space of a Markov chain is a single communicating class, i.e., any state is accessible from any state in space, the Markov chain is irreducible.

Periodicity

The state X_i has period $t > 1$ if $p_{ii}^{(n)} = 0$ unless $n = vt$ is a multiple of t. The state X_i is aperiodic if no such $t > 1$ exists. In other words, returning to state X_i can occur at irregular times.

Transition probability matrix.

Let $\{X(t), t = 0,1,2,\cdots\}$ be a Markov chain, and the state space $E = \{0,1,\cdots,S\}$. We can use a matrix to describe all transition probabilities:

$$A = \begin{pmatrix} p_{00} & p_{01} & \cdots & p_{0S} \\ p_{10} & p_{11} & \cdots & p_{1S} \\ \vdots & \vdots & \vdots & \vdots \\ p_{S0} & p_{S1} & \cdots & p_{SS} \end{pmatrix} \tag{F.5}$$

The matrix A is called transition probability matrix.

Stationary distribution

The time-dependent probability function of variable X in the Markov chain can be represented by a vector

$$\bar{\rho}^{(t)} = (\rho_0^{(t)}, \rho_1^{(t)}, \cdots, \rho_S^{(t)}) \tag{F.6}$$

where $\bar{\rho}_i^{(t)} = P(X(t) = i), i \in E$. The vector $\bar{\rho}^{(t)}$ is called the distribution of X at time t, i.e. $X(t)$.

The vector $\bar{\rho}^{(t)}$ describes the evolution of a Markov chain over time. In particular, it is interesting to check whether the limit $\lim_{t\to\infty} \bar{\rho}^{(t)}$ exists and what it looks like. For a given Markov chain $\{X(t), t = 0,1,2,\cdots\}$, if its distribution $\bar{\rho}^{(t)}$ is the same for all time t, i.e., $\rho = \rho^{(1)} = \rho^{(2)} = \cdots = \rho^{(t)} = \cdots$, this Markov chain is stationary, and $\rho = (\rho_0, \rho_1, \cdots, \rho_S)$ is called a stationary distribution for transition matrix A.

Theorem 1: Let $\rho^{(t)}$ be the distributions at successive time t, of a Markov chain $\{X(t)\}$ with transition matrix A. If $\rho = \lim_{t\to\infty} \rho^{(t)}$ exists, it is a stationary distribution for A.

Theorem 2: Assume a Markov chain is irreducible and aperiodic. Then there exists a unique stationary distribution ρ for A. For any states i and j,

$$\lim_{t\to\infty} P(X(t) = j \mid X(0) = i) = \lim_{t\to\infty} p_{ij}^{(t)} = \rho_j \tag{F.7}$$

For any initial distribution $\rho^{(0)}$, $\lim_{t\to\infty} \rho^{(t)} = \rho$